MULTI-LEPTON SEARCH FOR NEW PHYSICS IN 35 PB^{-1} PROTON-PROTON COLLISIONS AT THE LHC WITH THE CENTER MASS ENERGY OF $\sqrt{S} = 7$ TEV WITH CMS DETECTOR

BY DMITRY HITS

A dissertation submitted to the

Graduate School—New Brunswick

Rutgers, The State University of New Jersey

in partial fulfillment of the requirements

for the degree of

Doctor of Philosophy

Graduate Program in Physics and Astronomy

Written under the direction of

Professor Steve Schnetzer

and approved by

_____

_____

_____

_____

_____

New Brunswick, New Jersey

May, 2011

ABSTRACT OF THE DISSERTATION

Multi-lepton search for new physics in $35\ pb^{-1}$ proton-proton collisions at the LHC with the center mass energy of $\sqrt{s} = 7$ TeV with CMS detector

by Dmitry Hits

Dissertation Director: Professor Steve Schnetzer

This thesis describes a model independent search for new physics with decay signature of three or more leptons and missing energy in 35 pb^{-1} of proton-proton collisions at the LHC with center mass energy $\sqrt{s} = 7$ TeV with the CMS detector. The Standard Model backgrounds are predicted using both simulations and collision data. The observed events are fully consistent with the Standard Model predictions. The results are interpreted using various super-symmetry models: The gravity mediated super-symmetry breaking model, the gauge mediated super-symmetry breaking with slepton co-NLSP model, and leptonic R-parity violating super-symmetry model.

Acknowledgements

I would like to acknowledge

Dedication

For

Table of Contents

List of Tables

List of Figures

List of Abbreviations

CMS Compact Muon Solenoid -one of the general purpose detectors at the LHC

LHC Large Hadron Collider - an accelerator complex, on outskirts of Geneva, currently colliding protons on proton with center mass energy 7 TeV.

Chapter 1
Introduction

From the very first days of civilization people were trying to understand the building blocks of the universe around us. Early greek philosophers, Democritus and Leucippus, proposed that everything around us is made of indivisible pieces which they called atoms or "un-cutables". Thus starting the science which later got the name of particle physics!

Modern particle physicists strive not only to understand the properties of the elementary particles of which our universe is made of, but also strive to describe the interactions between those particles. Their efforts had resulted in what known as a Standard Model.

The Standard Model of particle physics is a fundamental theory describing the elementary particles and their interactions. I will describe the Standard Model in more details later. Here I want to mention that this theory is

The Higgs boson gives particles their masses and breaks the ElectroWeak symmetry but it has not been discovered yet.

The foundation of the Standard Model lies the a symmetry which describes the interaction of the particles. The SuperSymmetry.

Besides super-symmetry a myriad of other exotic theories exists.

The particle physics in general and particle physics at CMS is full of the technical jargon. I try to explain all the technical terms I use as early in the text as possible.

This thesis presents a search for new physics which demonstrates itself as 3 or more leptons. I will start in chapters 2 and 3 with the theoretical motivation for this search. Then in chapter 4 I will introduce the experimental setup we use to search for new physics. I will then make a small diversion and in section 4.3 tell you about the future part of this experimental setup in building which I have been actively involved. The I come back to describing the rest of the experimental setup and in sections **??** and **??** will describe the trigger system, followed by chapter 5 describing the reconstruction and identification. Finally, in the last two chapters, 6 and 7, I will describe our analysis and present results.

Chapter 2

From Standard Model to R-Parity Violating Supersymmetry

As previously mentioned in the introduction, particle physics approaches the study of our world by studying elementary particles and the interactions between them. Currently, the most successful theory describing all the known particles and their interactions is the so-called Standard Model theory or simply the Standard Model. Its current structure evolved in the 1970's from the works of Glashow, Weinberg, and Salam. It postulates that the

2.1 Standard Model

s

The Standard Model of particle physics is a gauge theory based on a local symmetry group $U(1)_Y \times SU(2)_L \times SU(3)_C$. To describe the particles and their interaction, it uses a classical mechanics invention, Lagrangian density. With the aid Lagrangian density it derives equation of motion, while requiring the Lagrangian density and the resulting equation of motion to be invariant under the transformations of the symmetry. To demonstrate this principle I will, as an example, derive the Lagrangian density for the scalar field $\phi(x)$, which is required to be invariant under local phase transformation of $U(1)$ symmetry:

$$\phi(x) \to e^{iq_\phi \alpha(x)} \phi(x) \tag{2.1}$$

It is not complicated to show that such transformation does not leave the free field Lagrangian invariant:

$$\mathcal{L} = \partial_\mu \phi^\dagger \partial^\mu \phi - m^2 \phi^\dagger \phi \ , \tag{2.2}$$

where ∂^μ is a covariant derivative $(\partial_t, -\nabla)$. Calculating the covariant derivative of the transformed field one obtains:

$$\partial_\mu \phi(x) \to e^{iq_\phi \alpha(x)} \partial_\mu \phi(x) + iq_\phi [\partial_\mu \alpha(x)] e^{iq_\phi \alpha(x)} \phi(x) \tag{2.3}$$

The problem arises in the second term of this formula (2.3), as it does not cancel when multiplied by its hermitian conjugate. To restore the invariance of the Lagrangian we are forced to introduce a vector potential A_μ which transforms as:

$$A_\mu(x) \to A_\mu - \partial_\mu \alpha(x) \tag{2.4}$$

and replace the covariant derivatives ∂_μ with the gauge covariant derivatives $D_\mu = \partial_\mu + iq_\phi A_\mu$ thus transforming the Lagrangian density into:

$$\mathcal{L} = D_\mu \phi^\dagger D^\mu \phi - m^2 \phi^\dagger \phi - \frac{1}{4} F^{\mu\nu} F_{\mu\nu} \ , \tag{2.5}$$

where $F^{\mu\nu} = \partial_\mu A_\nu - \partial_\nu A_\mu$ and q_ϕ is the charge of the field ϕ, determining both the strength of the interaction of the field and the vector potential. This new Lagrangian density is invariant under the transformation 2.1, because the second term in 2.4 cancels the second term in 2.3.

Now let us examine the new Lagrangian. Expanding the covariant derivatives in it we can identify three parts:

$$\mathcal{L} = \mathcal{L}_{free} + \mathcal{L}_{int} + \mathcal{L}_{gf} \ , \tag{2.6}$$

The first part is the Lagrangian of the free particle:

$$\mathcal{L}_{free} = \partial_\mu \phi^\dagger \partial^\mu \phi - m^2 \phi^\dagger \phi \ , \tag{2.7}$$

The second part describes the interaction of the scalar field ϕ with the vector potential A_μ:

$$\mathcal{L}_{int} = -iq\big(\phi^\dagger \partial^\mu \phi - (\partial^\mu \phi^\dagger)\phi\big) A_\mu + q^2 A^\mu A_\mu \phi^\dagger \phi \ , \tag{2.8}$$

And the third part, called gauge fixing (gf), removes the ambiguity in the choice of the gauge field by fixing the value of it at all space-time points.

$$\mathcal{L}_{gf} = -\frac{1}{4} F^{\mu\nu} F_{\mu\nu} \tag{2.9}$$

This term also defines the kinetic energy of the gauge field, which in this case is a photon. Note that the gauge field here is massless by construction, because the mass term $-\frac{1}{2} m_A^2 A_\mu A^\mu$ will not be invariant under the transformation 2.1.

This method can be generalized to non-Abelian symmetries such as $SU(2)$ and $SU(3)$ using the prescription for forming the gauge covariant derivatives

$$D_\mu = \partial_\mu + igt_A V_{A\mu}$$

where t_A is the group generator for the particular symmetry. For example the group generators for $SU(2)$ symmetries are Pauli matrices $t_A = \frac{1}{2}\sigma_A$, where $A = 1,\ 2,\ 3$,

$$\sigma_1 = \begin{pmatrix} 0 & 1 \\ 1 & 0 \end{pmatrix}, \quad \sigma_2 = \begin{pmatrix} 0 & -i \\ i & 0 \end{pmatrix}, \quad \sigma_3 = \begin{pmatrix} 1 & 0 \\ 0 & -1 \end{pmatrix} \tag{2.10}$$

The gauge field strength

$$F_{A\mu\nu} = \partial_\mu V_{A\nu} - \partial_\nu V_{A\mu} - g f_{ABC} V_{B\mu} V_{C\nu}$$

has an extra term $gf_{ABC}V_{B\mu}V_{C\nu}$ where f_{ABC} is a structure constant of the gauge group. This term describes the self-interaction of the gauge fields. The details of the construction of the Lagrangian density for the SU(2) and SU(3) gauge symmetries are cumbersome and will not be shown here. However, one may consult one of the classic texts on the subject, for example [7], if details are desired.

The above examples demonstrate that by using local gauge symmetries, one can construct a theory of interactions between particles and describe the properties of these interactions. All one has to do is find the correct symmetry! The symmetry that describes all Standard Model interactions is:

$$U(1)_Y \times SU(2)_L \times SU(3)_C \tag{2.11}$$

where $SU(3)_C$ is a non-Abelian[1] symmetry that describes the "strong" interactions between particles that carry a property called "color" ("C" in the subscript). The symmetry generator is a color triplet. The carriers of the strong interaction are the massless fields called gluons, there are eight different color combinations of gluons generated by the $SU(3)_C$ symmetry. The only other particles that carry color are quarks.

$SU(2)_L$ is another non-Abelian symmetry that describes the "weak" interaction, which acts on particles having weak isospin, t, which is a quantum number associated with an $SU(2)$ doublet. Some examples of $SU(2)$ doublets and their weak isospin number are shown below:

$$t = \frac{1}{2}, \qquad t_3 \;=\; \begin{cases} +\frac{1}{2} & \begin{pmatrix} \nu_e \\ e^- \end{pmatrix}_L, \qquad \begin{pmatrix} u \\ d_C \end{pmatrix}_L \\ -\frac{1}{2} & \end{cases} \tag{2.12}$$

[1]Non-Abelian symmetry is the symmetry which transformations do not commute.

where t_3 is the third component of the weak isospin. The subscript "L" indicates that this symmetry only acts on the "left-handed" doublets, or the doublets whose eigenvalue is -1 when acted by chirality operator γ_5[2].

$U(1)_Y$ is an Abelian symmetry, which is similar to the $U(1)$ symmetry of electro-magnetism described above, but instead of electric charge it is acting on particles carrying a quantum number called hyper-charge, Y.

As already mentioned above, all described symmetries generate gauge fields which are massless, because, similar to electro-magnetic case, the mass terms are not invariant under the transformations of these symmetries. Complications arise when the $SU(2)_L$ doublet of the scalar field obtains vacuum expectation value.

$$\begin{pmatrix} 0 \\ f/\sqrt{2} \end{pmatrix} \tag{2.13}$$

It spontaneously breaks the $U_Y(1) \times SU(2)_L$ symmetry to $U(1)_{em}$, which is electro-magnetic gauge symmetry. The breaking of the symmetry mixes the electro-weak gauge fields and as a result gives masses to the gauge fields that carry weak interaction, the $W^{\pm}$ and Z^0 bosons, yet leaves massless the electro-magnetic gauge field, γ or the photon.

In the following mini-sections I will briefly describe the properties of the Standard Model particles, which will be used in further chapters of this thesis.

2.1.1 Electro-Weak Bosons.

Photon.

Photon is the carrier of the electro-magnetic interaction. It has zero rest mass, zero charge, and infinite lifetime. In this analysis we do not search for photons,

[2] $\gamma_5 = \begin{pmatrix} 0 & 1 \\ 1 & 0 \end{pmatrix}$, where 1 is a two-dimensional identity matrix.

	t_3	Y	Q
ν_{eL}	$1/2$	-1	0
ν_{eR}	0	0	0
e_L	$-1/2$	-1	-1
e_R	0	-2	-1
u_L	$1/2$	$1/3$	$2/3$
u_R	0	$4/3$	$2/3$
d_L	$-1/2$	$1/3$	$-1/3$
d_R	0	$-2/3$	$-1/3$
ϕ^+	$1/2$	1	0
ϕ^0	$-1/2$	1	0

Table 2.1: Standard model particles and there charges.

however, if a photon converts into an electron-positron pair while interacting with material, it may interfere with our signal. I will postpone the description of photon conversion until section 4.2.

W bosons.

The charged $W^{\pm}$ bosons are the carriers of weak interactions. They have the same mass $m_W \approx 80.4\ GeV$ and the same inclusive production cross-section in proton-proton collision at 7 TeV, $\sigma \approx 92\ nb$. $W^{\pm}$ bosons are responsible for flavor-changing-charged-currents, interactions where the incoming particle has the charge and the flavor different from that of an outgoing particle. In fact, most of the decays of the Standard Model particles occur with intermediation of the W boson. Thus the decay of the W boson determines the decays of most particles.

Decay mode	fraction of all decays (%)
$e^-\bar{\nu_e}$	10.8
$\mu^-\bar{\nu_\mu}$	10.6
$\tau^-\bar{\nu_\tau}$	11.3
Total leptonic decays	32.4
Hadronic decays	67.6

Table 2.2: List of important W^- decays, the decays of W^+ are similar.

Z boson.

The neutral vector boson, Z^0, is the carrier of weak interactions. It has mass $m_Z \approx 91\ GeV$, and its inclusive production cross-section in proton-proton collisions at $7\ TeV$ is about $\sigma \approx 28\ nb$. The invariant mass of Z^0 decay products sharply peaks at m_Z owning to a narrow width of Z^0 decay, $\Gamma_{ll} \approx 84\ MeV$ and $\Gamma_{hh} \approx 1.7\ GeV$. The decays of the off-shell Z^0 boson, whose decay products have invariant mass lower than m_Z, are indistinguishable from the decays of the virtual photon, $\gamma^\star$. Thus the invariant mass distribution of these decay products peaks close to the double rest mass of the decay products. The decay processes of the Z^0 and $\gamma^\star$ into lepton-antilepton pairs are collectively called Drell-Yan processes and the decay products are called Drell-Yan pairs or Drell-Yan leptons. Below I list important Z^0 decay modes and their branching ratio for reference.

Decay mode	fraction of all decays (%)
e^-e^+	3.4
$\mu^-\mu^+$	3.4
$\tau^-\tau^+$	3.4
Total leptonic decays	10.1
Invisible decays	20.0
Hadronic decays	69.9

Table 2.3: List of important Z^0 decays.

2.1.2 Leptons

Neutrinos.

Neutral leptons, Interact weakly escape the detector leave energy imbalance in the detector.

Electron.

Electron is the lightest charged lepton, mass 0.5 MeV, stable particle leaves charge trace in the tracker and energy deposit in the electro-magnetic calorimeter.

Muon.

Charged lepton heavier than electron, mass 106 MeV, mean life time $\tau \approx 2\ \mu s$, which makes $c\tau \approx 600\ m$. Thus most of the time muon decays outside of the detector. It interacts with matter weakly and electro-magnetically, although since it is 2000 times heavier thatn electron it leaves a lot less energy in the detector and only leaves a charge trace in the tracker and in the muon system.

Tau.

Tau is the heaviest of all known leptons, with mass 1777 MeV or $\sim 1.8\ GeV$ and a very short lifetime, $\tau \approx 3 \times 10^{-13}\ s$, hence the $c\tau \approx 90\ \mu m$. This means that tau decays almost immediately after its production, before it is able to be registered by the detector. The detector registers only tau decay products. The tau decay proceeds via $W^{\pm}$, see figure 2.1. Thus its branching fraction is similar

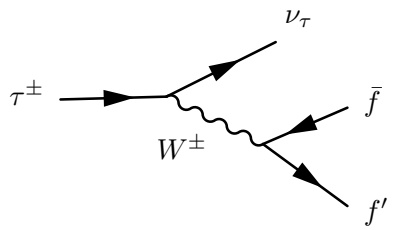

Figure 2.1: Tau decay, W here is virtual, thus $(f', \bar{f})$ can only be $(e^-, \bar{\nu}_e)$, $(\mu, \bar{\nu}_\mu)$, $(d, \bar{u})$, and their charge conjugates. The decay to $(s, \bar{u})$ occurs rarely and does not affect the branching fraction of other decays.

to that of the $W^{\pm}$. However, since the tau is lighter than the $W^{\pm}$, the $W^{\pm}$ in the tau decay is virtual. Therefore some of the decay modes are not accessible, while the branching fractions of the remaining decay modes increase.

The most important decay modes are listed in table 2.4. They are usually categorized into:

- Leptonic decay modes, which include the decay modes with a charged lepton, either electron or muon in the final state.
- Hadronic single-prong decay modes, which include the decay modes with a single charged hadron, usually π^0, in the final state.
- Hadronic three-prong decay modes, which include the decay modes with three charged hadrons in the final state.

Decay mode	fraction of all decays (%)
$e^-\bar{\nu}_e\nu_\tau$	17.9
$\mu^-\bar{\nu}_\mu\nu_\tau$	17.4
Total leptonic decays	35.1
$\pi^-\nu_\tau$	10.9
$K^-\nu_\tau$	0.7
Total hadronic single-prong isolated decays	11.6
$\pi^-\pi^0\nu_\tau$	25.5
$\pi^-2\pi^0\nu_\tau$	9.3
$\pi^-3\pi^0\nu_\tau$	1.0
Total hadronic single-prong non-isolated decays	35.8
$\pi^-\pi^+\pi^-\nu_\tau$	9.0
$\pi^-\pi^+\pi^-\pi^0\nu_\tau$	2.7
Total hadronic three-prong decays	11.7

Table 2.4: List of important tau decay modes. Only τ^- decay modes are shown. The decays of τ^+ are similar.

2.1.3 Quarks and gluons.

There are six quarks in the Standard Model, forming three generations, each generation includes an up-like quark and a down-like quark. The three lightest quarks are u, d, and s or up, down, and strange. They have masses ranging

from few MeV for 'up' and 'down' quarks to $\sim$ 100 MeV for 'strange' quark. The light quarks have a long lifetime, but due to color confinement cannot be seen individually in the detector, and instead form hadrons, which are particles consisting of two or more quarks.

b and c quarks.

The heavier b and c quarks deserve special attention because their weak decays contain charged leptons (electrons and muons) which sometimes may appear isolated, thus they can be confused with signal leptons. The lifetime of the charm hadrons is on the order of $\tau \approx 0.5 - 1\ ps$, which makes $c\tau \approx 150 - 300\ \mu m$. The lifetime of the bottom hadrons is on the order of $\tau \approx 1.5\ ps$, which makes $c\tau \approx 450\ \mu m$. Thus the decay products of these quarks appear to originate away from the interaction point. This feature can be utilized to mark the leptons coming from the decays of the heavy flavor hadrons.

Top quark.

Top quark is in a league of its own. With the mass $m \approx 172\ GeV$, it is the heaviest elementary particle known to date. Top quarks are usually produced in pairs. The cross-section of their production in proton-proton collisions at $7\ TeV$ is $\sigma \approx 164\ pb$. Top quark lifetime is very short $\tau =$, and it decays before it can hadronize, thus no top-like hadrons are known. Top quark decay through weak interaction. The main decay mode of the top quark is $t \to W^+ b$, thus it is the W decays (see table 2.2) that determine the final state of the top-quark decay, see table 2.5. Top-quark decays are the main background to many searches for new physics.

Final state	fraction of all decays (%)
$e^{\pm}\ \bar{\nu_e}\ b\ \bar{b}\ q\,\bar{q'}$	14.8
$\mu^{\pm}\,\bar{\nu_\mu}\,b\ \bar{b}\ q\,\bar{q'}$	14.8
$\tau^{\pm}\,\bar{\nu_\tau}\,b\ \bar{b}\ q\,\bar{q'}$	14.8
Total semi-leptonic decays	44.4
$e^{\pm}\ \bar{\nu_e}\ \mu^{\mp}\,\nu_\mu\,b\ \bar{b}$	2.5
$e^{\pm}\ \bar{\nu_e}\ \tau^{\mp}\,\nu_\tau\,b\ \bar{b}$	2.5
$\mu^{\pm}\,\bar{\nu_\mu}\,\tau^{\mp}\,\nu_\tau\,b\ \bar{b}$	2.5
$e^{-}\ \bar{\nu_e}\ e^{+}\,\nu_e\,b\ \bar{b}$	1.2
$\mu^{-}\,\bar{\nu_\mu}\,\mu^{+}\,\nu_\mu\,b\ \bar{b}$	1.2
$\tau^{-}\,\bar{\nu_\tau}\,\tau^{+}\,\nu_\tau\,b\ \bar{b}$	1.2
Total fully leptonic decays	11.1
$b\ \bar{b}\ q\,\bar{q'}\,q''\,\bar{q'''}$	44.4

Table 2.5: List of the final states in the top pair decay.

2.2 Super-Symmetry

The Standard Model successfully describes the majority of current experimental data. It has been tested to high precision by the Large Electron Positron (LEP) collider at CERN and by the Stanford Linear Collider (SLC) at Stanford National Laboratory, but in spite of that, it is still incomplete. Several experimental and theoretical arguments are showing gaps in the current version of the Standard Model.

Experimental argument 1: The oscillation of neutrinos, where neutrinos created by the specific lepton flavor are later determined to have a different flavor, were observed in many independent experiments. This observation suggests that neutrinos have mass, which is not explained by the Standard Model.

Experimental argument 2: Observations of fluctuations in the spectrum of the microwave background, remnant from the Big Bang, have established the existence of cold dark matter. Its existence cannot be explained by

the Standard Model. In particular, recent measurements from the Wilkinson Microwave Anisotropy Probe (WMAP) satellite show that dark matter composes 23.3% of the Universe, while ordinary baryonic matter makes up only 4.6% of it.

Experimental argument 3: Observation of large red shifts in the spectrum of the oldest Type Ia supernovas confirms the theory that 70% of the Universe is made up of dark energy. This measurement has also been supported by the WMAP satellite measurements, which established the dark matter content at 72.1%. Again the Standard Model fails to explain its existence.

Experimental argument 4: The Standard Model does not explain the existence of gravity.

Theoretical argument 1: We do not understand particle masses and their mixing parameters, therefore a large number of parameters is needed by the Standard Model.

Theoretical argument 2: The choice of both the gauge group which describes Standard Model interactions and particle representation did not originate from the theory itself.

Theoretical argument 3: The introduction of the scalar field to explain the breaking of the electroweak symmetry is done "by hand". And since the Higgs particle has not been discovered yet, this method of electroweak symmetry breaking has not been confirmed.

Several theories have been put forward to help solve the arguments listed above. Among them, the Supersymmetry holds a prominent place.

Supersymmetry is the theory that postulates the symmetry between bosons and fermions. It requires that for every Standard Model fermion there exists a

supersymmetric boson partner and for every Standard Model boson there exists a supersymmetric fermion partner.

The supersymmetry generator is an operator Q which transforms bosonic states into fermionic states and vice versa.

$$Q|\mathcal{B}\rangle = |\mathcal{F}\rangle, \qquad Q|\mathcal{F}\rangle = |\mathcal{B}\rangle \tag{2.14}$$

Note, although the spinor indices are suppressed, the supersymmetry operators are anticommuting spinors.

$$\{Q, Q^\dagger\} = P^\mu \tag{2.15}$$

where P^μ is a four-momentum generator of space-time translations.

The particles of the supersymmetry are so called "supermultiplets". They contain both fermion and boson states, which relate to each other by the supersymmetry operators, Q and $Q^\dagger$. The elements of the supermultiplet are called "superpartners" of each other. In the simplest supersymmetric theory two possibilities for the supermultiplet exists. One consists of the Weyl fermion[3] and a complex scalar (spin-0), the other consists of a spin-1 vector boson (massless before symmetry is broken) and a spin-1/2 Weyl fermion (also massless before the symmetry is broken).

Although there are many ways to construct a supersymmetric version of the Standard Model, the most popular is a minimalistic approach which tries to introduce as few extra parameters as possible. The result of such approach is Minimal Supersymmetric Standard Model or MSSM.

The construction of the MSSM begins with the selection of gauge symmetry. We choose the one utilized by the Standard Model, $U(1)_Y \times SU(2)_L \times SU(3)_C$. Then each particle of the Standard Model is promoted to a supermultiplet. The

[3]Weyl fermion is either a left-handed or right-handed part of the Dirac fermion.

superpartners in a supermultiplet, one of which is a Standard Model particle, must have spins which differ by 1/2 a unit from each other.

Thus all Standard Model fermions will obtain a scalar superpartner called scalar-fermion or sfermions, for example each quark will get superpartner scalar quark or squark, each lepton will get superpartner scalar lepton or slepton. The fermionic superpartners of the Standard Model gauge bosons are called gauginos. Also since the left-handed and right-handed parts of the Standard Model fermions transform differently under the gauge group, $SU(2)_L$, so they must have different superpartners. Thus right-handed electron will have scalar super partner right selectron, while left-handed electron will have scalar super partner left selectron. In nomenclature the superpartners of the Standard Model particles will have the same symbol with a tilde on top of it, for example right scalar muon will be $\tilde{\mu}_R$.

The superpartners of the Standard Model vector gauge bosons are fermionic states of the supermultiplet called gauginos. Particularly the superpartner of the B-boson is bino, superpartner of charged W-boson is wino, superpartner of neutral W-boson or Z (after broken electroweak symmetry) is zino.

If we include gravity, then spin-2 graviton will have spin-3/2 superpartner called gravitino.

A complication arises when creating a supermultiplet for the Standard Model Higgs iso-doublet

$$\phi = \begin{pmatrix} \phi^+ \\ \phi^0 \end{pmatrix},$$

because the hypercharge of the scalar component of the supermultiplet which is needed to give masses to "up", $t_3 = +1/2$, type fermions should to be $Y = +1$, while the hypercharge of the scalar component of the supermultiplet which is needed to give masses to "down", $t_3 = -1/2$, type fermions should be $Y = -1$. In Standard Model that was accomplished by the charge conjugate field $\phi^c = i\sigma_2\phi^*$ which has weak hypercharge $Y = -1$. However due to supersymmetric formalism

the charge conjugate Higgs field has to have its own super partner. Thus in supersymmetry not one but two supermultiplets arise the Standard Model iso-doublets

$$H_d = \begin{pmatrix} H_d^0 \\ H_d^- \end{pmatrix}$$

will have a superpartner

$$\tilde{H}_d = \begin{pmatrix} \tilde{H}_d^0 \\ \tilde{H}_d^- \end{pmatrix}$$

and the charge conjugate Standard Model iso-doublet

$$H_u = \begin{pmatrix} H_u^+ \\ H_u^0 \end{pmatrix}$$

will have a superpartner

$$\tilde{H}_u = \begin{pmatrix} \tilde{H}_u^+ \\ \tilde{H}_u^0 \end{pmatrix}.$$

The index of an iso-doublet reminds us which types of fermions, "up" or "down", are getting masses from it.

The field content of the MSSM is summarized in table 2.6.

Names		spin 0	spin 1/2	$SU(3)_C, SU(2)_L, U(1)_Y$
Squarks, quarks	Q	$\left(\tilde{u}_L \quad \tilde{d}_L\right)$	$\left(u_L \quad d_L\right)$	$(\mathbf{3},\ \mathbf{2}, +\frac{1}{6})$
$\times$ 3 families	$\bar{u}$	$\tilde{u}_R^*$	$u_R^\dagger$	$(\bar{\mathbf{3}},\ \mathbf{1}, -\frac{2}{3})$
	$\bar{d}$	$\tilde{d}_R^*$	$d_R^\dagger$	$(\bar{\mathbf{3}},\ \mathbf{1}, +\frac{1}{3})$
Sleptons, leptons	L	$\left(\tilde{\nu}_L \quad \tilde{e}_L\right)$	$\left(\nu_L \quad e_L\right)$	$(\mathbf{1},\ \mathbf{2}, +\frac{1}{2})$
$\times$ 3 families	$\bar{e}$	$\tilde{e}_R^*$	$e_R^\dagger$	$(\bar{\mathbf{1}},\ \mathbf{1}, +1)$
Higgs, higgsinos	H_u	$\left(H_u^+ \quad H_u^0\right)$	$\left(\tilde{H}_u^+ \quad \tilde{H}_u^0\right)$	$(\mathbf{1},\ \mathbf{2}, +\frac{1}{2})$
	H_d	$\left(H_d^0 \quad H_d^-\right)$	$\left(\tilde{H}_d^0 \quad \tilde{H}_d^-\right)$	$(\mathbf{1},\ \mathbf{2}, -\frac{1}{2})$

Table 2.6: Particles of the Minimal Supersymmetric Standard Model and their symmetry multiplets.

Names	spin 1/2	spin 1	$SU(3)_C, SU(2)_L, U(1)_Y$
Gluino, gluons	$\tilde{g}$	g	$(\mathbf{8},\ \mathbf{1},\ 0)$
Winos, W-bosons	$\tilde{W^{\pm}}\ \tilde{W^0}$	$W^{\pm}\ W^0$	$(\mathbf{1},\ \mathbf{3},\ 0)$
Bino, B-bosons	$\tilde{B^0}$	B^0	$(\mathbf{1},\ \mathbf{1},\ 0)$

Table 2.7: Gauge fields of the Minimal Supersymmetric Standard Model and their symmetry multiplets.

The next step in constructing MSSM is to choose a potential. It has to satisfy the following requirements: First, it has to be renormalizable, that is each term has to have total field content with total mass dimension ≤ 4. Note that the scalar field has dimension $[M]$, while the fermion field has dimension $[M^{3/2}]$. Second, the potential must be invariant under the supersymmetry transformations. it turns out that the most general term of super potential in MSSM is:

$$W_{MSSM} = \bar{u}\mathbf{y_u}QH_u - \bar{d}\mathbf{y_d}QH_d - \bar{e}\mathbf{y_e}LH_d + \mu H_u H_d + \tag{2.16}$$

$$+\lambda_{ijk}L_iL_j\bar{e}_k + \lambda'_{ijk}L_iQ_j\bar{d}_k + \mu'_iL_iH_u + \ , \tag{2.17}$$

$$+\lambda''_{ijk}\bar{u}_i\bar{u}_j\bar{d}_k \ , \tag{2.18}$$

where H_u, H_d, Q, L, $\bar{u}$, $\bar{d}$, $\bar{e}$ are super multiplets defined in table 2.6, $\mathbf{y_u}$, $\mathbf{y_d}$, $\mathbf{y_e}$ are dimensionless 3×3 matrices called Yukawa coupling parameters, the μ-term is a supersymmetric equivalent of the Higgs mass. The terms in 2.16 is the minimal viable supersymmetric potential, the terms in 2.17 violate lepton number, while the terms in 2.18 violate barion number. Both 2.17 and 2.18 cannot be present

as it would lead to decay of the proton. In most versions of supersymmetry the 2.17 and 2.18 are forbidden by imposing conservation of so-called R-parity.

$$R = (-1)^{3(B-L)+2S} \tag{2.19}$$

The particle within the supermultiplet do not have the same R-parity. The Standard Model particles have $R = +1$, while their superpartners have $R = -1$. The conservation of R-parity has an important phenomenological consequence, the lightest supersymmetric particle (LSP) would have to be stable, thus providing a viable candidate for the dark matter especially if it is neutral and weakly interacting, thus explaining why it have not been detected yet.

One of the main difficulties of the supersymmetry is deciding how it is broken. It must be broken because supersymmetry requires the states of the supermultiplet, the Standard Model state and the new supersymmetric state, to have the same mass, while none of the supersymmetric states have been detected. In MSSM the breaking of terms introduced explicitly, by writing down the "soft" breaking terms of the Lagrangian.

$$\mathcal{L}_{soft}^{MSSM} = -\frac{1}{2}(M_3\tilde{g}\tilde{g} + M_2\tilde{W}\tilde{W} + M_1\tilde{B}\tilde{B} + c.\ c.) \tag{2.20}$$

$$-(\tilde{\bar{u}}\mathbf{a_u}\tilde{Q}H_u - \tilde{\bar{d}}\mathbf{a_d}\tilde{Q}H_d - \tilde{\bar{e}}\mathbf{a_e}\tilde{Q}H_d + c.\ c.) \tag{2.21}$$

$$-\tilde{Q}^{\dagger}\mathbf{m_Q^2}\tilde{Q} - \tilde{L}^{\dagger}\mathbf{m_L^2}\tilde{L} - \tilde{\bar{u}}^{\dagger}\mathbf{m_{\bar{u}}^2}\tilde{\bar{u}} - \tilde{\bar{d}}^{\dagger}\mathbf{m_{\bar{d}}^2}\tilde{\bar{d}} - \tilde{\bar{e}}^{\dagger}\mathbf{m_{\bar{e}}^2}\tilde{\bar{e}} \tag{2.22}$$

$$-m_{H_u}^2 H_u^* H_u - m_{H_d}^2 H_d^* H_d - (bH_u H_d + c.\ c.) \tag{2.23}$$

In 2.20 the M_1, M_2, and M_3 are the bino, wino, and gluino mass terms. The scalar couplings $\mathbf{a_u}$, $\mathbf{a_d}$ and $\mathbf{a_e}$ in 2.21 are complex 3×3 matrices. They correspond to the Yukawa coupling in the superpotential 2.16 but have dimension of [mass]. Each of the $\mathbf{m_Q^2}$, $\mathbf{m_{\bar{u}}^2}$, $\mathbf{m_{\bar{d}}^2}$, $\mathbf{m_L^2}$, $\mathbf{m_{\bar{e}}^2}$ in 2.22 are 3×3 complex hermitian matrices. Finally in 2.23 we have a supersymmetry breaking potential due to the Higgs field, where $m_{H_u}^2$ and $m_{H_d}^2$ are the squared mass term of H_u and H_d and b is a squared of diagonal mass term of H_u and H_d.

In MSSM it is argued that we must expect

$$M_1,\ M_2,\ M_3,\ \mathbf{a_u}, \mathbf{a_d}, \mathbf{a_e} \sim m_{soft} \tag{2.24}$$

and

$$\mathbf{m_Q^2},\ \mathbf{m_{\bar{u}}^2},\ \mathbf{m_{\bar{d}}^2},\ \mathbf{m_L^2},\ \mathbf{m_{\bar{e}}^2},\ m_{H_u}^2,\ m_{H_d}^2, b \sim m_{soft}^2 \tag{2.25}$$

where m_{soft} can not be much larger than 1 TeV, thus making supersymmetry discoverable at the LHC!

The "soft" explicit supersymmetry breaking however is not the only variant proposed. Other types of the supersymmetry breaking are also possible. One of the popular variants of the supersymmetry breaking are the "hidden' sector models. Where the supersymmetry is broken somewhere in the "hidden" sector while the breaking is transported to our visible sector by the messenger fields.

In the following sections I will describe several supersymmetry scenarios that have multi-lepton signatures.

Chapter 3

SUSY with multi-lepton signatures

Production of superpartners at the LHC is dominated by strong processes, see figures 3.1a through 3.1c. Weak production (direct production of chargino, neu-

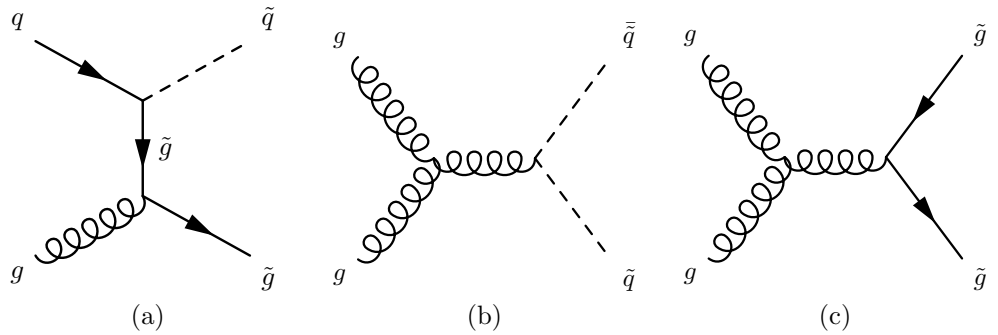

Figure 3.1: Examples of strong production diagrams of squarks and gluinos, (a) t-channel, quark-gluon to squark-gluino, (b) s-channel, gluon-gluon to squark-antisquark, (c) s-channel, gluon-gluon to gluino-gluino.

tralinos, and sleptons) at the LHC has a smaller cross-section. That is because the leading order process for the weak production is quark-antiquark annihilation. Unlike the Tevatron, where quark-antiquark pairs are abundant, in the proton-antiproton as collision particles, the LHC proton-proton collisions have much fewer quark-antiquark pairs. The only type of antiquarks in protons are the "sea" quarks, occurring through gluon splitting, which carry a small fraction of the proton's momentum. Due to the high center mass energy, the superpartners produced via strong interactions at the LHC extend the parameter space covered by the Tevatron searches.

In the following sections I will describe several SUSY scenarios, where the strong production of squarks and gluinos leads to signatures with multiple leptons in the final state.

Abbreviation	Short description
RPV	MSSM with R-parity violation
MSSM	Minimal Supersymmetric Standard Model
	Subsets of MSSM with Goldstino
MSSMG	MSSM + Goldstino
GMSB	Gauge Mediated SUSY Breaking model
MGGM	Most General Gauge Mediated SUSY breaking model
GGM	General Gauge Mediated SUSY breaking model
GMSM	Gauge Mediated SUSY breaking model with Split Messengers
MGM	Minimal Gauge Mediated SUSY breaking model
	Subsets of MSSM without Goldstino
cMSSM	constrained Minimal Supersymmetric Standard Model
mSUGRA	minimal SUper GRAvity model

Table 3.1: The hierarchy of the SUSY models from the least restrictive to the most restrictive. I only list the models which are discussed in the text or the ones that are closely related to them in some way or another.

3.1 Slepton co-NLSPs models.

An interesting SUSY model to explore at the LHC is a gauge-mediated SUSY breaking scenario with split messengers (GMSM). It has large strong-production cross-section and large branching ratios for decays with multi-leptonic final states. The GMSM is a slightly more general subset of gauge mediated SUSY breaking (GMSB) than the minimal gauge mediated SUSY breaking scenario (MGM), see table 3.1. MGM, the simplest variant of GMSB, has only 5 parameters

$$N_5 \ , \ \Lambda \ , \ M \ , \ tan(\beta) \ , \ sgn(\mu)$$

where N_5 is the equivalent number of $5 \oplus \overline{5}$ messenger fields, Λ is the SUSY breaking scale, and M is the messenger scale. However, one of the features of the MGM is that it creates a spectra where the superpartner masses are directly proportional to the associated gauge couplings squared, which makes strong super-partners much heavier than their electro-weak counterparts. Hence the strong production cross-section of such models are quite small. An example of an MGM spectrum is shown in the fugure 3.2a.

If we allow the strong and the weak messenger fields to be independent, that is to have different values of the SUSY breaking scale, then our new model, gauge-mediated SUSY breaking with split messengers (GMSM), will have strong super-partner masses independent from the electro-weak super-partner masses. The one parameter of the MGM, Λ will be replaced by two parameters, Λ_L the weak SUSY breaking scale and Λ_d the strong SUSY breaking scale. This extra complication, however, makes it possible to create a compressed spectra in which squarks and gluinos are only slightly heavier than the sleptons, the wino, and the bino. Thus creating models where the cross-sections for strongly produced super-partners are abundantly produced at the LHC. An example of a compressed spectrum is shown in figure 3.2b.

The compressed scale GMSM models naturally yield spectra where the next-to-lightest-super-partners (NLSPs), are the right-handed sleptons, that are nearly degenerate (thus they are called co-NLSPs) and a bino-like neutralino (χ_B^0) is next-to-next-to-lightest superpartner (NNLSP). For such spectra, the cascade decays from strongly produced squarks and gluinos always pass sequentially through the bino, then bino, that decays to one of the co-NLSP sleptons and a lepton, followed by the slepton decay to another lepton and the LSP Goldstino[1], see equation 3.1.

[1]Goldstino is the massless fermion which is the general feature of models with spontaneous symmetry breaking. It is analogous of the Goldstone boson that arises when the global bosonic symmetries are spontaneously broken. The goldstino is a spin $\frac{1}{2}$ fermion because the SUSY

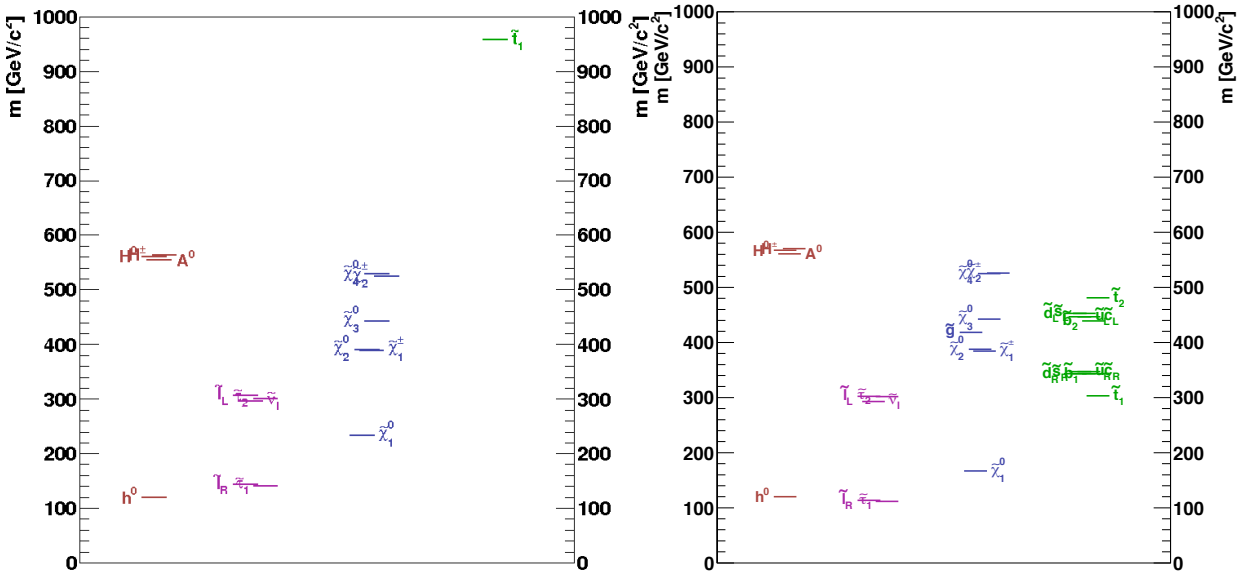

Figure 3.2: Two GMSB spectra are shown: (a) MGM spectra with $\Lambda_L = \Lambda_d = \Lambda = 35$ TeV and (b) a slightly more general GMSM spectra with parameters $\Lambda_L = 35$ TeV and $\Lambda_d = 10$ TeV. All other parameters are the same for both spectra: $N_5 = 5$, $\tan\beta = 3$, $M/\Lambda = 3$, $\mathrm{sgn}(\mu) = +$, and $\mu/m_2 = 0.95$. In the leftmost column of each figure the masses of the Higgs sector are plotted, followed by the sleptonic sector, followed by the gaugino sector, and ending with the strong sector in the rightmost column. The almost massless goldstino is not shown on neither plot. Strongly interacting superpartners that are heavier than 1 TeV/c^2 are also not shown. (Courtesy of Scott Thomas)

$$\chi_B^0 \to \widetilde{\ell}_i^{\pm}\ \ell_i^{\mp}$$
$$\hookrightarrow \ell_i^{\pm}\ \widetilde{G} \tag{3.1}$$

where i indicates lepton generation, e, μ, or τ, that are produced with roughly equal weight. The Goldstino escapes the detector carrying with it some momentum producing missing transverse energy. Thus the pair production of superpartners heavier than the bino-like neutralino will necessarily result in signatures with four prompt isolated leptons and missing transverse energy.

$$pp \to \ell_i^+ \ell_i^-\ \ell_j^+ \ell_j^- + X + \not{E}_T \tag{3.2}$$

, where X includes everything produced in the cascade decay to the bino.

An interesting scenario arises when the mass splittings between selectron and stau and between the smuon and the stau are larger than the mass of the tau. In this scenario the selectron and smuon decay predominantly to the stau, which is the lightest slepton. These decays can have either a charge preserving form

$$\chi_B^0 \to \widetilde{\ell}_i^{\pm}\ \ell_i^{\mp}$$
$$\hookrightarrow \widetilde{\tau}_1^{\pm}\ (\tau^{\mp}\ \ell_i^{\pm})$$
$$\hookrightarrow \tau^{\pm}\ \widetilde{G} \tag{3.3}$$

or a charge changing form

$$\chi_B^0 \to \widetilde{\ell}_i^{\pm}\ \ell_i^{\mp}$$
$$\hookrightarrow \widetilde{\tau}_1^{\mp}\ (\tau^{\pm}\ \ell_i^{\pm})$$

---

generator itself carries spin $\frac{1}{2}$. It is a fermionic partner of the auxiliary field that develops a SUSY breaking vacuum expectation value.

$$\hookrightarrow \tau^{\mp}\ \widetilde{G} \tag{3.4}$$

Due to the fact that the mass splittings between the heavier sleptons and the stau are quite small, the leptons and the taus emitted in the three-body decays of these heavy sleptons to stau (see middle part of the graphs 3.3 and 3.4) are very soft and are not accepted by the detector. Thus the resulting signatures of the cascading decays of squarks and gluinos in this scenario are the 2 leptons (μ or e) + 2 taus + missing energy, shown below accounting for all possible charge and flavor permutations.

$$\begin{gathered} pp \to \ell_i^{\pm}\ell_j^{\mp}\ \tau^{\pm}\tau^{\mp} + X + \not{E}_T \\ \ell_i^{\pm}\ell_j^{\pm}\ \tau^{\pm}\tau^{\mp} + X + \not{E}_T \\ \ell_i^{\pm}\ell_j^{\mp}\ \tau^{\pm}\tau^{\pm} + X + \not{E}_T \\ \ell_i^{\pm}\ell_j^{\pm}\ \tau^{\pm}\tau^{\pm} + X + \not{E}_T \end{gathered} \tag{3.5}$$

where $i, j = e, \mu$ with equal weight.

Such scenarios usually occur for moderate to high values of $tan(\beta)$, we must note that for very large $tan(\beta)$, when all sleptons except for stau become heavier than the bino, the decays of bino will proceed exclusively through stau, thus, in this case, all four leptons in the final state will be tau making it important to increase acceptance and efficiency of the reconstruction methods of tau leptons.

3.2 Leptonic R-paritiy violating SUSY.

Another super-symmetry scenario that naturally results in signatures with multiple leptons in the final state is leptonic R-parity violating SUSY. As was discussed in section 2.2 super-symmetry allows one to write a re-normalizable superpotential which does not conserve baryon and lepton numbers, see equation 3.6.

$$W_{R_p} = \frac{1}{2}\lambda_{ijk} L_i L_j \bar{E}_k + \lambda'_{ijk} L_i Q_j \bar{D}_k + \frac{1}{2}\lambda''_{ijk} \bar{U}_i \bar{D}_j \bar{D}_k \tag{3.6}$$

where i, j, and k are generation indices (note that λ_{ijk} couplings are anti-symmetric in i, j), L and Q are lepton and quark $SU(2)_L$ doublet superfields and $\bar{E}$, $\bar{D}$, and $\bar{U}$ are the charged lepton, down-like quark and up-like quark $SU(2)_R$ singlet superfields. The third term violates baryon number while the first and second terms are lepton number violating. Here we will only consider leptonic R-Parity violating (L-RPV) models with $\lambda_{ijk} \neq 0$ and $\lambda'_{ijk} = \lambda''_{ijk} = 0$.

Squarks and gluinos, produced in the *pp* collision, cascade decay down to the lightest super-partner, which we chose to be the bino-like neutralino, $\tilde{\chi}^0_B$. Because R-parity is violated, the neutralino is no longer stable. Through λ_{ijk} coupling, it decays into two charged leptons and a neutrino as shown in figures 3.3 and 3.4. We consider two separate cases, in each for simplicity we set one $\lambda_{ijk} \neq 0$ while setting all others λ_{ijk} couplings to zero: *a*) $\lambda_{122} \neq 0$, in this case at least one of the charged leptons in each neutralino decay is a muon while the other is either an electron or a muon. *b*) $\lambda_{123} \neq 0$, in this case, at least one of the charged leptons in each neutralino decay is a tau while the other is either an electron or a muon. Figure 3.3 and figure 3.4 show the Feynman diagram of the neutralino decay for the λ_{122} and λ_{123} cases, respectively.

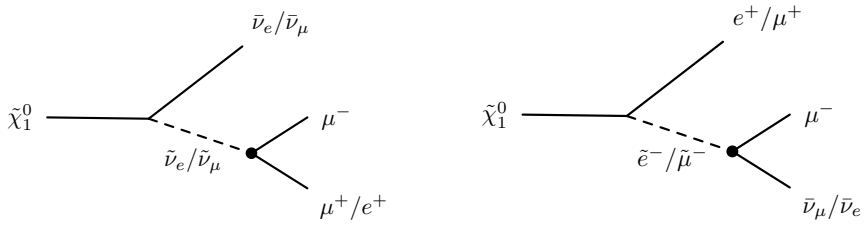

Figure 3.3: Neutralino decay for the case of $\lambda_{122} \neq 0$

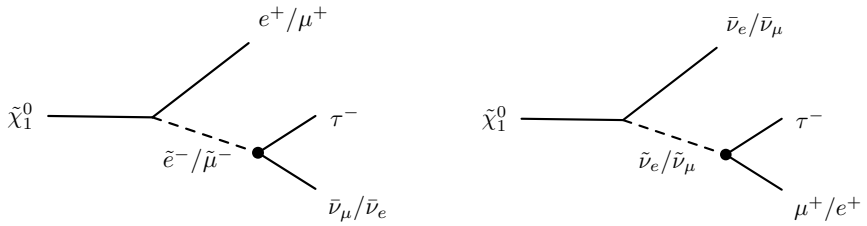

Figure 3.4: Neutralino decay for the case of $\lambda_{123} \neq 0$

Any non-zero value of λ_{ijk} will cause the neutralino to decay and will, therefore, yield multilepton final states. The actual value of λ_{ijk} simply determines the lifetime and therefore the decay length of the neutralino. As long as the value of λ_{ijk} is large enough so that decay is prompt, decay length $\lessapprox 100\mu$m, our results are independent of its value. In the limit of $m_{\tilde{\chi}_B^0} \ll m_{\tilde{l}_R} \ll m_{\tilde{l}_L}$, where $m_{\tilde{\chi}_B^0}$ is the mass of the bino-like neutralino, $m_{\tilde{l}_R}$ is the right-handed slepton mass, and $m_{\tilde{l}_L}$ is the left-handed slepton mass, a lower limit on the neutralino decay width is given by

$$\Gamma(\tilde{\chi}_B^0 \to l_i \nu_j l_k,\, \nu_i l_j l_k) \;=\; \left(\frac{\alpha \lambda_{ijk}^2}{192\pi^2 \cos^2\theta_W}\right)\left(\frac{m_{\tilde{\chi}_B^0}^5}{m_{\tilde{l}_R}^4}\right)$$

corresponding to a decay length of

$$c\tau \;\approx \left(\frac{3.7\times 10^{-11}\text{ cm}}{\lambda_{ijk}^2}\right)\left(\frac{m_{\tilde{l}_R}/100\text{ GeV})^4}{m_{\tilde{\chi}_B^0}/100\text{ GeV})^5}\right)$$

For $m_{\tilde{\chi}_B^0} = 300\ GeV/c^2$ and $m_{\tilde{l}_R} = 1000\ GeV/s^2$ the decay length is:

$$c\tau \approx \frac{1.5 \times 10^{-9}\ \text{cm}}{\lambda_{ijk}^2} \quad \Rightarrow \quad c\tau < 100\ \mu\text{m} \quad \text{for} \quad \lambda_{\text{ijk}} > 4 \times 10^{-4}$$

where θ_W is a Weinberg item and α is the fine structure constant,

An upper limit on λ_{ijk} is set by constraints from neutrino mass values. As was discussed in section 2.2 the one-loop contributions induced by λ_{ijk} to neutrino-neutralino mixing gives masses to neutrinos. However, if the value of the coupling is too big the neutrino masses would exceed the upper experimental bounds on them.

Here we choose a value for $\lambda_{122} = \lambda_{123} = 0.05$, which is both large enough to decay within a few microns from the interaction point, yet small enough to satisfy the neutrino mass constraint.

3.3 Constrained MSSM.

The constrained Minimal Supersymmetric Standard Model (cMSSM) is one of the standard benchmarks on which experiments and analyses compare their reach for new physics. It is, in fact, a slightly less constrained version of the minimal supergravity model (mSUGRA). Both, cMSSM and mSUGRA, are part of the Grand Unifying Theories, which assume that at some energy, $Q = M_U \approx 2 \times 10^{16}$, called the grand unification scale, the standard model symmetries, $SU(3)_c \times SU(2)_L \times SU(1)_Y$, are unified into one greater gauge symmetry, G, see for example [8] in which $G \equiv SU(5)$. Thus the three gauge interactions, electromagnetic, weak, and strong, unify into one single interaction, thus unifying the gauge couplings and the gaugino masses:

$$\alpha_1(M_U) = \alpha_2(M_U) = \alpha_3(M_U) \equiv \alpha_G\ , \tag{3.7}$$

where $\alpha_1(M_U)$, $\alpha_2(M_U)$, and $\alpha_3(M_U)$ are the coupling constants for electromagnetic, weak, and strong interactions, note that $\alpha_1(M_U) = \frac{5}{3}\alpha(M_U)$, where $\alpha(M_U)$ is the fine structure constant.

$$M_1(M_U) = M_2(M_U) = M_3(M_U) \equiv m_{1/2} \ , \tag{3.8}$$

where $M_1(M_U)$, $M_2(M_U)$, and $M_3(M_U)$ are the masses of bino, wino, and gluino.

The GUT models postulate the existence of a "hidden sector", which is a collection of yet unobserved particles and fields that do not interact with standard model particles via exchange of gauge bosons. However, they can interact via exchange of so called "messenger" fields, which, for example, is gravity in both the cMSSM and mSUGRA cases. These messenger fields are responsible for SUSY breaking. Since gravity is assumed to be blind to flavor, all of the parameters in the SUSY breaking potential (see 2.20 through 2.23), the masses of the scalar superpartners, the trilinear Yukawa couplings, and the square diagonal Higgs mass terms, are unified:

$$\mathbf{m_Q^2}(M_U) = \mathbf{m_U^2}(M_U) = \mathbf{m_D^2}(M_U) = \mathbf{m_L^2}(M_U) = \mathbf{m_E^2}(M_U) \equiv m_0^2\mathbf{1} \tag{3.9}$$

$$m_{H_u}^2(M_U) = m_{H_d}^2(M_U) \equiv m_0^2 \ , \tag{3.10}$$

$$\mathbf{a_u}(M_U) = A_0\mathbf{y_u},\ \mathbf{a_d}(M_U) = A_0\mathbf{y_d},\ \mathbf{a_e}(M_U) = A_0\mathbf{y_e} \ , \tag{3.11}$$

$$b = B_0\mu \tag{3.12}$$

Thus out of 105 parameters of the MSSM only 5 remain in cMSSM at the grand unified scale:

$$m_0,\ M_{1/2},\ \tan(\beta),\ A_0,\ sign\ \mu\ , \tag{3.13}$$

where, as mentioned above, m_0 is the mass of all scalar fermions at the GUT scale, s $M_{1/2}$ is the mass of all gauginos at the GUT scale, and the A_0 is the trilinear Yukawa coupling coefficient at the GUT scale (cf. 2.20 through 2.23). The parameter $\tan(\beta)$ is the ratio of vacuum expectation values for H_u and H_d. In the cMSSM B_0 can be expressed in terms of $\tan(\beta)$. The cMSSM also constrains the value of μ leaving its sign undetermined. In mSUGRA $\tan(\beta)$ is no longer a free parameter, but can be expressed through m_0 and A_0 [9]. The simplicity of these models allows for manageable phenomenological studies.

The parameters at the electroweak scale, $Q = M_Z \sim 100\ GeV$, are derived through the renormalization group equations [10, 11]. From which the following useful relations between the grand unified scale parameters and observable scale parameters can be obtained:

$$m^2_{\tilde{q}}(M_Z) \approx m_0^2 + (5-6)m^2_{1/2}\ , \tag{3.14}$$

$$m^2_{\tilde{e}_L}(M_Z) \approx m_0^2 + 0.5m^2_{1/2}\ , \tag{3.15}$$

$$m^2_{\tilde{e}_R}(M_Z) \approx m_0^2 + 0.15m^2_{1/2}\ , \tag{3.16}$$

The gaugino masses are proportional $m_{1/2}$, the $M_3(M_Z)$ mass in our sector is larger than $m_{1/2}$, while $M_1(M_Z)$ and $M_2(M_Z)$ are smaller than $m_{1/2}$. The following relations between gaugino masses is valid in cMSSM over the whole range

of the energy scales, from observable electroweak energy scale to grand unified energy scale:

$$\frac{\alpha_1(Q)}{M_1(Q)} = \frac{\alpha_2(Q)}{M_2(Q)} = \frac{\alpha_3(Q)}{M_3(Q)} \ , \tag{3.17}$$

giving the ratios of the gauginos masses: $M_1(M_Z) : M_2(M_Z) : M_3(M_Z) \sim 1 : 2 :\sim 7$, in correspondence with the ratios of electromagnetic ($\alpha_1(M_Z) = 0.017$), weak ($\alpha_2(M_Z) = 0.034$), and strong ($\alpha_3(M_Z) = 0.118 \pm 0.003$) coupling constants at the electroweak energy scale [12].

As mentioned in the introduction to this chapter the main process for production of SUSY at LHC is by strong interactions, figures 3.1a - 3.1c. Thus the multi-lepton signatures occur in cMSSM in several possible scenarios of cascade decays of strongly produced squarks and gluinos: In one scenario the squarks and gluinos cascade decay down to two neutralinos $\tilde{\chi}_2^0$, then each neutralino decays into two charged leptons and the lightest neutralino, which is stable and escapes the detector resulting in missing energy.

$$\tilde{q} \to \tilde{\chi}_2^0 + X \to l\bar{l}\tilde{\chi}_1^0 + X \tag{3.18}$$

or

$$\tilde{g} \to \tilde{\chi}_2^0 + X \to l\bar{l}\tilde{\chi}_1^0 + X \tag{3.19}$$

creating the signature of four isolated leptons and missing transverse energy. In another scenario one leg cascade decays to the neutralino ($\tilde{\chi}_2^0$) while the other leg cascade decays to the chargino ($\tilde{\chi}_1^{\pm}$), followed by decay of the neutralino to two charged leptons an the lightest neutralino and following by the chargino to a charged lepton, a neutrino, and the lightest neutralino.

$$\tilde{q} \to \tilde{\chi}_1^{\pm} + X \to l^{\pm}\nu\tilde{\chi}_1^0 + X \tag{3.20}$$

or

$$\tilde{g} \rightarrow \tilde{\chi}_1^{\pm} + X \rightarrow l^{\pm}\nu\tilde{\chi}_1^0 + X \tag{3.21}$$

thus creating a signature of three leptons and missing transverse energy. Note that in the cMSSM parameter space the lightest charginos $\tilde{\chi}_1^{\pm}$ and second lightest neutralino $\tilde{\chi}_2^0$ are approximately degenerate, see equation 3.22.

$$m_{\tilde{\chi}_2^0} \approx m_{\tilde{\chi}_1^{\pm}} \approx 2m_{\tilde{\chi}_1^0} \tag{3.22}$$

Thus the cascade decays to each of them occur in equal proportion, making the three lepton signature four times more likely than the four lepton signature.

The decays of the chargino $\tilde{\chi}_1^{\pm}$ and the neutralino $\tilde{\chi}_2^0$ down to leptons and the lightest neutralino can proceed in several ways. If sleptons are heavier than $\tilde{\chi}_1^{\pm}$, the decay of $\tilde{\chi}_1^{\pm}$ to a charged lepton, neutrino, and the lightest neutralino can either occur through a virtual slepton:

$$\begin{aligned} \tilde{\chi}_1^{\pm} &\rightarrow \widetilde{\ell}_i^{\pm}\ \nu_i \\ &\quad\ \big\lfloor\!\!\rightarrow \ell_i^{\pm}\ \tilde{\chi}_1^0 \end{aligned} \tag{3.23}$$

or through a virtual $W^{\pm}$

$$\begin{aligned} \tilde{\chi}_1^{\pm} &\rightarrow W^{\pm}\ \tilde{\chi}_1^0 \\ &\quad\ \big\lfloor\!\!\rightarrow \ell^{\pm}\nu \end{aligned} \tag{3.24}$$

The heavier the sleptons the more preferential in the decay through the process 3.24, thus reducing the branching ratio of $\tilde{\chi}_1^{\pm} \rightarrow l + \not{E}_T$ from $\sim 100\%$ to the branching ratio of $W^{\pm} \rightarrow \ell\nu$, which is $\approx 10\%$ for each lepton flavor (see section 2.1.1). In a similar way if the sleptons are heavier than $\tilde{\chi}_2^0$, the decay of $\tilde{\chi}_2^0$ into

two charged leptons and the lightest neutralino can either occur through a virtual slepton:

$$\tilde{\chi}_2^0 \rightarrow \widetilde{\ell}_i^{\pm}\ \ell_i^{\mp}$$

$$\hookrightarrow \ell_i^{\pm}\ \tilde{\chi}_1^0 \tag{3.25}$$

or through a virtual Z^0

$$\tilde{\chi}_2^0 \rightarrow Z^0\ \tilde{\chi}_1^0$$

$$\hookrightarrow \ell_i\ell_i \tag{3.26}$$

Again, the heavier the sleptons the more preferential is the decay through the process 3.26, thus reducing the branching ratio of $\tilde{\chi}_1^{\pm} \rightarrow 2l+ \not{E}_T$from $\sim 100\%$ to the branching ratio of $Z^0 \rightarrow \ell\ell$, which is $\approx 3.4\%$ for each lepton flavor (see section 2.1.1). Naturally, when the sleptons are lighter than the charginos $\tilde{\chi}_1^{\pm}$ and the neutralino $\tilde{\chi}_2^0$ then the dominant decay processes are 3.25 and 3.25 where the sleptons are real. In that region of the cMSSM parameter space the branching ratio to multi-leptons is close to 100%.

Another interesting scenario occurs when $m_{\tilde{\chi}_1^0} > m_Z$, because according to relation 3.22 the decays of $\tilde{\chi}_2^0$ through on-shell Z^0 become kinematically allowed thus SUSY signal events appear with real Z^0s accompanied by $\not{E}_T$+X.

In conclusion, I must also note that although the decay of charginos and neutralino produce the majority of multi-lepton signatures there are other processes, occurring earlier in the cascade, which also produce multi-lepton signatures. Thus the combined cross-section of all multi-lepton signatures has a complex dependance on the cMSSM parameters.

Chapter 4
LHC and CMS detector.

4.1 LHC, accelerator complex

Large Hadron Collider (LHC), colloquially known as "the machine", is the world's largest and most powerful accelerator. It has 26.7 km circumference and lies on both sides of swiss-french border on the outskirts of Geneva. It was built as a discovery machine, with the main focus on the discovering of the Higgs boson, the last building block of the Standard Model, but also with a possibility of discovering physics beyond the Standard Model, supersymmetry being one of the example. It accelerates two proton beams in opposite directions to the total energy of 3.5 TeV per proton per beam. The counter rotating proton beams are contained in separate beam pipes and only brought together in four interaction points.

The previous accelerator in the current LHC tunnel was Large Electron Positron (LEP) accelerator. It accelerated and collided electrons and positrons at the center of mass energy of 209 GeV. However, a very high losses due to synchrotron radiation made it technically impossible to accelerate electrons to even higher energies. Since the losses due to synchrotron radiation are inversely proportional to the particle mass to the fourth power, the proton was chosen for the LHC in order to achieve higher collision energies.

The full accelerator complex is shown on the figure 4.1. The path of the proton to a collision point begins from the hydrogen bottle that supplies protons to the first stage of the linear accelerator, Linac2. The Linac2 uses Radio Frequency

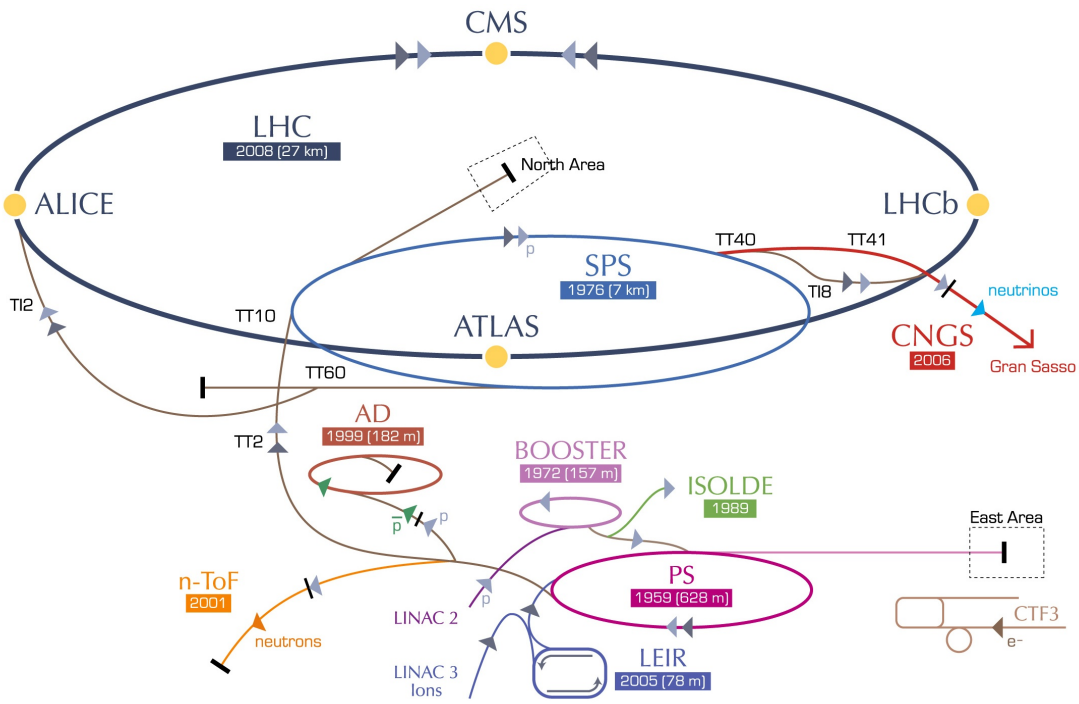

Figure 4.1: LHC accelerator complex.

Quadrupoles to accelerate the protons to 50 MeV, then, after passing the 80 m long transfer line, the protons enter 157 m circumference Proton Synchrotron Booster (PSB) ring, which further accelerates them to 1.4 GeV before injecting into the Proton Synchrotron (PS). The PS acts as a pre-injector for the LHC. It accelerates the protons to 26 GeV and splits the 6 bunches injected from the PSB into bunch trains, long equally spaced series of bunches, up to 72 bunch long with 25 ns distance between bunches. Then either the bunch trains of the individual bunches are injected into Super Proton Synchrotron (SPS), which is the final stage of acceleration before injecting into the LHC. The SPS accelerate the 26 GeV proton bunches to 450 GeV and injects them via the two separate transfer lines into the clockwise (beam 1) and anti-clockwise (beam 2) LHC rings.

Two main parameters of an accelerator that interest particle physicist are the center of mass energy of the collision also known as $\sqrt{s}$ and the integrated luminosity. The LHC is designed to accelerate the 450 GeV proton bunches injected

from SPS up to 7 TeV in two counter rotating beams, thus ultimately achieving 14 TeV center of mass collision energy. The limiting factor to the achievable energy of the beam is the magnetic field strength of the bending dipole magnets. To achieve bending of 7 TeV protons in the LHC ring the average magnetic field needed is 5.5 T. Thus approaching the limit of the maximum reachable magnetic field of 10 T for the superconducting niobium-titanium filaments, which LHC uses. During 2010 operation, due safety consideration of the LHC bending dipole magnets, the protons were accelerated up to 3.5 GeV per beam, half of the design energy, making the center of mass energy of the collision $\sqrt{s} = 7\ TeV$.

The integrated luminosity is the integral over time of the instantaneous luminosity, which is given by the following formula,

$$\mathscr{L} = \frac{n^2 k_b f \gamma}{4\pi\epsilon_n \beta^*} F \ , \tag{4.1}$$

where f is the revolution frequency, γ is the Lorentz factor, n is the number of protons per bunch, k_b is the number of colliding bunches, ϵ_n is the normalized transverse emittance, which is the amount of phase-space occupied by beam particles as they travel, β^* is the amplitude function, which modulate the transverse motion of the particles in the bunch, thus proportional to the transverse size of the beam at the interaction point, and F is the form factor which depends on the crossing angle of the collision. In 2010 the peak instantaneous luminosity achieved by the LHC was $\mathscr{L} = 2 \times 10^{32}\ cm^{-2}s^{-1}$ with the following beam parameters $\beta^* = 3.5\ m$, $\epsilon \approx 2.4\ \mu m$, 348 bunches per beam colliding in CMS and 1.2×10^{11} protons/bunch [13]. This value of instantaneous luminosity is 5 orders of magnitude higher than the maximum instantaneous luminosity in the first 7 TeV collisions at the beginning of 2010! Overall in 2010 47 pb^{-1} of integrated luminosity was delivered by the LHC to the CMS out which 43 pb^{-1} was recorded on tape and 35 pb^{-1} was approved for physics analysis.

4.2 CMS detector

Compact Muon Solenoid (CMS), shown on the figure 4.2, is one of the two multipurpose particle detectors at the LHC designed to perform searches for a broad spectrum of physics. It consist of 13 m long and 6 m in diameter superconducting solenoid, inside the solenoid, immersed in 4 T field, are the central tacker and the electromagnetic and hadronic calorimeters, outside the solenoid are the outer and forward calorimeters and, interspersed with the solenoid's return yoke steel, the muon detectors.

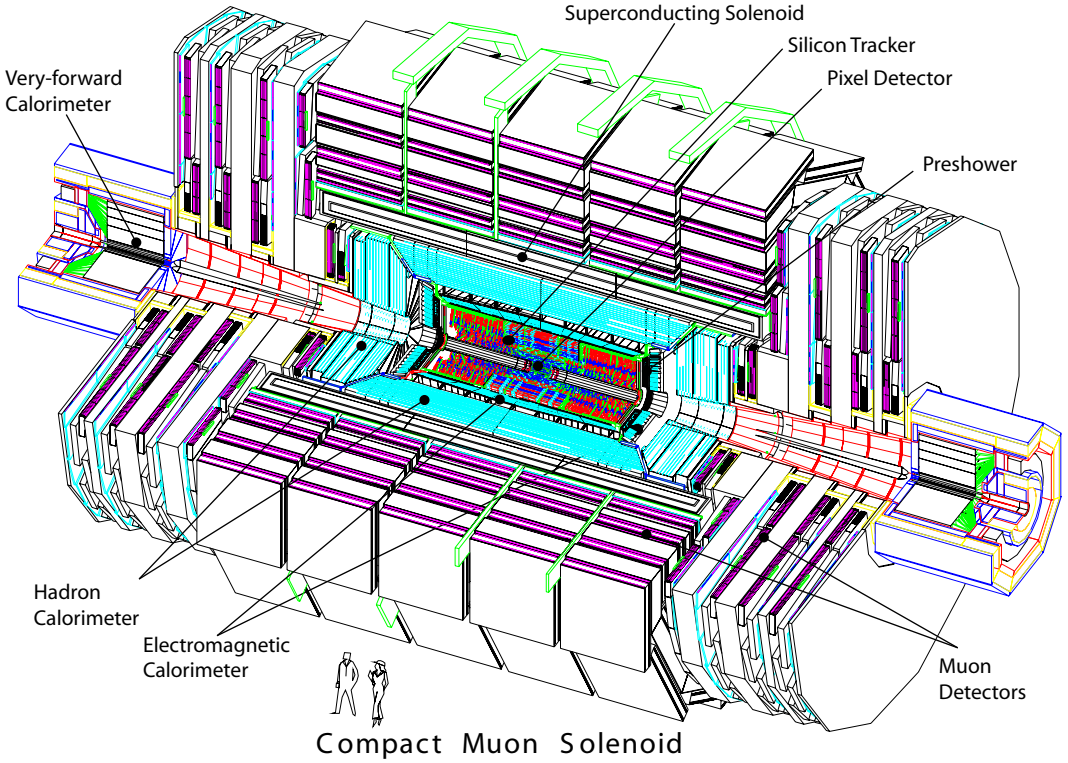

Figure 4.2: CMS detector.

The CMS coordinate system is centered at the expected collision point. The x axis is pointing toward the center of the LHC ring, the y-axis is pointing vertically upwards and the z-axis pointing horizontally in the counter-clockwise direction of the LHC ring, i.e. in the same direction as beam 2 of the LHC is traversing. Due to the cylindrical symmetry of the detector and the nature of the physics

of the hadronic collisions three more coordinates are quite useful when talking about the position of the detector components and physics objects. First, the azimuthal angle ϕ in the $x-y$ plane with $\phi = 0$ in the +x direction and $\phi = \pi/2$ in the +y direction. Second, the polar angle θ measured from the z-axis with $\theta = 0$ at +z and $\theta = \pi$ at -z. The last but not least, is a pseudo-rapidity $\eta = -\ln\tan(\theta/2)$. The η coordinate is useful for describing the scattering of the products of the collision of the hadrons, because their distribution is roughly flat in pseudo-rapidity.

Geometrically CMS detector can thought as consisting of three parts. The "barrel" – consisting of coaxial cylinders parallel to z direction and two "end-caps" – the disks perpendicular to z direction, on +z and -z ends of the detector.

The magnetic field, inside the solenoid, points in +z direction and for technical reasons can never be reversed.

In the following section I will describe the components of the detector I have used in my analysis, then take a small detour to tell about the future luminosity monitor with design and development of which I have been involved.

4.2.1 Tracker

The purpose of the tracker is to provide precise measurements of the two important quantities: the momentum of the charged particle and the 3-dimensional impact parameter of the trajectory of that particle with respect to the beam spot. The impact parameter with respect to the beam spot is the shortest distance between the trajectory and the beam spot. The measurement of the impact parameter also results in the measurement of the positions of the primary and of the secondary vertices.

The precision of the measurement of the impact parameter strongly depends on the proximity of the first trajectory measurement to the interaction point and

on the precision of the measurement of the particle's momentum, its value and its direction.

Since the trajectory of a particle in a uniform magnetic field is a helix, with the radius R and the pitch angle λ[1], where the relation between the momentum p and the radius of the trajectory is

$$p \cos\lambda \approx 0.3BR \ ,$$

where B is the value of the magnetic field measured in Tesla. Thus the precision of the measurement of the momentum depends on precision of the measurement of the curvature of the trajectory, $k \equiv \frac{1}{R}$. The curvature error δk consists of the curvature error measurement of the perfect trajectory δk_{res} and of the curvature error due to trajectory imperfections introduced by small angle multiple scatterings in the material δk_{ms}.

$$(\delta k)^2 = (\delta k_{res})^2 + (\delta k_{ms})^2$$

For the high momentum tracks the δk_{res} dominates:

$$\delta k_{res} = \frac{\epsilon}{L_T}\sqrt{\frac{720}{N+4}} \ ,$$

where ϵ is the individual sensor resolution, L_T is the transverse length of the lever-arm of the trajectory, and N is the number of the trajectory measurements. For the low momentum tracks the trajectory measurement is dominated by the multiple scattering effect:

$$\delta k_{ms} \approx \frac{(0.016)(GeV)}{pL\cos^2\lambda}\sqrt{\frac{L}{X_0}} \ ,$$

[1]pitch angle is complimentary to the polar angle θ

where p is the momentum, L is the total track length, and X_0 is the radiation length of the scattering medium, which is the length that an electron must travel to loose $1/e$ of its energy (measured in units of length here, defined elsewhere it needs to be multiplied by the density of the material).

The tracker, shown in figure 4.3, is designed to give the precise measurements of both the momentum of the charge particles and of the impact parameters of their trajectories. It is the innermost CMS sub-detector completely submerged in 4 T coaxial magnetic field. It consist of a cylindrical barrel surrounding the beam-line and flat end-cap disks.

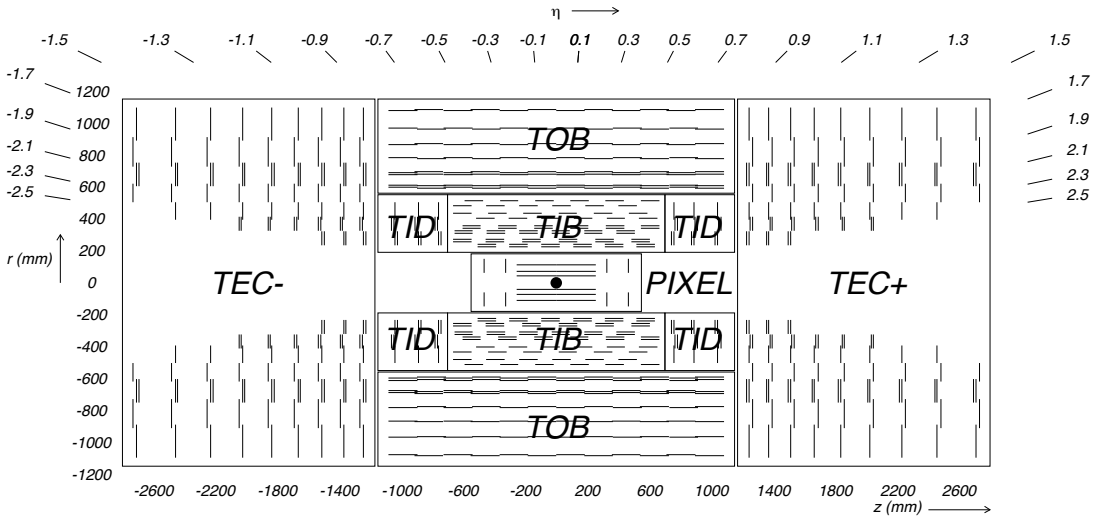

Figure 4.3: Tracker cross-section in $r - z$ plane.

The central part of the tracker is occupied by the pixel detector, shown separately in figure 4.4. It consists of three barrel layers, with radii ranging ranging from 4.4 cm to 10.2 cm, and four end-cap disks, two on each side at $z = \pm 34.5$ cm and $z = \pm 46.5$ cm. Together they cover pseudo-rapidity range up to $|\eta| = 2.5$.

Surrounding the pixel-tracker is the silicon-strip-tracker. Its total length is 5.8 m and the outermost diameter is 2.5 m. It consists of the inner and the outer-trackers. In turn, the inner and the outer-trackers consist of the barrel cylinders and the end-cap disks. The inner-tracker consist of four barrel layers

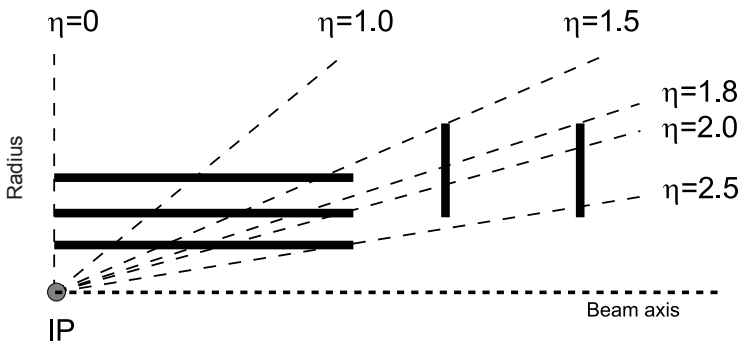

Figure 4.4: Pixel sub-detector cross-section in $r - z$ plane.

and three end-cap disks on each side. The inner-tracker is surrounded by the outer-tracker, which adds six layers in the barrel and nine layers on each side of the end-caps. Each disk of the outer-tracker end-caps consists of several rings of increasing diameter, seven in the first three disks, six in the next three, five in the next two, and four in the last one.

The measurement of the particle's trajectory is done by silicon sensors. When a charge particle traverses the sensor, it creates electrons and holes, which then drift in the direction of the electric field applied between the front and the back electrode. In addition, due to the Lorentz force induced by the magnetic field, they also drift perpendicular to the electric field, along the plane of the sensor, until collected by the front and the back electrodes, see figure 4.5. The front side of each sensor is divided into many small electrodes and due to the Lorentz drift the charge deposited by the particle is collected by several neighboring electrodes. Thus the position resolution of the hit depends on the size of the electrode and on the degree of the charge sharing between the neighboring electrodes.

In the pixel detector the front electrodes are small rectangles with a pitch of 100 μm and 150 μm in ϕ and η directions correspondently. This allows to achieve resolution of the hit position with the precision $15-20$ μm within the plane of the sensor. Due to such outstanding resolution of the hit position measurement and due to its close position to the interaction point, the pixel detector is essential

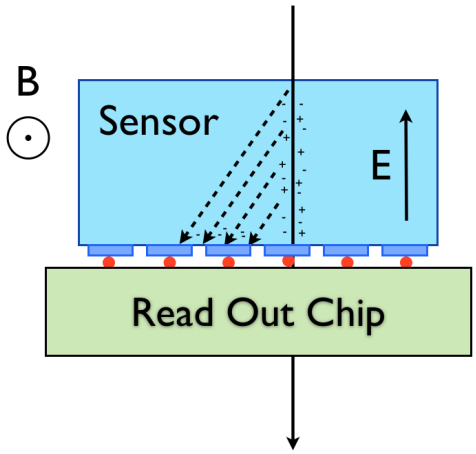

Figure 4.5: Illustration of the Lorentz drift of the charges induced by the charged particle passing through the sensor. Only the drift of the negative charges is shown. Note that the magnetic field direction with respect to the sensor is different in barrel and in the end-cap.

in determining the precise position of the secondary vertices from decays of B-hadrons and taus. It is also essential in distinguishing the primary vertices from multiple interactions that have happened in the same bunch crossing, so called "pile-up" event.

In the silicon-strip-tracker the front electrodes are long thin strips, with the pitch ranging from 80 μm to 205 μm and with their length ranging from 85 mm to 200 mm. Thus the resolution of the strip detector varies from $\sim$ 20 μm to $\sim$ 50 μm. The long side of the strips positioned along the beam-line in the barrel and along the radial direction in the end-cap disks, thus providing only the $r - \phi$ measurement of the hit position in the barrel and only the $\phi - z$ measurement of the hit position in the end-caps. Some of the layers have another sensor mounted back-to-back with the primary sensor, they are shown as a double line in figure 4.3. The additional sensor is mounted with a stereo angle of 100 $mrad$ to the original sensor, thus adding another coordinate to the measurement. For more detail about the arrangement of the tracker layers, their strip pitch and the corresponding resolutions please see [14] and the references wherein.

Thus described central tracker is able to achieve the relative precision of the transverse momentum measurement on the order of $1.5 - 2.0$ % for the high transverse momentum tracks, $p_T = 100\ GeV$. The designed precisions for the transverse and longitudinal impact parameters are on the order of 100 μm and 200 μm for the high transverse momentum tracks , $p_T = 100\ GeV$, in the central pseudo-rapidity region $|\eta| < 1$, see figures 4.6a-4.6c.

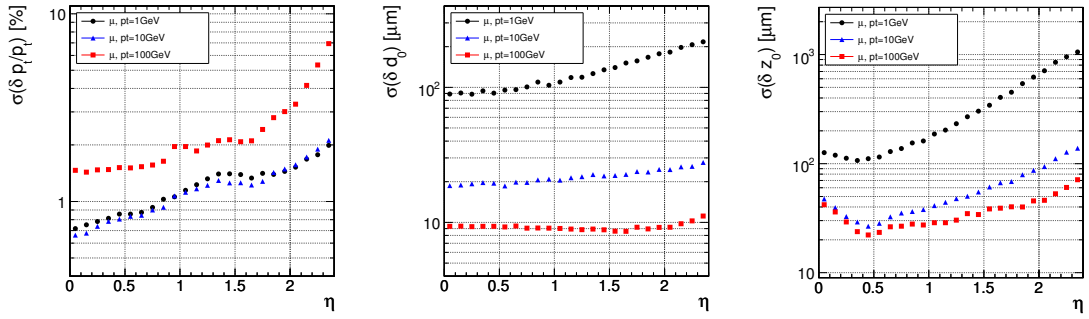

(a) (b) (c)

Figure 4.6: The tracker resolutions of the transverse momentum measurement (a), of the transverse impact parameter (b), and the longitudinal impact parameter (c) versus the pseudo-rapidity, η, for values of the momentum, 1 GeV, 10 GeV, and 100 GeV

The last but not least parameter of the tracker layers is the efficiency of the hit detection, which is for most of them is above 99%.

4.2.2 Electromagnetic calorimeter.

The primary task of the electromagnetic calorimeter is to determine the energy of the electrons and photons. It does that by converting the energy lost by an electron or photon inside the lead tungstate scintillating crystal into a blue-green scintillation light, which is subsequently detected by a light sensitive detector. The electron loses energy in the material through bremsstrahlung, whereas the photon loses it by converting to electron-positron pair. The energy loss of an electron and of a photon in the material is typically described by a radiation

length. It is the length that an electron must travel to loose $1/e$ of its energy or $7/9$ of the mean free path for electron-positron pair production by a high energy photon. This is also an appropriate length to describe the electromagnetic showers. The radiation length of a material with a single type of nuclei can be approximately calculated by formula 4.2.

$$X_0 = \frac{716.4 \cdot A}{Z(Z+1)\ln(\frac{287}{\sqrt{Z}})}\ g \cdot cm^{-2}\ , \tag{4.2}$$

where A is an mass number of the nucleus, Z is the atomic number of the nucleus. For the material with a mixture of the nuclei the radiation length can be approximated by formula 4.3.

$$\frac{1}{X_0} = \sum \frac{w_j}{X_j}\ , \tag{4.3}$$

where w_j and X_j is the fraction and the radiation length of the j^{th} element in the material.

The electromagnetic calorimeter, shown in figure 4.7, surrounds the central tracker system. It consists of a barrel covering the pseudo-rapidity range $-1.479 < \eta < 1.479$ and two end-caps each covering pseudo-rapidity ranges $-3.0 < \eta < -1.479$ and $1.479 < \eta < 3.0$, slightly extending the pseudo-rapidity coverage of the central tacker.

The active element of the electromagnetic calorimeter is a lead tungstate ($PbWO_4$) scintillating crystal. The crystals have a short radiation length, $X_0 = 0.89\ cm$, due high atomic numbers of lead and tungsten, and a small Móliere radius[2], $R_M = 2.2\ cm$. The crystals have a wedge shape with a square front face, $22 \times 22\ mm^2$, and a square back face, $26 \times 26\ mm^2$, the crystal's length is 230mm, which corresponds to 25.8 radiation lengths. The front face of the barrel

[2]Móliere radius is the radius of a cylinder containing 90% of the shower's energy deposition. It is related to the radiation length $R_M = 0.0265X_0(Z + 1.2)$

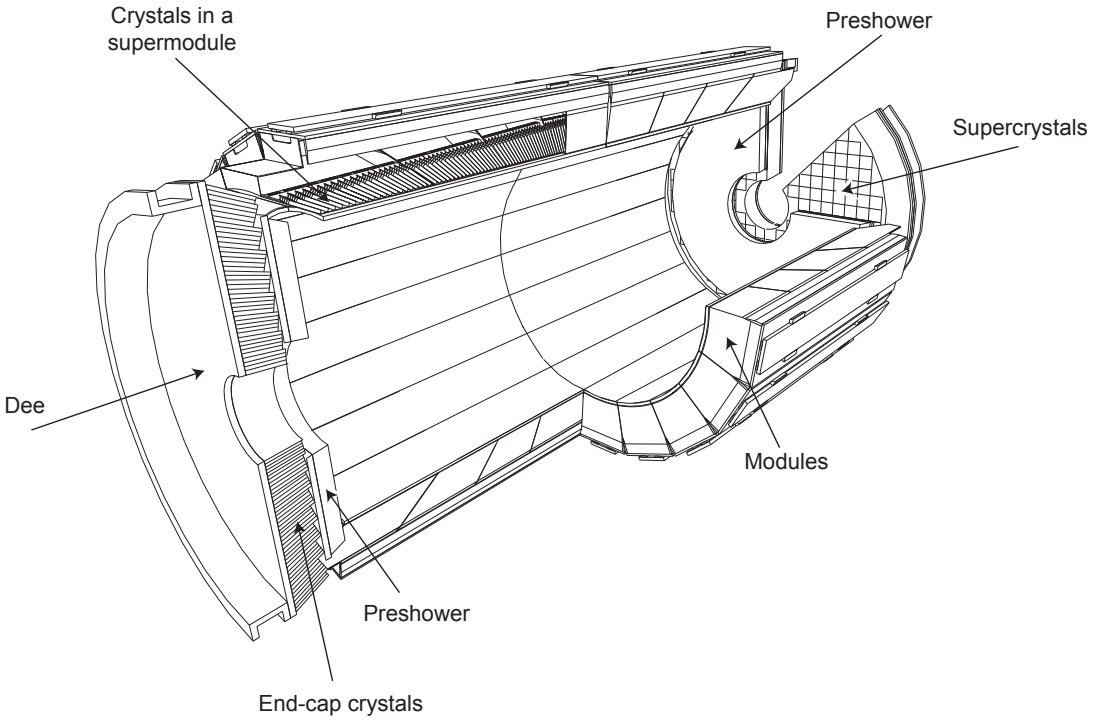

Figure 4.7: Electromagnetic calorimeter layout. Showing the arrangements of crystals, module, supermodules, end-cap Dees, and pre-shower module in front of the end-cap.

is 1.29 m radius, thus the crystal's face dimensions in terms of pseudo-rapidity and azimuthal angle are $\eta \times \phi \approx 0.0174 \times 0.0174$. The crystals are tightly positioned in the barrel and are pointed slightly away from the interaction point, thus making barrel completely hermetic.

Each end-cap consists of two half disks or "Dees" positioned at $z = \pm 315.4\, cm$. The end-cap crystals are also wedge-shaped with a square front face, $28.62 \times 28.62\ mm^2$, a square back face, $30 \times 30\ mm^2$, and a length 220 mm, thus making it 24.7 radiation lengths. To make end-caps hermetic, the crystals in it are also point slightly away from the interaction point.

In front of the each end-cap, covering the pseudo-rapidity ranges $1.653 < |\eta| < 2.6$, positioned the pre-shower detector. Its primary purpose is to identify neutral pions in the end-caps. It also helps the identification of electrons against minimum ionizing particles and improves position determination of the photons and electrons. It is able to do that due to the fine position resolution of its sensors. It uses the silicon sensors with a front electrode divided into strips with a pitch of 1.9 mm. The sensors are arrange in two layers. In front of the first sensor plane is a radiator with the thickness of two radiation lengths. After the first sensor plane but before the second plane is another radiator, one radiation length thick. Thus, the sensors measure the shower profiles of the photons.

The electromagnetic calorimeter resolution for the energies below 500 GeV, at which point the leakage through the back of the crystal becomes significant, can be parametrized as:

$$\left(\frac{\sigma}{E}\right)^2 = \left(\frac{S}{\sqrt{E}}\right)^2 + \left(\frac{N}{E}\right)^2 + C^2 \ , \tag{4.4}$$

where S is a stochastic term, N is a noise term, and C is a constant term. The typical energy resolution, determined in test beam experiments by summing energy of the block of 3×3 crystal, was,

$$\left(\frac{\sigma}{E}\right)^2 = \left(\frac{2.8\%}{\sqrt{E}}\right)^2 + \left(\frac{0.12}{E}\right)^2 + (0.3\%)^2 \ , \tag{4.5}$$

where E is measured in GeV.

During the first collisions anomalous energy deposits were discovered in the barrel of the electromagnetic calorimeter. These deposits are believed to be due to the direct ionization of the scintillation sensors, Avalanche Photo Diodes (APD), positioned at the rear faces of the scintillating crystals, by highly ionizing charged particles, such as secondary low energy protons, produced during collisions. Because these energy deposits were observed in single crystals, they were called "spikes". These anomalous energy deposits were separated from normal scintillating shower deposits by their topological and timing characteristics. The topological variable compares the energy of the single crystal, E_1, to the sum of the energy in the four adjacent crystals, E_4, is called "swiss-cross" variable. The cut on $(1 - E_4/E_1) < 0.95$ was implemented, which has rejection power that depends on the transverse energy of the signal:

- 92% for $E_T > 3\ GeV$
- 97% for $E_T > 5\ GeV$
- 99% for $E_T > 10\ GeV$

The timing variable takes advantage of the fact that the charge particles excite the shower sensor directly, thus causing it to peak earlier at $t \approx -10\ ns$. The timing variable has helped to clean out the anomalous energy deposits for the non-isolated spikes, with $(1 - E_4/E_1) < 0.95$.

4.2.3 Hadronic calorimeter.

The hadronic calorimeter, whose primary purpose is to measure and identify the strongly interacting particles, is in fact consist of several calorimeters, see figure 4.8. The central hadronic calorimeter directly surrounds the electromagnetic calorimeter. It consists of barrel, covering in pseudo-rapidity range, $|\eta| < 1.392$, and two end-caps covering pseudo-rapidity range, $1.3 < |\eta| < 3.0$. The outer radius of the central hadronic calorimeter is restricted by the inner radius of the solenoid, $R = 2.95\ m$, thus the barrel central barrel calorimeter is complimented by the hadronic outer calorimeter, "tail catcher", positioned right outside of the solenoid and covering the pseudo-rapidity range, $|\eta| < 1.3$. Finally, the forward hadronic calorimeters positioned in the forward pseudo-rapidity regions, $2.8 < |\eta| < 5.2$.

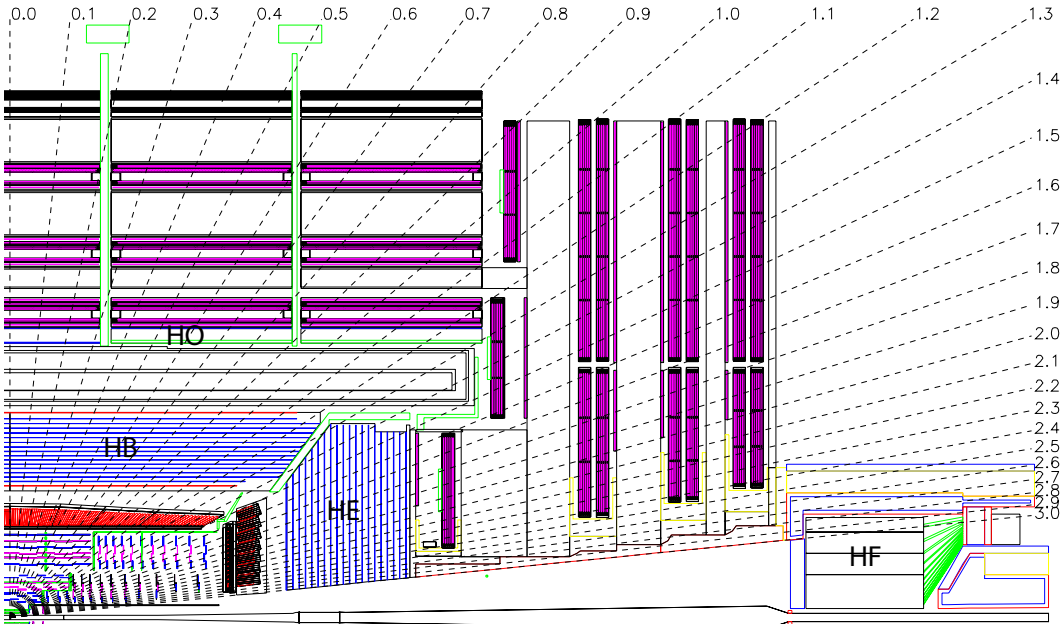

Figure 4.8: Longitudinal cross section of the quarter of the CMS detector showing the positions of the hadronic calorimeter barrel (HB), hadronic calorimeter endcap (HE), forward hadronic calorimeter (HF), and outer hadronic calorimeter (HO).

The barrel, the end-cap, and the outer hadronic calorimeters are all sampling calorimeters. They consists of plastic scintillators sandwiched between brass absorbers. Thus, the scintillators "sample" the showers of the charged particles produced by the nuclear interactions of the hadrons with the nuclei of the absorber. The absorber material is characterized by the nuclear interaction length, λ_I, which is the length over which strongly interacting particle loses $1 - 1/e$ of its energy. The absorber of the barrel calorimeter is 5.82 interaction lengths deep at 90°, the effective thickness increases with the polar angle as $1/\sin\theta$, resulting in 10.6 interaction lengths at edge of the barrel. The electromagnetic calorimeter adds another $1.1\lambda_I$ in the front. The scintillators of the hadronic calorimeter are subdivided into 72 azimuthal sectors and 36 pseudo-rapidity sectors, resulting in segmentation of $\Delta\eta \times \Delta\phi = 0.087 \times 0.087$.

The total depth of the end-cap of the hadronic calorimeter is 10 interaction lengths, which takes into account the electromagnetic calorimeter in front of it. The granularity of the end-cap calorimeter is $\Delta\eta \times \Delta\phi = 0.087 \times 0.087$ for $|\eta| < 1.6$ and $\Delta\eta \times \Delta\phi = 0.17 \times 0.17$ for $|\eta| \geq 1.6$

The outer calorimeter is positioned outside of the magnet and uses it as an additional absorber in front of another 19.5 cm thick iron. Thus making a total depth of the calorimeter system minimum $11.8\lambda_I$. It also has granularity $\Delta\eta \times \Delta\phi = 0.087 \times 0.087$, however, due to the need for the mechanical support structures and the service structures, the outer calorimeter is not as hermetic as the inner.

The forward calorimeter is also a sampling calorimeter, however, it uses radiation hard scintillating fibers, which run alone the developing electromagnetic and hadronic showers, instead of scintillating plates in the perpendicular direction as in the central hadronic calorimeter. The forward calorimeter is essentially an iron cylinder, that acts as an absorber with total depth 165 $cm \approx 10\lambda_I$. The fibers running parallel to the beam line through the holes in the iron. The fibers are

bundled to yield $\Delta\eta \times \Delta\phi = 0.175 \times 0.175$ granularity. Two lengths of fibers are used, one is running through the whole length of the calorimeter, and the other starting after 22 cm of iron. This arrangement is used to distinguish the electrons and photons, which shower in the beginning of the calorimeter, from the hadrons, which shower all the way through.

Besides measuring the energy deposits of the hadrons, electrons, and photons, forward calorimeter has another important function, the luminosity measurement. It is designed to provide luminosity information on bunch-by-bunch basis with statistical precision 1% every second. The systematic error is approximately 5%. In the future the luminosity measurement of the forward calorimeter will be supplemented by the Pixel Luminosity Monitor, which I will describe in section 4.3.

4.2.4 Muon system.

As implied by the experiment's name, Compact Muon Solenoid, muon system system is of primary importance. It has three functions: triggering muons, measurement of the muon momentum, and muon identification. Muon system has three sub-system. The barrel drift tubes (DT), the end-cap cathode strip chambers, and resistive plate chambers (RPC) covering both barrel and end-cap.

DT

The DT muon subsystem, shown on figure 4.9, covers pseudo-rapidity range, $|\eta| < 1.2$. It consist of five wheels, each wheel divided into 12 sectors, with each sector consisting of four chambers, one on inside of the magnet-return-yoke, one on the outside and two sandwiched in between the magnet-return-yoke. The supports for the magnet-return-yoke in between the chambers are placed, so they do not overlap in azimuthal angle ϕ, thus insuring complete ϕ coverage by the DT chambers. Each drift-tube chamber is made of either three or two superlayers, each superlayer, in its turn, is made of four layers of long rectangular drift cells

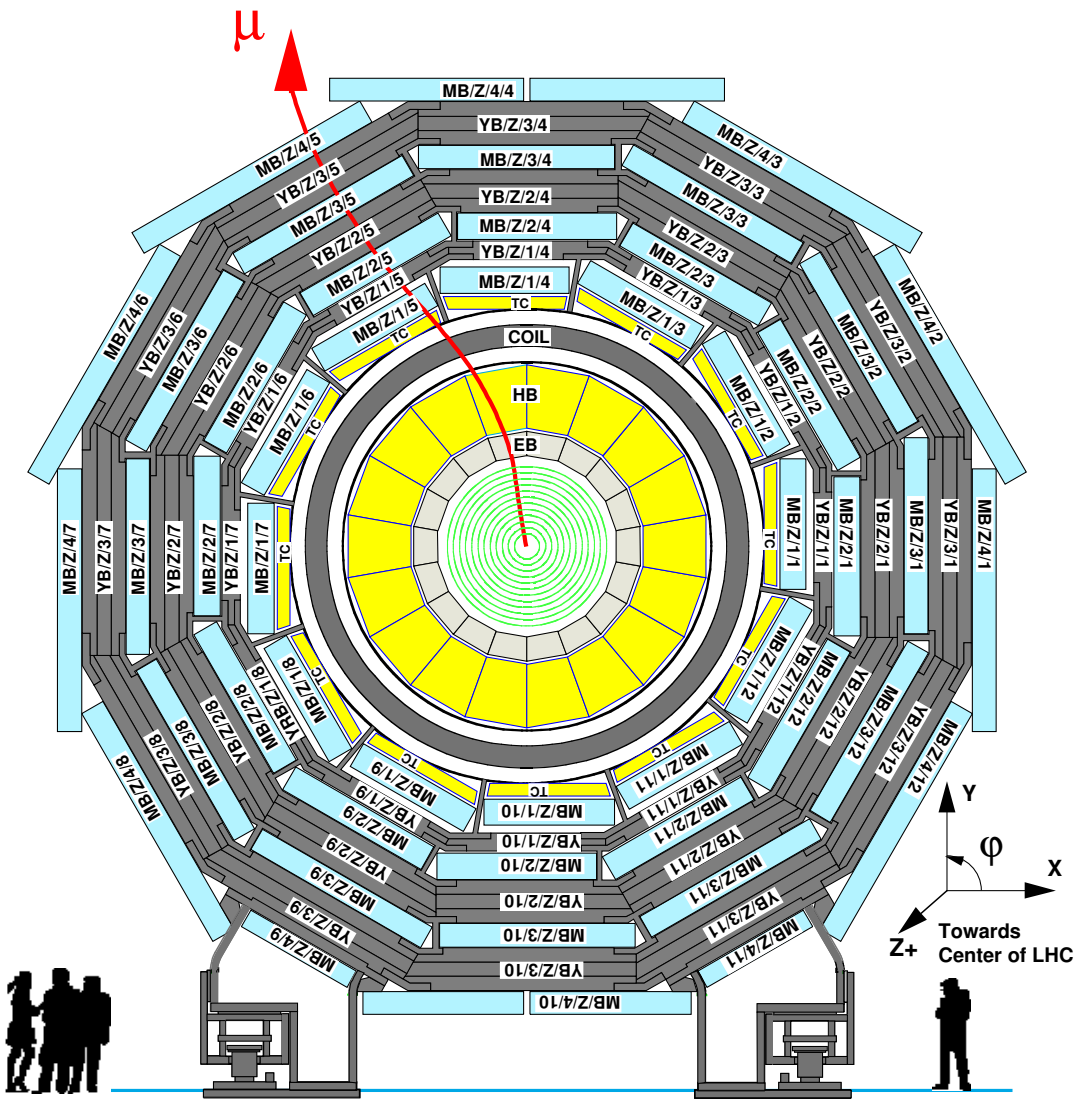

Figure 4.9: The layout of muon drift tube chambers (DT) in one of the five wheels. The layout in each wheel is identical with exception of wheels -1 and $+1$ where the presence of cryogenic chimneys for the magnet shortens the chambers in 2 sectors.

staggered by half a cell. The drift cell is 2.4 m long with the cross section 13×42 mm^2. A thin anode wire is stretched in the middle along the long side of it. The characteristic transverse dimension of the drift cell is 21 mm, thus the maximum drift time is 380 ns in the gas mixture of 85% Ar and 15% CO_2. The two superlayers on outside of the chamber have wires inside the cell parallel to the beam line, thus measuring the azimuthal angle. The superlayer inside the chamber has wires perpendicular to the beam line, thus measuring the z position. The z-measuring superlayer is not present in the last muon station.

The superlayer is a basic measuring unit of the DT station. Each superlayer delivers a time with respect to the bunch crossing, the position of the center of gravity, and the angle of the track segment with precision of few nano-seconds, 1.5 mm, and 20 $mrad$, respectively. The design and the precise mechanical construction of the DT chamber allowed them to achieve 100 μm precision in global $r - \phi$ position measurement.

Cathode Strip Chambers.

The cathode strip chambers (CSC), shown in figure 4.10, cover pseudo-rapidity ranges, $0.9 < |\eta| < 2.4$. The region between $0.9 < |\eta| < 1.2$ is covered by both DT chambers and CSC. The cathode strip chambers are trapezoidal in shape with a smaller side of the trapezoid positioned at the smaller radius. Each chamber is made of 7 cathode strip planes with strips in each plane running along the azimuthal angle ϕ. These cathode strip planes are interleaved with six anode wire planes with the wires running perpendicular to the strips. The only difference is in ME1/1 chambers, which are positioned inside the solenoid. The wires in ME1/1 are tilted at the Lorentz angle $\alpha_L = 29^\circ$ with respect to the perpendicular direction. This tilt is done in order to compensate for the Lorentz drift of the electrons. The single plane spatial single hit resolution in $r - \phi$ is 80 μm for ME1/1 and ME1/2 chambers, thus resulting in 80 $\mu m/\sqrt{6} = 33$ μm

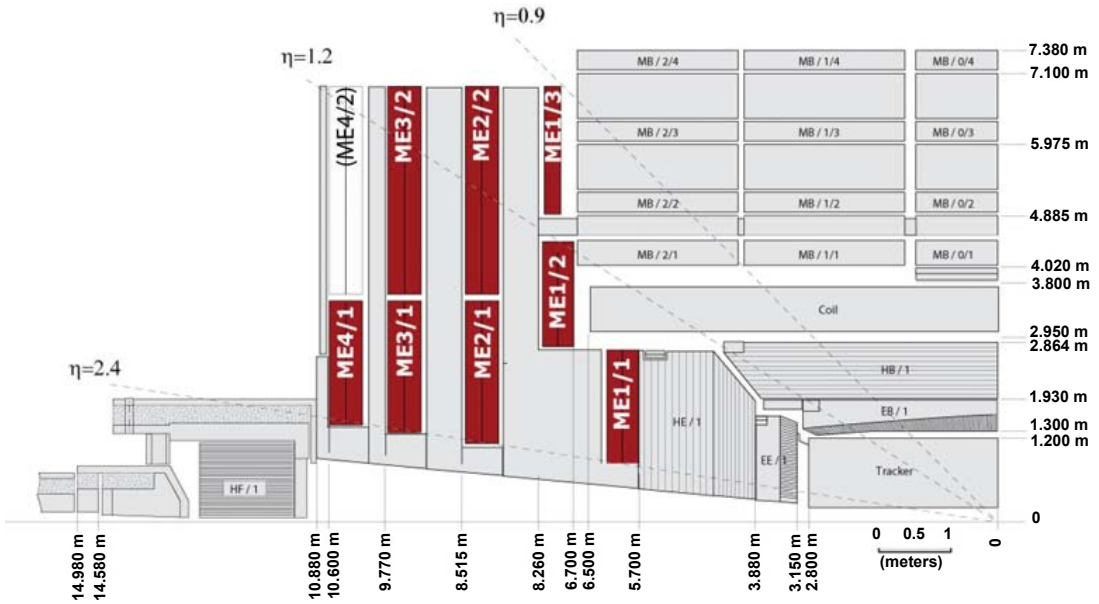

Figure 4.10: The layout of muon cathode strip chambers (CSC) in one quarter of the CMS. Most of the cathode strip chambers are highlighted in dark-red, the ME4/2 chamber is not highlighted, because it was thought that it would not be installed at the start-up of the LHC, but delays in the LHC start-up allowed for it to be installed for the first data.

spatial six-plane resolution. The spatial single hit six-plane resolution for all other chambers is $\sim 80\ \mu m$.

Resistive Plate Chamber System.

The primary purpose of the Resistive Plate Chamber (RPC) system is to provide fast and efficient trigger for muons. The reaction time of the RPCs is $\sim 1\ ns$, which much is shorter, than the 25 ns difference between the neighboring bunch crossings. Thus RPCs can provide precise bunch assignment. Moreover, they have an adequate spacial single hit resolution of the order of $\sim 1\ cm$.

In the barrel, see figure 4.11, RPC layout follows the layout of DT chambers. In the two inner rings the PRCs are positioned on both sides of the DT chambers. In the two outer rings the RPCs are positioned only on the inner side of the DT chambers.

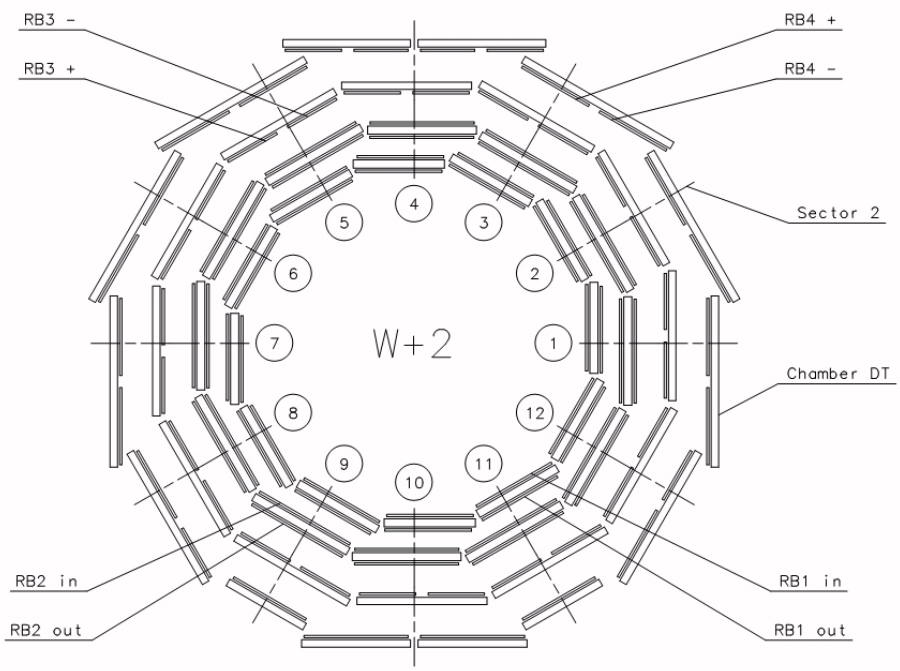

Figure 4.11: The layout of muon resistive plate chambers in the barrel.

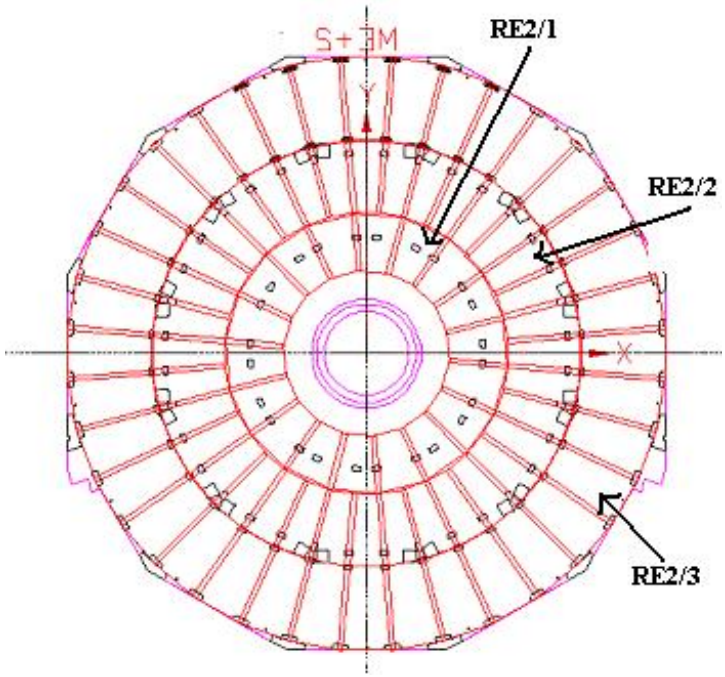

Figure 4.12: The layout of muon resistive plate chambers in the end-cap.

The layout of the RPC system in the end-cap is shown in figure 4.12. For the initial data-taking period, until the next long stop of the accelerator, the RPC coverage extends only to the pseudo-rapidity region $|\eta| < 1.6$.

4.3 Overview of the PLT project

PLT is an independent stand alone luminosity detector for the CMS based on pixelated single crystal diamond sensors. It designed to be self calibrating. With a projected relative luminosity accuracy measurement better than 1%!

4.3.1 Bump bonding diamond sensors to the readout chip

Talk to Bert.

4.3.2 Test Beam Results

Test beam at the CERN SPS

Talk to Steve, Bob, Will, Stefan and Matt

Test beam at the Fermilab m-Test

Talk to Bob, Will, Matt

4.4 Trigger system.

At the highest luminosity in the LHC, proton bunches will intersect inside the CMS detector every 25 ns. Each bunch crossing results in about 20 proton-proton interactions. These produce particles that make signals in the various sub-detectors of CMS, ultimately resulting in $\sim 1\ MB$ of information per bunch crossing or $\sim 40\ TB$ per second! With present technology, it is impossible to record every event at this rate. Moreover, not all events are interesting, thus one

must decide what to keep and what to discard. This is the job of the trigger system.

In CMS, the trigger decision, whether to keep or discard an event, is performed in two steps or levels. The process of making the trigger decision is called the trigger path. The trigger path starts at level one, or L1, where the trigger system performs decisions at the hardware level, using custom-designed programmable electronics. Then it passes the decision to the High Level Trigger (HLT), which decides at the software level, and makes the final decision on wether to record the event.

In order to be flexible, the L1 trigger architecture was implemented using Field Programable Gate Arrays (FPGA's) technology. However, in the case where either speed or radiation hardness was important, programable memory look-up tables (LUTs) and Application-Specific Integrated Circuits (ASICs) were used. The L1 trigger electronics is located partially on the detector and partially in the underground control room, approximately 90 m away from the detector.

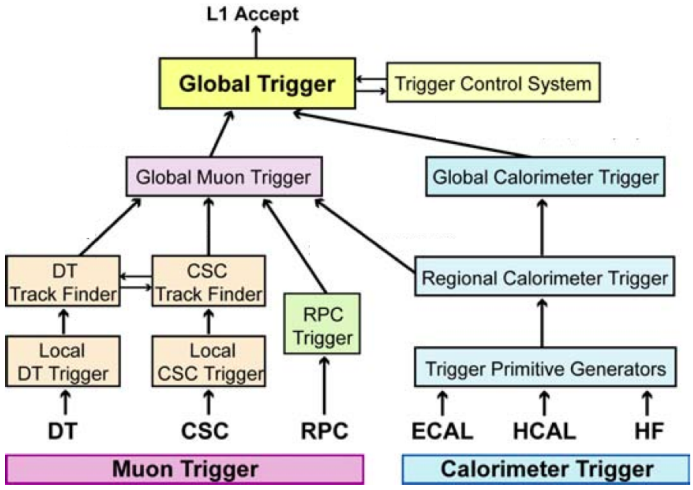

Figure 4.13: L1 trigger architecture.

The information flow of the L1 trigger is shown on the figure 4.13. The L1 trigger consists of local, regional, and global components. At the beginning of the path are the local triggers also called Trigger Primitive Generators (TPG).

They are based on calorimeter energy deposits for the calorimeter trigger or on hit patterns or track segments in the muon chambers for the muon trigger. Then, in limited spatial regions, the regional triggers combine the information from the local triggers and use it to rank and sort trigger objects, such as electron and muon candidates. The rank is determined based on the energy, the momentum and the quality of objects. Then, the ranked objects from the regional muon and calorimeter triggers are transferred to the global muon and calorimeter triggers, which select the highest ranked calorimeter and muon objects and pass them to the Global Trigger. The Global Trigger takes a decision whether to accept or reject the event, based on preprogrammed algorithm and on readiness of the sub-detectors and data-acquisition system (DAQ), the latter is determined by the trigger control system(TSC). The decision, L1 Accept (L1A), is communicated back to the sub-detectors by the trigger, timing, and control system (TTC).

The L1 trigger must analyze every bunch crossing. The allowed time for that analysis, latency, is 3.2 μs. This is the time difference between the moment when bunch crossing has occurred and the moment of communication of the decision back to the sub-detectors. Thus the sub-detectors have to store information about events within this time in the memory buffer, to allow for quasi-dead-time-free operation.

Once the decision, L1 Accept, has been made all event information is passed to the High Level Trigger (HLT). The HTL is implemented on the computer processor farm, also referred as "event filter farm". In oder make a decision to accept or to reject an event, the HLT uses full detector information. Thus it is able to make a more inform decision but it must analyze the event at the L1 trigger output rate, which was designed to be 100kHz. Therefore an efficient online event reconstruction algorithm has been designed.

The difference between the offline reconstruction algorithm (described in the next chapter 5) and the online reconstruction algorithm is that the latter has been

optimized for speed, while sacrificing the precision in the description of the event. Otherwise, they perform the same task. They use the information supplied by the detector about the event, in case of online reconstruction it uses the information passed by the L1 trigger, an estimation of the momentum, energy, direction, and position of the L1 trigger objects, as a seed. Then the HLT correlates this information with detector alignment and calibration constants, the beam parameters and other relevant experimental conditions. After that it passes all this information through sophisticated software algorithm to reconstruct the physical objects, such as for example, electrons and muons. Reconstruction procedure determines the parameters of the object, for example, transverse momentum, energy, and direction. Finally, the HLT uses the parameters of the objects to make the decision about keeping or rejecting the event.

The HLT decision program represents a chain of filter algorithms or HTL paths. Subsequent filters, using the parameters of the physical objects, make the decision whether or not to pass the event. If the event is passed, the information about the objects is passed along, in order to serve as a seed for the next step of decision path. Several HLT paths can run in parallel and brunch out into new paths. The event is only rejected, if decision to reject is made by all HLT paths.

Two important parameter describe the overall trigger path: The trigger rate, which determines how many events per second are passing this path and the pre-scale, which determines how often you pick an event, which have passed a certain trigger path. A pre-scale of 10 means that every 10^{th} event, passing this trigger path, is recorded on disk. The trigger paths can be pre-scaled on both L1 and HLT levels separately.

The trigger path is named after an object it uses to make the decision. For example the trigger path that makes the decision based on the parameters of the muon object is called the muon trigger. If it uses electron parameters then it is

called the electron trigger. The cross-triggers use parameters of more than more object, for example muon and electron.

One of the object's parameters that the trigger uses to pass an event is the transverse momentum of the object. In trigger lexicon it is called p_T threshold. The event that has an object with p_T, as determined by the offline reconstruction, higher, than the p_T threshold for this object, is passed.

Since the measurement of transverse momentum has a finite resolution, sometimes, the objects with higher "real" transverse momentum do not pass the trigger and objects with lower "real" transverse momentum do. Thus the efficiency of the trigger around the threshold value is not a simple step function but has a smooth rise. This rise in efficiency of the trigger around the threshold value is referred to as *the trigger turn on effect*.

The events, passing separate trigger paths, can in principle form their own datasets. In practice, the events in the dataset are usually grouped by some logical connection between trigger paths. For example, the 2010 Muon dataset combines almost all of the muon trigger paths. With exception of the muon based trigger paths that are used to trigger quarkonia (J/Ψ, Ω) candidates. And with the exception of the low threshold, hence highly pre-scaled, muon triggers that are used for trigger debugging. An example of the muon trigger path that is part of the Muon dataset is: "`OpenHLT_Mu7`" which, as the name suggests, has a 7 GeV threshold on the muons transverse momentum. It was seeded by "`L1_SingleMu5`", a L1 trigger with a threshold 5 GeV on the transverse momentum of the L1 muon object.

Chapter 5
Reconstruction and Identification.

Before the events, selected by the trigger and recorded by the data acquisition (DAQ) systems, can be analyzed the raw data has to be decoded. The output of the DAQ system consists of signal pulse heights, the time when the signal occurred, and the address of the detector element where it occurred. What we need to know are the particles which were produced in the collision, their energies, momenta, masses, and the coordinates of their origin.

Determining this information is the task of the off-line reconstruction software. First, it correlates the output of the DAQ system with the information about the geometry of the detector, the current values of all detector alignment and calibration constants, the beam parameters and other relevant experimental conditions. Then, it passes all this information through sophisticated computer algorithms, which attempt to reconstruct what happened in the collision. In order to do that, it employs knowledge about the standard model particles and their interactions and with the material of the detector. In the following sections, I will describe in detail the process of reconstruction and identification of all the objects used in this analysis: tracks, vertices, beam spot, electrons, muons, jets, and missing transverse energy.

5.1 Beam spot and vertex reconstruction.

When two proton bunches cross inside the detector, some of the protons in those bunches interact. Each hard collision produces multiple particles originating from

the point of collision. This point is called the *primary interaction vertex*. Since the proton bunches have a finite size, the collisions of individual protons do not always occur at exactly the same point. Instead, they are distributed over a finite volume. This locus of collision points is called the *beam spot*. The short-lived particles originating from the proton collision can decay some distance away from the primary interaction point with several secondary particles originating at the point of decay. This point is called the *secondary vertex*.

The beam spot position and the center of the CMS detector do not exactly coincide. In addition, due to changing LHC parameters and conditions the position of the beam spot may change with respect to the previous known position. As we will see in the next section, many track seeding steps use the beam spot location as a constraint to find the seed and to determine the initial seed parameters. Thus the precise knowledge of the beam spot position is important for efficient track reconstruction.

If the beam spot is displaced with respect to the center of CMS as indicated on figure 5.1a, there will be a correlation between the transverse distance of the point-of-closest-approach of the track to the CMS center (d_{xy}) and the azimuthal angle (ϕ) of the track as shown in figure 5.1b. We can parametrize this correlation to first order as follows:

$$d_{xy}(\phi, z_p) = x_{bs} \sin\phi + \frac{dx}{dz} \sin\phi z_p - y_{bs} \cos\phi - \frac{dy}{dz} \cos\phi z_p \tag{5.1}$$

where x_{bs} and y_{bs} are the beam spot position at $z = 0$, $\frac{dx}{dz}$ and $\frac{dy}{dz}$ are the slopes of the beam spot, and z_p is the longitudinal position of the track's point-of-closest-approach to the center of the CMS.

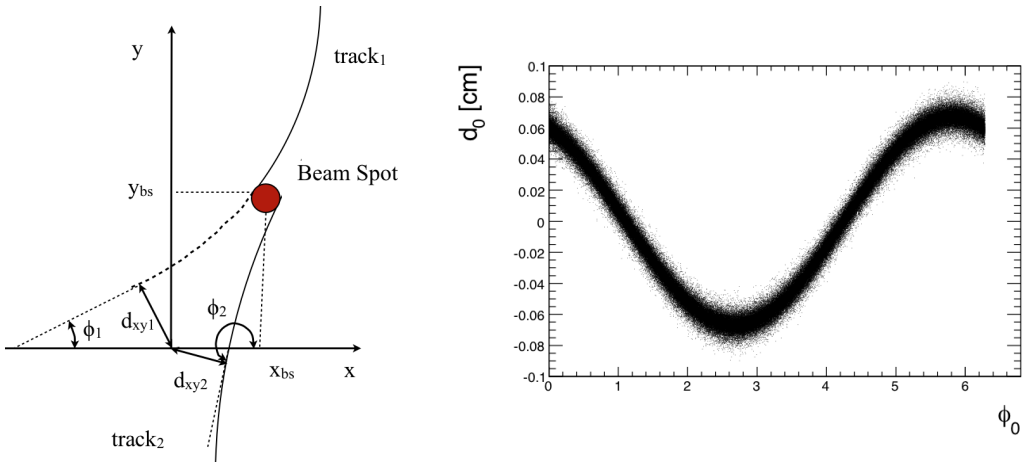

(a) (b)

Figure 5.1: (a) Shows two tracks originating from a displaced beam spot. The impact parameters d_{xy_i} and the azimuthal angles ϕ_i of each track are measured at the point-of-closest-approach of the track to the center of CMS. (b) Correlation between the track impact parameter d_0 and tracks azimuthal angle, ϕ, both measured at the point-of-closest-approach of the track to the center of CMS, when the beam spot is displaced with respect to the origin of the detector coordinate system by $x_{bs} = 300\mu m$ and $y_{bs} = 600\mu m$. Note that $d_0 = -d_{xy}$.

Thus, to determine the beam spot parameters (x_{bs}, y_{bs}, $\frac{dx}{dz}$, and $\frac{dy}{dz}$) we can use the above parametrization to fit the measured dependance between track's ϕ and d_{xy} by minimizing the following χ^2 distribution:

$$\chi^2 = \sum_{i=1}^{N_{Tracks}} \frac{(d_{xy_i} - d_{xy}(\phi_i, z_{pi}))^2}{\sigma^2_{dxy_i} + 2\sigma^2_{Beam}} \tag{5.2}$$

where the d_{xy_i} is the measured value of the track's impact parameter with respect to the CMS coordinate center for the i^{th} track, $d_{xy}(\phi_i, z_{pi})$ is the value of track's impact parameter obtained from the parametrization 5.1, $\sigma^2_{dxy_i}$ is the error on the track's impact parameter determined from the track's fitting procedure (as explained in the following section), and the σ^2_{Beam} is the average transverse beam width. An example of the beam spot parameters during one of the LHC fills is given in table 5.1.

beam spot parameters					
x_{BS}	y_{BS}	z_{BS}	$\sigma_{x_{BS}}$	$\sigma_{y_{BS}}$	$\sigma_{z_{BS}}$
960 μm	90 μm	0.5 cm	30 μm	30 μm	$3.5 - 5.0 cm$

Table 5.1: Approximate positions and widths of the beam spot during LHC fill 1089, [15].

The task of reconstructing primary vertices subdivides into vertex finding and vertex fitting. The primary vertices are found by sorting all tracks in the event into subsets with a common origin. First the tracks having a small impact parameter with respect to the beam-line are selected. Then the selected tracks are clustered together based on the z-coordinate of the track's point-of-closest to the beam-line, the clusters are split if the track is further than 1 mm away in z from its nearest neighbor. Then using these groups of tracks the vertex candidates are fitted by an adaptive vertex fitter [16]. The fitter assigns each track a weight,

$$w_i = \frac{\exp(-\chi_i^2/2T)}{\exp(-\chi_i^2/2T) + \exp(-\sigma_{cut}^2/2T)} \ ,$$

with

$$\chi_i^2 = d_i^2/\sigma_{d_i}^2 \ ,$$

where d_i and σ_{d_i} are the track's 3D distance to the vertex and its error, the σ_{cut}^2 defines the cut on the track's χ_i^2, and T defines the softness of this cut (i.e. if $T = 0$ the cut is the hardest). The value of T is chosen by trial and error. Each fitted vertex is then assigned a number of degrees of freedom, defined as:

$$n_{dof} = 2 \sum_{i=1}^{nTracks} w_i - 3 \tag{5.3}$$

5.2 General track reconstruction.

Measuring the parameters of the trajectory of a charged particle in the magnetic field allows us do determine the kinematic properties of the associated particle. In first order, this trajectory is a helix with an axis along the magnetic field. It is characterized by five parameters: The curvature, with radius, R, proportional to the transverse momentum ,p_T, of the particle and with direction of curvature related to the sign of the particle, the distance of the closest approach of the helix to the beam spot both in perpendicular, $d_{xy}(bs)$, and along, $d_z(bs)$, magnetic field planes, and the angles, ϕ and θ, its makes at the point of closest approach (PCA) with the x-axis in the plane perpendicular to the magnetic field and with the z-axis in the plane parallel to the magnetic field. All five parameters are shown in figure 5.2. In second order, the trajectory is affected by the energy losses of

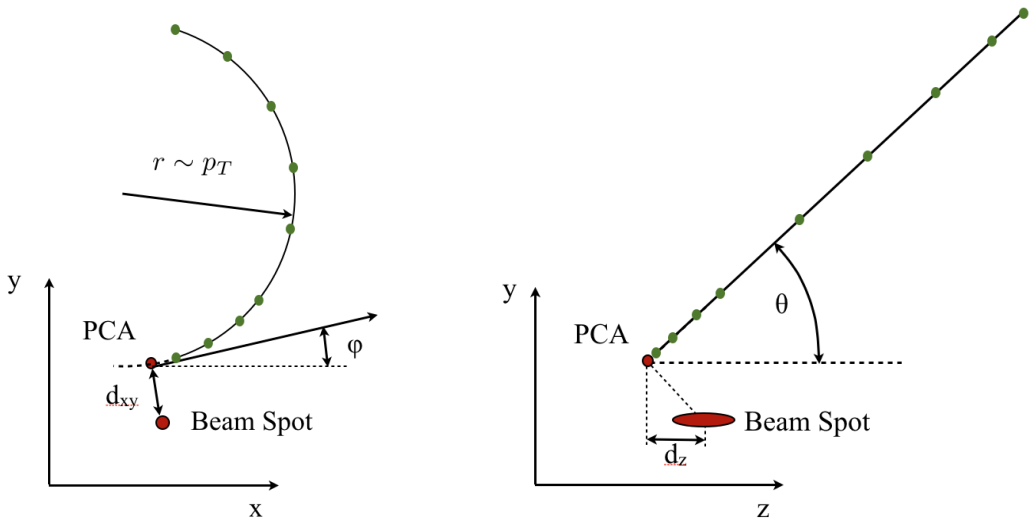

Figure 5.2: Schematic views of a particle's trajectory in $r-\phi$ plane (left) and in $r-z$ plane (right) showing five trajectory parameters. In $r-\phi$ plane: the radius of the trajectory which is proportional to the transverse momentum of the particle, $r \sim p_T$, the 2D distance from the beam spot to the point-of-closest-approach (PCA), $d_{xy}(bs) = (x_{PCA} - x_{BS})\sin\phi - (y_{PCA} - y_{BS})\cos\phi$, and the azimuthal angle of the trajectory at the PCA, ϕ. In $r-z$ plane: the z-coordinate of the PCA with respect to the beam spot $d_z(bs) = z - z_{BS}$ and the polar angle θ at the PCA, in track reconstruction the $\cot\theta = \frac{p_z}{p_T}$ is commonly used. Magnetic filed is along z.

the particle due to radiation and interaction with the material of the detector, by small angle multiple scatterings, and by the non-uniformity of the magnetic field. Thus, by knowing the parameters of particle's trajectory at various points in the detector, we will know the location of the particle's origin, its momentum, the sign of its charge, and how much energy it has lost while traversing the detector.

As a charge particle traverses the detector it leaves a trace of small energy deposits in each tracker sensor its crosses. Thus to find the parameters of the trajectory of the particle we need to determine the positions of these energy deposits and then reconstruct the trajectory from those positions. This task is performed by the track reconstruction software.

The track reconstruction in CMS is performed in six iterations [17]. Each iteration starts with a different set of seeds, which are the rudimentary trajectories defined by a minimum of three points, and then proceeds using the same algorithm for each iteration. The multi-iteration track finding significantly improves the efficiency of reconstructing tracks, especially those with large impact parameters, while keeping the number of fake tracks low. Each iteration consists of five steps described below.

First, in each sensor the clusters are formed out of contiguous sets of strips or pixels with signal above threshold. Then the signal distribution between the pixels or the strips in a cluster is analyzed, using the templates developed during test beam experiments, and the hits (also called recHits) are formed. The hits carry information about the position and the error on the position.

In the second step, trajectory seeds are generated using a minimum of three tracker hits with three-dimensional position measurements. As mentioned above the seeds for each iteration are constructed differently. Since more than 90% of the charged particles produced in the proton-proton collisions will cross three pixel layers, provided they are inside the geometrical acceptance of the tracker, the seeding in many iterations starts in the pixel detector. Overall, four types of

seeds are used. Pixel triplets give the most precise estimation of the trajectory parameters, hence they are used first. In order to find them, a loose beam spot constraint is used to filter out trajectories that did not originate in the interaction region, but once the seed is constructed the beam spot position is not use to estimate the initial trajectory parameters. Another type of seeds are pixel and strip pairs with vertex constraint. They use vertices reconstructed using tracks from the previous iteration. The vertex constraint is used to build the trajectory then it is removed before determining the final trajectory parameters. The third type of seeds are pixel and strip pairs with beam spot constraint. Although it is similar to the previous type, the looser beam spot constraint helps to recover the long-lived hadronic decays, such as pions and kaons. The forth type of seeds are the strip only pairs with beam-spot constraint, which use three-dimensional strip measurements to construct seeds for trajectories which may not have had any pixel hits. As before, the beam spot constraint is removed before determining the final trajectory parameters. The seeds for each iteration are summarized in table 5.2.

Iteration	Seeding Layers	p_T	d_{xy}	d_z	Constraint
		GeV	cm	cm	
0	pixel triplets	0.5	0.2	15.9	beam-spot
1	pixel/strip pairs	0.9	0.2	0.2	vertex
2	pixel triplets	0.075	0.2	17.5	beam-spot
3	pixel/strip pairs	0.35	1.2	7.0	beam-spot
4	strip pairs	0.5	2.0	10.0	beam-spot
5	strip pairs	0.8	5.0	10.0	beam-spot

Table 5.2: The parameters used to build seed-trajectories for each iteration. The d_z and d_{xy} were calculated with respect to CMS center, except where the vertex constraint was used, then both d_z and d_{xy} were calculated with respect to the interaction vertex. In all cases the constraint was not used to determine the final trajectory parameters.

In the third step the trajectories are built using a Combinatorial Track Finder (CTF) algorithm [18] which is based on the Kalman filter method. The Kalman

filter method was developed by Rudolf E. Kalman in the context of random signal processing to solve the problem of separating random signals from random noise. The key idea of the method is to use not only the empirical description of the phenomena but to also employ the underlying physical laws that govern the behavior of the phenomena in order to produce a more precise prediction of the next state of this phenomena [19]. In the application to track finding, the Kalman filter uses not only the weighted average of the previous measurements of the trajectory but also the law of motion of the charged particle in the magnetic field in oder to predict the next trajectory measurement.

Starting from the seed the combinatorial track finder builds the trajectory a hit at a time, a new hit is added if the χ^2 of the trajectory calculated with this hit is smaller then a predetermined value. If several hits pass this criteria, then several new trajectories are created. In addition, a trajectory with no hit in a layer is also created to account for the possibility of detector inefficiency. This absent hit is called "invalid" hit. However, the trajectory is not allowed to have two "invalid" hits in a row at the building stage.

The track finding algorithm can result in several trajectories stemming out from the same seed. Also, because multiple trajectories are built simultaneously, several trajectories originating from different seeds may merge. These ambiguities are resolved in the fourth, "cleaning", step. The number of shared hits between two the trajectories is examined:

$$f_{shared} = \frac{N_{shared}}{min(N_1^{hits}, N_2^{hits})}$$

If f_{shared} is more than 50% then the trajectory with the least amount of hits is discarded. If both trajectories have the same amount of hits then the trajectory with the higher chi-square is discarded.

This leads to the final fit step in which the trajectories are re-fitted again using the Kalman filter method. The residual errors of each hit are re-evaluated after the final fit and the hits with a residual error larger than a predetermined value are discarded and replaced by the "invalid" hits. After a hit has been discarded, the track is re-fitted again and new hit residual errors are calculated. This procedure is repeated until the residual errors of all hits are smaller then the predetermined threshold.

Before proceeding to the next iteration, the quality of the tracks is evaluated according to a complex criteria [20]. It uses the relations between the track's probability to be a "ghost" track (not corresponding to a real particle) and the track's parameters, such as pseudo-rapidity, transverse momentum, number of tacker layers crossed, χ^2 of the track and compatibility with the beam spot and the primary vertex. The criteria was optimized, using simulated events, to maximize the rejection of "ghost" tracks (tracks not matching to a simulated track) and minimize the rejection of real tracks. The full set of parameters and corresponding cuts is listed bellow:

- The track chi-square per degree of freedom,

  $\chi^2/\nu < \alpha_0 n_{layers}$

- The track transverse distance to the beam spot,

  $|d_{xy}| < (\alpha_1 n_{layers})^{x_1} \sigma_{d_{xy}}(p_T)$

- The track longitudinal distance to the closest primary vertex,

  $|d_z| < (\alpha_2 n_{layers})^{x_2} \sigma_{d_z}(p_T, \eta)$

- Transverse compatibility with beam spot,

  $|d_{xy}|/\delta d_{xy} < (\alpha_3 n_{layers})^{x_3}$

- Longitudinal compatibility with the closest primary vertex,

$$|d_z|/\delta d_z < (\alpha_4 n_{layers})^{x_4}$$

where

$$\sigma_{d_z}(p_T, \eta) = \sigma_{d_{xy}}(p_T) = a + \frac{b}{p_T}$$

and the n_{layers} is the number of layers crossed by a track. The values for the parameters used in the cuts above to select the tracks with "high purity" and with "loose" quality criteria are listed in table 5.3. Although the criteria to determine

Quality type	α_0	α_1	α_2	α_3	α_4	x_1	x_2	x_3	x_4	$\frac{a}{\mu m}$	$\frac{b}{\mu m}$
High Purity	0.7	0.3	0.35	0.4	0.4	4	4	4	4	30	10
Loose	1.6	0.55	0.65	0.55	0.45	4	4	4	4	30	100

Table 5.3: The cuts used to select high purity and loose quality tracks.

the quality of the tracks is quite complex, it can be loosely summarized as follows. If the track crossed ten or more layers, then it is kept. However, for tracks with fewer number of measurements the quality criteria strongly depends on a number of crossed layers, the value of transverse momentum and pseudo-rapidity of the track.

After the tracks with a passing quality have been selected, the hits that belong to them are removed from the pool of available hits and a new iteration starts with a smaller collection of hits. During the first iteration only the tracks passing the "high purity" criteria are selected, while in later iterations the selection criteria is relax to maximize the efficiency.

On a final note, all tracks in the central tracker reconstructed with the CTF algorithm compose the "general track collection". This collection, however, does not include either the local, also called the stand-alone, tracks reconstructed in the muon detectors, or the global muon tracks with hits in both the tracker and the muon detectors. It also does not include the electron tracks reconstructed by the Gaussian sum filter algorithm, which will be described in the next section,

although it does include electron tracks that are reconstructed with the CTF algorithm. Thus, care must be taken to avoid double counting when using tracks from several different collections.

5.3 Electron reconstruction and identification.

Electrons originating at the primary interaction vertex, *prompt*, and not in the neighborhood of other particles in the event, *isolated*, are part of the multi-leptonic signature that we are searching for. Thus, its unambiguous identification and the precise determination its parameters are important tasks, that is performed by the electron reconstruction and identification algorithms. Electron reconstruction is done by combining measurements in the electromagnetic calorimeter with measurements in the tracker.

While traversing the tracker, an electron encounters a large amount of material and loses energy by emitting bremsstrahlung photons, see figure 5.3. Although

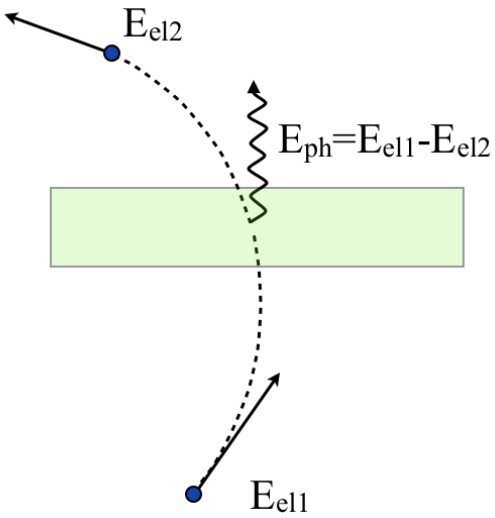

Figure 5.3: Electron with energy E_{el1} traversing the material emits bremsstrahlung photon, thus loosing energy $E_{el2} = E_{el1} - E_{ph}$. The photon is emitted at a tangent to electron's trajectory. The magnetic filed is perpendicular to the plane of the picture.

the electron travels along a curved trajectory, the radiated photons travel in a

straight line on a tangent to the electron trajectory. Thus the pattern of energy deposits in the calorimeter is a narrow trail of clusters in the ϕ direction, left by each radiated photon along with the electron itself. In order to calculate the total energy of the electron, these clusters are combined into one super-cluster. The reconstruction of the electron super-cluster is done first by combining individual calorimeter towers with energy above threshold into clusters, then, combining all clusters along a narrow strip in phi into the super-cluster, see figure 5.4.

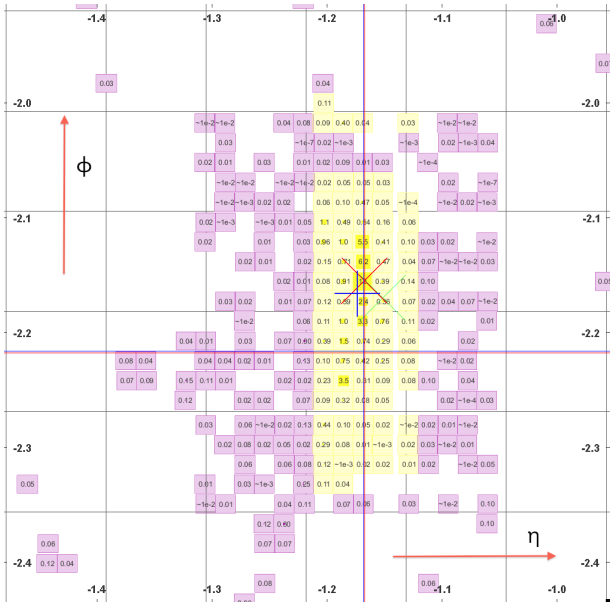

Figure 5.4: Electromagnetic calorimeter towers grouped into electron supercluster (yellow). The pink are unclustered towers. Blue cross + indicates supercluster centroid. Green × indicates direction of the electron at vertex. Red × indicates seed cluster centroid. The azimuthal angle ϕ is along the vertical axis and pseudo-rapidity η is along the horizontal axis. The image is produced in CMS visualization software cmsShow [1].

The reconstruction of the electron track differs from the reconstruction of the tracks of minimum ionizing particles described in previous section. The trajectory parameters can not be deduced by using a Kalman filter, because it assumes a simple Gaussian distribution of energy loss, while the electron energy loss due to bremsstrahlung photons has large non-Gaussian tails. The energy loss

by bremsstrahlung can be approximated using the following probability density function (see the original article by Bethe and Heitler [21])

$$f(z) = \frac{[-\ln z]^{c-1}}{\Gamma(c)}, \tag{5.4}$$

with $c = t/\ln 2$, where t is the length of the path of the electron in the material in units of radiation length, where z is the fraction of the electron energy remaining after the electron has traversed the material. This distribution is sharply peaked at one but has very long tails. This means that although the majority of electrons lose very little energy, some of the electrons lose more than 50%. Thus, to gain the efficiency in reconstructing electrons in the tails of this distribution a modified version of the Kalman filter is used, known as the Gaussian Sum Filter (GSF). This filter uses the probability density function, equation 5.4, which is approximated by a weighted sum of gaussians, instead of a simple gaussian probability distribution of energy loss.

The amount of CPU time that the GSF uses to re-fit a track is much longer than the time required by the Kalman filter. Thus the preselection of track seeds is made by using the super-cluster. The seeding method uses the fact that due to conservation of momentum the center of mass of the super-cluster does not depend on emission of bremsstrahlung photons. From the position of the center-of-mass of the super-cluster and from the total super-cluster energy the position of the hits in the pixel detector and most of layers of the strip detector can be inferred. Of course, since the super-cluster does not identify the charge of the electron, the tracks of both signs have to be checked.

The identification of the electron makes use of both supercluster and tracker variables. Below I list the variables of the "simple cut based identification" method [22], which is used in our analysis. The distributions of these variables for simulated events are shown in figure 5.5.

- Had/Em — The ratio of hadronic to electromagnetic energy in the supercluster, an electron should deposit all its energy in the electromagnetic calorimeter.

- $\sigma_{I\eta I\eta}$ — the square of the energy weighted width in pseudo-rapidity of the super-cluster, this width should be narrow for the electron.

- $|\Delta\eta_{in}| = |\eta_{sc} - \eta_{in}^{extrap.}|$ and $|\Delta\phi_{in}| = |\phi_{sc} - \phi_{in}^{extrap.}|$ — the distance between the position of the GSF track extrapolated from the innermost measurement of the track to the electromagnetic calorimeter surface $(\eta_{in}^{extrap.}, \phi_{in}^{extrap.})$ and the center-of-mass of the super-cluster (η_{sc}, ϕ_{sc}). As mentioned previously, the position of the center-of-mass of the super-cluster does not depend on whether or not the bremsstrahlung photons were emitted.

Table 5.4 shows the cuts on the electron ID variables, which are used for working point 90 (WP90). These cuts give roughly a 90% efficiency in selecting signal electron in both barrel and end-caps.

Electron WP90		
Variable	barrel	end-cap
Had/Em	< 0.12	< 0.05
$\lvert\sigma_{I\eta I\eta}\rvert$	< 0.01	< 0.03
$\lvert\Delta\phi_{in}\rvert$	< 0.8	< 0.7
$\lvert\Delta\eta_{in}\rvert$	< 0.007	< 0.009

Table 5.4: Electron ID cuts for working point 90.

As mentioned in section 4.2.2, a photon passing through material will convert into electron-positron pair. Special care is taken to identify and reject electrons originating from converted photons [3]. Prompt electrons should have hits in all layers of the pixel detector. A search for a conversion track pair is performed among all CTF tracks within a cone $\Delta R = \sqrt{\eta^2 + \phi^2} = 0.3$ that have a sign opposite of the electron sign. The distance quantity, called *Dist*, to the nearest

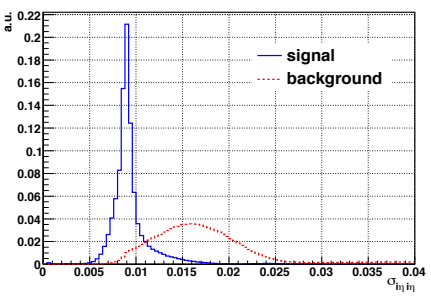

(a)

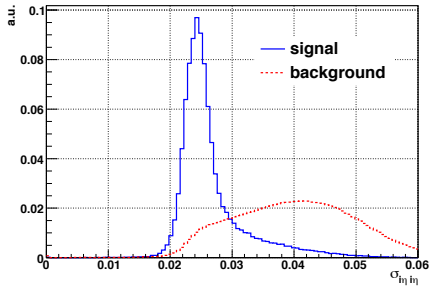

(b)

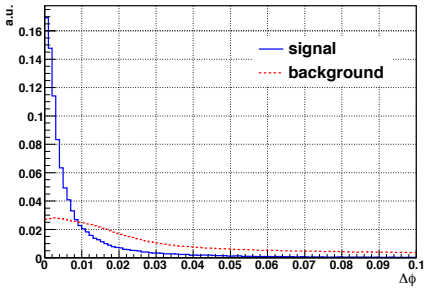

(c)

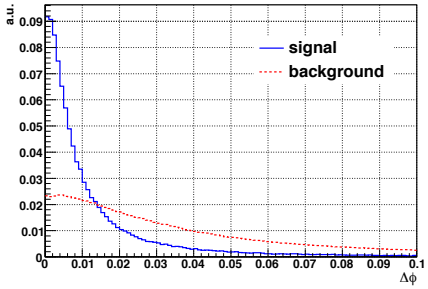

(d)

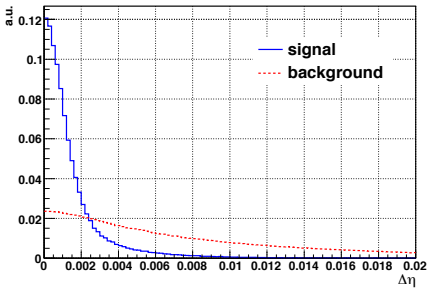

(e)

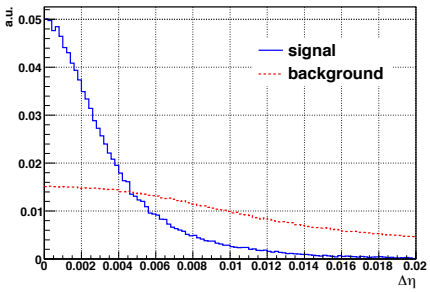

(f)

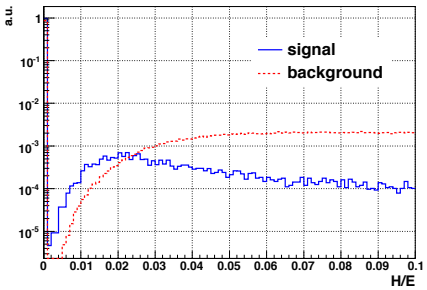

(g)

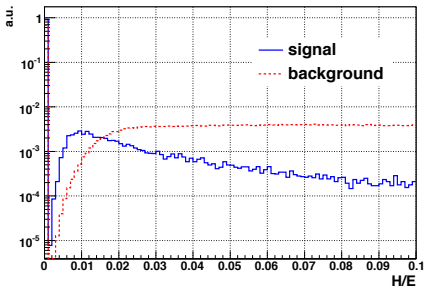

(h)

Figure 5.5: Electron ID variables for barrel (left) and end-cap (right): (a-b) $\sigma_{i\eta i\eta}$, (c-d) $\Delta\phi_{in}$, (e-f) $\Delta\eta_{in}$, and (g-h) H/E. The signal and the background are the reconstructed electron matched and not matched to the simulated electrons, for more detail see [2].

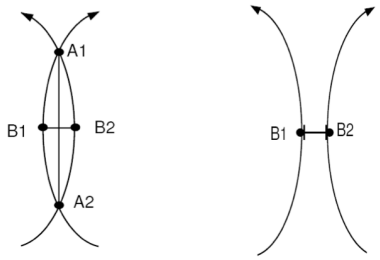

Figure 5.6: Two dimensional (in $x-y$ plane) distance between tracks is calculated at the point where two tracks are parallel. The distance is negative if tracks intersect each other and positive otherwise.

opposite sign track is calculated as shown on figure 5.6. A minimum difference in the cotangent of the polar angle with respect to the preselected CTF tracks, as above, is also used to find the conversion partner track,

$$\Delta \cot(\Theta) = \cot(\Theta_{CTF\ track}) - \cot(\Theta_{GSF\ track}) \ .$$

Also, the closest distance, $d_{xy}(bs)$, between the electron's trajectory and the beam spot in $x-y$ plane is used to select the prompt electrons and to reject electrons originating from long lived decays of hadrons, electrons emitted in interaction of primary collision particles with the nuclei of the material, so called *nuclear interactions*, and electrons originating from photon conversions. Their distance should be small for prompt electrons. Figure 5.7 shows the distribution of the variables used for rejecting electrons from photon conversions. Table 5.5 shows the cuts designed to reject 85% of converted photons while having a 95% efficiency in selecting prompt electrons [3].

Finally, electrons originating from the decays of W and Z bosons, as well as from the SUSY cascade decays, should not have any other particle in close proximity to them, in other words, they should be isolated. The degree of isolation from charged particles is determined in the tracker and from the electromagnetic and hadronic energy deposits in the calorimeters. The isolation is calculated by summing up the energy of all particles in a hollow cone, centered on electron track.

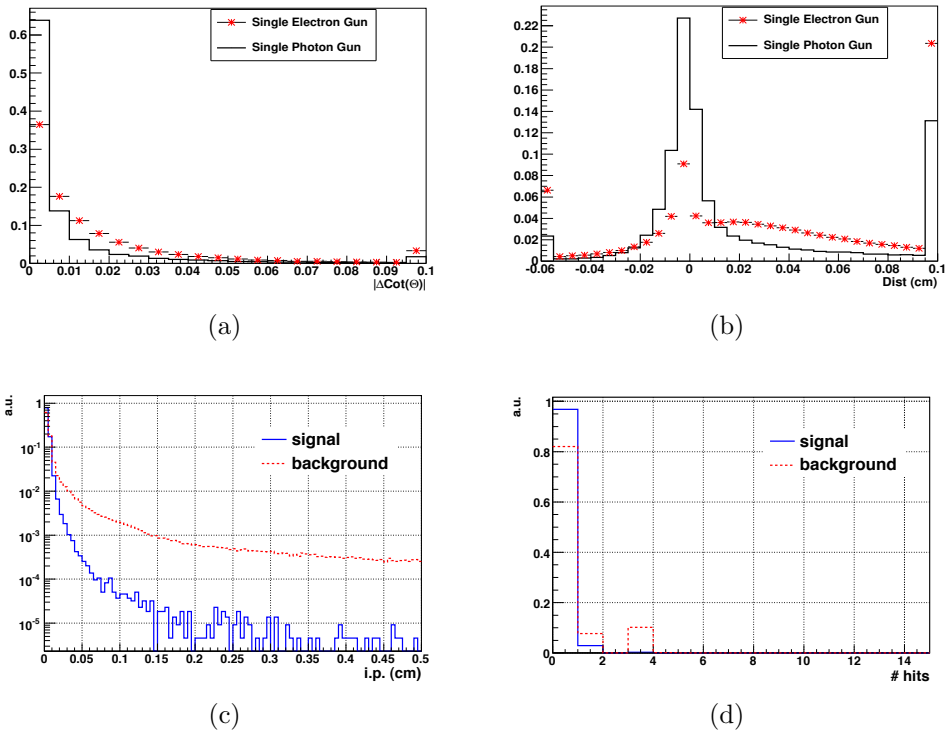

Figure 5.7: Variables for rejecting electrons from converted photons, long lived decays, and nuclear interactions. (a) and (b) show $|\Delta \cot(\Theta)|$ and *Dist* (cm), red asterisks correspond to background electrons from converted photons, solid black lines correspond to prompt electrons, for detail see [3]. (c) and (d) show $|d_{xy}(bs)|$ and *Number of missing hits*. The signal and the background correspond to the reconstructed electrons matched and not matched to the simulated electrons, for more detail see [2].

Conversion rejection	
Variable	cut
Dist	> 0.2
$\cot(\Theta)$	> 0.2
Number of missing pixel hits	≤ 1
$\lvert d_{xy}(bs)\rvert$	$< 0.02\ cm$

Table 5.5: Cuts used for rejecting electrons from the conversions of photons. The $|d_{xy}(bs)|$ and the *Number of missing pixel hits* variables also help to reject electrons originating from nuclear interactions and long lived decays, i.e. non-prompt electrons.

The inner, hollow part of the isolation cone, is called a veto cone. Its purpose is to exclude the energy deposits which may have been due to the electron itself.

In the tracker the scalar sum of the transverse momentum of all tracks with transverse momentum $p_T > 0.7\ GeV$, distance to the vertex of $d_{xy}(pv) < 0.2\ cm$, and within a hollow cone $0.04 < \Delta R < 0.3$ is calculated.

The isolation deposits in the electromagnetic calorimeter are calculated by summing up all transverse energy in a hollow cone with outer radius $\Delta R < 0.3$ and inner cone radius of three calorimeter crystals ($\Delta R \approx 0.05$ in the barrel). In order to exclude energy from bremsstrahlung photons, the deposits from a narrow strip along the azimuthal direction with a width in η of three calorimeter crystals are excluded. Also, to exclude noise a threshold of $E = 0.08\ GeV$ in the barrel and $E_T = 0.1\ GeV$ in end-cap was applied to all crystals in order to be considered for calculation of isolation deposits.

The isolation deposits in the hadronic calorimeter were simply calculated by summing up all hadronic calorimeter towers with the energy above 0.7 GeV in the barrel and 0.8 GeV in end-cap using a hollow cone with outer radius of 0.3 and the veto cone radius of 0.15.

The common measure of electron isolation is the combined relative isolation, which is the sum of all the above mentioned isolation deposits divided by the value of the transverse momentum of the electron. The cuts on the combined relative isolation, which are used in this analysis, are listed in table 5.6. These cuts are designed to keep more than 97% of prompt electrons and reject more than 92% of electrons from decays of heavy flavor hadrons [23].

5.4 Muon reconstruction and identification.

Identification and reconstruction of prompt isolated muons carry same priority as electrons, since they have the same importance in our signatures. Because

Isolation		
	Variable	cut
Barrel	$\frac{max(iso_E - 1,\ 0) + iso_H + iso_T}{p_T}$	< 0.15
End-cap	$\frac{max(iso_E,\ 0) + iso_H + iso_T}{p_T}$	< 0.15

Table 5.6: Electron isolation cuts. Note that 1 GeV pedestal subtraction is applied only in the barrel of the electromagnetic calorimeter.

of the nature of the CMS detector, identification of muons is more efficient and misidentification contamination is much less than for electrons. Muons are much heavier than electrons and therefore their energy loss materials is much less. Thus they leave only a track in the central tracker system, a small energy deposit in the calorimeters, and penetrate the calorimeters, the solenoid, and the return yoke steel leaving a track in the muon system.

The reconstruction of muons is similar to the reconstruction of tracks. In the central tracker the muon tracks are reconstructed together with all the other general tracks using the Combinatorial Track Finder described in section 5.2.

The tracks in the muon chambers, so called *stand-alone muons*, are also reconstructed using the same algorithm. The only difference is in the generation of the seeds, which are generated in the muon systems instead of the central tracker. The magnetic field in the muon systems is concentrated in the solenoid's return yoke, whereas the value of the magnetic field in the muon chambers is much lower. Thus the trajectory of the muon inside of the individual chamber is a straight line segment. Therefore, to find a seed, a single or a pair of such segments is searched for using a rough geometrical approach based on the premise that muons originate from the interaction point.

After generating the seed the reconstruction follows the same procedure as an iteration of the track reconstruction in the tracker. In order to improve momentum resolution the final fit of the stand-alone muon track in the muon chambers is done with the interaction point constraint.

The reconstruction of the tracks that use hits in both the central tracker and the muon systems (so called *global muon* tracks) begins after the reconstruction of tracks in the central tracker (called here *tracker tracks* to avoid confusion with tracks in other systems) and the reconstruction of the stand-alone muons is finished. In the first step, the stand-alone muons and the tracker tracks are matched. For each stand-alone muon track a subset of the tracker tracks is chosen based on loose cuts on the spatial variables and momentum difference. Then all the pre-selected tracker tracks are *propagated out* to a common surface between the central tacker and the muon chambers, while stand-alone muon tracks are *propagated in* to the same surface. Then the parameters of the trajectories of the tracker tracks and of the stand-alone muon track on that surface are compared. If no match is found based on predetermined matching criteria, then the best pick is chosen based on loose cuts on the direction of the tracker track and the stand-alone muon at the interaction point. In the next step, a global fit is performed using hits in the tracker track and the stand-alone muon track. Since the procedure above may match several tracker tracks to the same stand-alone muon track, the global fit attempts to fit all matched pairs. If more than one global muon results for each stand-alone muon, then the one with the best χ^2 is selected. Thus in the end only one global track for each stand-alone muon track is reconstructed.

The third type of muons are *tracker muons*, which are tracker tracks matched to at least one segment in the muon chambers. The tracker muon algorithm starts with a tracker track above a certain momentum or above a certain transverse momentum. The tracker track is then propagated to the muon chambers where the association of this track to the segments in the muon chambers is performed

based on predetermined cut on its position errors there. Tracker tracks with at least one associated segment are kept and stored in the tracker muon collection.

The algorithm that reconstructs tracker muons does not resolve ambiguities. Multiple tracker muons can be associated to one segment and vice versa multiple segments can have the same tracker muon associated with them. in order to resolve these ambiguities, *arbitration* is performed. There are many arbitration methods implemented in the muon reconstruction software. Most of them are based on comparing various parameters of tracks and associated segments. The result of the arbitration is used in tracker muon identification.

However, in this analysis we do not use arbitration of the tracker muons, since we never use tracker muons alone without other muon identification variables. Because the reconstruction of the tracker muon proceeds from "inside-out" whereas the reconstruction of the global muon proceeds from "outside-in" the algorithms are complimentary to each other. Thus, in our analysis we always require that each tracker muon should also be reconstructed as a global muon and vice versa.

To identify prompt muons coming from the interaction vertex both the quality of the tracker track and of the global muon track are considered. Among the parameters of the tracker track we use the following:

- The distance of point-of-closest approach in $x - y$ plane to the beam spot, $d_{xy}(bs)$, should be small for prompt muons.
- The z-coordinate of the PCA with respect to the primary vertex $d_z(pv)$, should be small for prompt muons.
- The number of valid hits on the tracker track, $N_{hits}^{tracker}$ (see definition in section 5.2), should be equal to the number of crossed layers. Usually a constant minimum number is used for all pseudo-rapidity ranges.

In addition we use the following the global muon parameters:

- The chi-square divided by the number of degrees of freedom, $\chi^2/ndof$, of the global muon track should be small, since global tracks of good muons should not have large kinks either.

- The number of valid hits in the muon chambers, N_{hits}^{muon}, should not be zero for the same reason as above. The stand-alone muon tracks and the tracker tracks ideally should match.

The distributions of some of the muon identification variables are shown in figure 5.8.

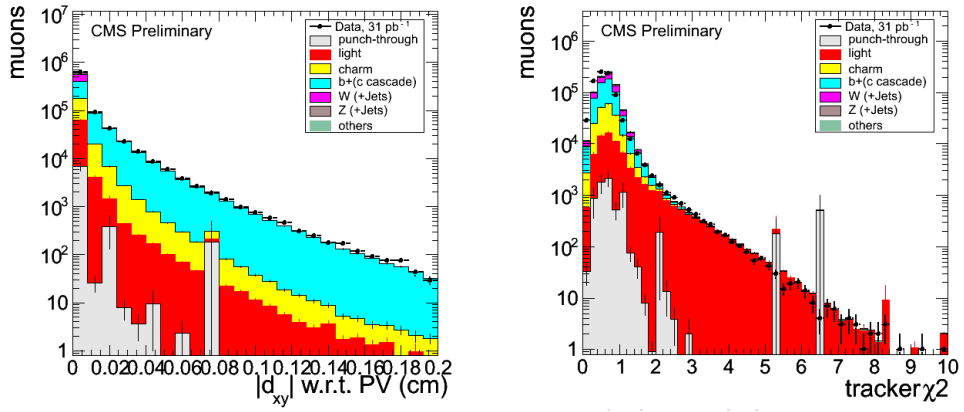

(a) (b)

Figure 5.8: Muon ID variables. (a)The distance $d_{xy}(pv)$ in the $x-y$ plane of the muon's closest approach to the primary vertex. (b) The χ^2 of the tracker track. Both distributions are taken from [4].

The isolation of the muon is measured in the tracker, in the electromagnetic calorimeter, in the hadronic calorimeter, and in the outer hadronic calorimeter. In all cases a hollow cone around the muon with the outer radius $\Delta R = 0.3$ is used. The inner, hollow part of the cone is called the veto cone. It is designed to remove the muon's own deposits from the calculation of the isolation. In the tracker the isolation cone is centered around the direction of the muon track at the interaction point, in the calorimeters the isolation cone is centered around the point where the muon hits the calorimeters. The isolation deposits in the

tracker is the scalar sum of the transverse momenta of the tracks in the hollow cone. The tracks should have small impact parameter with respect to the beam spot in the $x-y$ plane ($d_{xy}(bs)$) and they also should have their point-of-closest-approach (PCA) to the beam spot in close proximity to the muon's PCA in the z-direction ($|z^{track}_{PCA} - z^{muon}_{PCA}|$), as shown in table 5.7. Note that muon's own track is removed from the calculation of deposits by the veto cone. In all calorimeters the isolation deposits are the sum of the transverse energy of all calotowers in the hollow cone except for the towers with the energy below the 3σ of the energy of the noise and with transverse energy E_T below the respective thresholds. The cuts on the pre-selected tracks in the tracker, the thresholds on the calotowers in the calorimeters, and the sizes of the veto cones are summarized in table 5.7.

Tracker			ECAL barrel	ECAL end-cap	HCAL and HO
$d_{xy}(bs)$	$< 1\ mm$	E (GeV)	> 0.12	> 0.45	> 0.6
$\|z^{track}_{PCA} - z^{muon}_{PCA}\|$	$< 2\ mm$	E_T (GeV)	> 0.2	> 0.2	> 0.5
veto cone radius	0.01		0.07	0.07	0.1

Table 5.7: The sizes of the veto cones in each detector, the selection cuts on the tracks, and the calotower thresholds for calculation of the muon isolation deposits in the tracker and in the calorimeters.

In this analysis we have used a combined relative isolation variable, which is the sum the isolation deposits in the tracker and in the both calorimeters divided by the value of the transverse momentum of the muon,

$$iso_{CombRel} = \frac{iso_E + iso_H + iso_T}{p_T} \ , \tag{5.5}$$

to determine the degree of muon's isolation, see figure 5.9.

The summary of all the variable's we have used to identify prompt isolated muon in this analysis along with their cuts is given in table 5.8

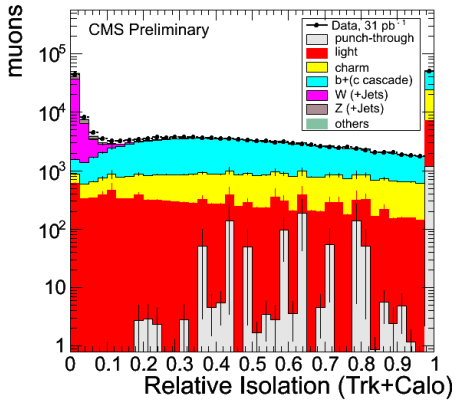

Figure 5.9: The combined relative isolation distribution, taken from [4].

tracker track	
$N_{hits}^{tracker}$	> 10
$d_{xy}(bs)$	$< 200\ \mu m$
$d_z(pv)$	$< 1\ cm$
global muon track	
$\chi^2/ndof$	< 10
N_{hits}^{muon}	> 0
muon object	
Global muon?	yes
Tracker muon?	yes
$\frac{iso_E + iso_H + iso_T}{p_T}$	< 0.15

Table 5.8: The cuts on the variables for the identification of prompt isolated muons. For the definition of each variable, please refer to the text.

5.5 Particle flow algorithm.

The particle flow algorithm [6] attempts to reconstruct all stable strongly or electromagnetically interacting particles in the event, that is, electrons, photon, muons, and all charged and neutral hadrons, using information from all of the CMS sub-detectors. The resulting particles are then used to reconstruct higher level observables, such as jets, missing transverse energy, isolated electrons and muons, etc. In this analysis we use the particle flow framework to reconstruct jets and missing transverse energy.

5.5.1 Particle flow jet reconstruction.

Jets are associated with hadrons. The process of the hadronization (formation of hadrons out of quarks and gluons) results usually in a bunch of particles, which are, due to the boost from the initial parton, emanating from the interaction point in a tight cone. As was mentioned in section 2.1, hadrons originating from heavy-flavor quarks can decay emitting a lepton, that is sometimes isolated from the jet of hadrons in a jet. In other cases the hadron itself can be confused with electron by depositing all of its energy in the electromagnetic calorimeter or with muon by punching through the calorimeter and the magnet and leaving a track segment in the muon chambers. Leptons originating from hadrons are called "fake leptons" or "background leptons" as they are not part of the signal. For this analysis it is important to understand their rate and how their rate depends on the properties of the jets in the event. For that reason we need to reconstruct the parameters of the jets.

In particle flow framework the jets are defined as groups of any reconstructed particles which have been clustered (their four-momentums combined to yield the jet's four-momentum) according to some clustering algorithm. In this analysis we

used jets clustered by anti-k$_T$ algorithm [5], which is fast, infrared safe[1] and collinear safe[2] jet clustering algorithm. The criteria for clustering particles into a jet are the following:

$$d_{ij} = min(k_{ti}^{2p}\ ,\ k_{ti}^{2p})\frac{\Delta_{ij}^2}{R^2} \tag{5.6}$$

$$d_i = k_{ti}^{2p} \tag{5.7}$$

where $\Delta_{ij}^2 = (\eta_i - \eta_j)^2 + (\phi_i - \phi_j)^2$ and k_{ti}, η_i, and ϕ_i are correspondently transverse momentum, pseudo-rapidity , and azimuthal angle of the particle i. R is radius of the jet. The algorithm loops over all entities (particles, clusters of particles) and compares d_{ij} and d_i, if d_{ij} is smaller the i and j are clustered if d_i is smaller than it is called a jet and removed from the list. The traditional k_t algorithm has $p = 1$, thus the anti-k_t algorithm has $p = -1$. It is easy to demonstrate that with anti-k_t condition the clustering algorithm prefers to cluster around hard particles, thus forming nice conical jets with a hard particle center, while the jets of the soft particles in the neighborhood of the hard particles will have deformed cones, see figure 5.10.

The anti-k_t jet clustering algorithm with the jet cone size $R = 0.5$ is the default jet clustering algorithm in CMS. Thus it was used in this analysis within a particle flow framework. Except for applying threshold on jet transverse momentum and assuring that a jet was not coinciding with one of the selected leptons no additional jet identification variables were used in this analysis.

---

[1]Infrared safe jet algorithm means that the output of the algorithm is stable against addition of soft particles.

[2]Collinear safe jet algorithm means that the output of the algorithm remains the same if the energy of the a particle distributed between two collinear particles.

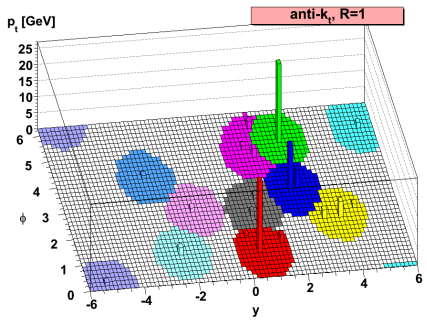

Figure 5.10: Example of the anti-k_t clustering algorithm at work, the cones (circles in this projection) around the hard particles are nice and round, while the cones of the soft particles, in close proximity the cones of the hard particles, are deformed. For more detail see [5].

5.5.2 Particle flow missing energy reconstruction.

As we saw in chapter 3, many multi-leptonic SUSY signatures have either neutrinos or other weakly interacting particles in the final state. Such particles do not register by the detector but create an energy imbalance which can be measured. However, since the longitudinal momentum of the individual colliding partons is not known (just the longitudinal momentum of the whole proton can be measured) and only the transverse momentum of the colliding partons can be assumed with a large precision to be zero. Thus we only measure the transverse part of the energy imbalance, which we call the missing transverse energy.

Since the particle flow algorithm reconstructs all particles, the reconstruction of the missing transverse energy proceeds in a straightforward fashion. The $\not\!\!E_T$ is the vector balancing the vector sum of the transverse momenta of all particles.

One potential problem that can affect the particle flow reconstruction of missing transverse energy is calorimeter noise. The noise towers and crystals can be reconstructed as neutral hadrons and photons and included into the calculation of the missing transverse energy. Therefore a simple cleaning algorithm was developed and tuned to identify the noise patterns even if they are in the neighborhood

of the real signal, to mask noisy channels so that they are not used in the particle flow reconstruction while insuring that none of the real signal was suppressed. The distribution of the missing transverse energy after cleaning is shown on figure 5.11.

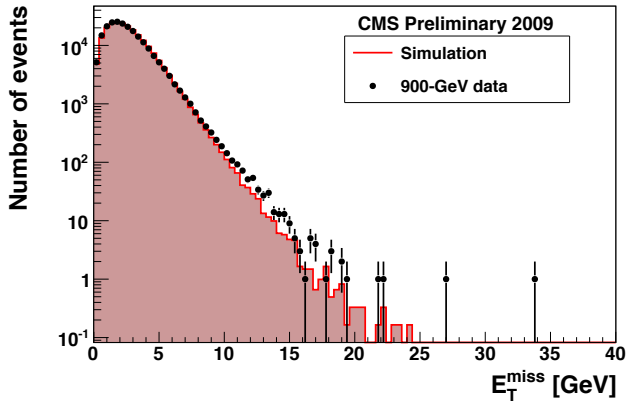

Figure 5.11: Particle flow missing transverse energy distribution after cleaning in $p-p$ collision with $\sqrt{s} = 900\ GeV$ compared with the simulation. For more detail see [6].

Together with cleaning applied the particle flow missing transverse energy exhibited better resolution when compared to the missing transverse energy calculated using only calorimeter information. Thus it was used in our analysis.

Chapter 6
Analysis

6.1 Analysis overview

This analysis, in its essence, is a counting experiment. We count the number of multi-lepton events in data and compare that number with the number of multi-lepton events predicted under the assumptions of the Standard Model theory, further on referred to as background events or simply background. The difference and the degree of difference between the number of events counted in data and the number of predicted background events tell us whether new physics has been discovered and also tells us the probability of its existence.

A strong point of this analysis is the way in which the counting is done. We use an exclusive multi-channel approach, where each channel is assigned a priority based roughly on the anticipated ratio of the number of signal to background events in it. The selected events are then categorized into multiple channels, where a selected event can belong to one and only one channel with the highest priority for which it can qualify for. Each channel is then treated as a separate experiment for which the background is estimated. The channels are then combined to perform simultaneous multi-channel fit.

The exclusive channels are categorized according to the following criteria: The number of isolated leptons in the event, the flavor of the isolated leptons, the value of the missing E_T in the event, the invariant mass of the opposite-sign-same-flavor

leptons, and the value of the total charge of the leptons. Such categorization simplifies estimation of the background, for example the background for electrons differs from the background for muons and is better estimated separately, and allows us more flexibility to prioritize the channels according to signal-to-background ratio, the higher signal-to-background ratio gets higher priority, ultimately giving higher statistical power to the analysis. The categorization also allows us to not discard the channels with the large number of background events, but to assign them a lower priority and use them to check our background predictions. The multi-channel method is described in detail in section 6.2.4.

Another strong point of this analysis is the data-driven methods for estimating "fake" multi-lepton background. Such background is usually difficult to estimate from a simulation. The imperfect theoretical description of the QCD processes prevents us from making an accurate estimate of the rate with which a jet "fakes" an isolated lepton or track. These methods are described in detail in section 6.4.1.

In the following sections I describe in detail the event selection process, the requirements we put on the objects which we consider for the analysis, the method with which we classify our exclusive channels, the methods we use to estimate the background, and the statistical procedure we use to perform the multi-channel fit.

6.2 Event selection.

Event selection in this analysis is a multi-step process. First, as described section 4.4, the events are pre-selected by the triggers and categorized into corresponding datasets according to the type of the trigger paths they have passed. Then, as described in chapter 5, the events are reconstructed by the offline reconstruction software. At this point we analyze the recorded datasets, apply our pre-selection

criteria in order to further slim down the data sample (see section 6.2.2), and form our n-tuples[1]. The n-tuples are used for the final event selection and analysis.

6.2.1 Triggers.

Since the event selection process starts with the triggers, it is important to decide, which triggers to use for our analysis. For our signal we select events, which came either on muon or on electron triggers. For studying background events and fake rate prediction (see section 6.4) , we select events, which came either on jet or on missing E_T triggers.

However, the set of triggers during the year 2010 period of data collection did not stay the same for several diverse reasons. First, as mentioned in section 4.1, the instantaneous luminosity, delivered by the LHC, has increased by five orders of magnitude during that period. Second, our understanding of the detector has improved. We learned more about the noise patterns, and the new noise backgrounds, such as electromagnetic calorimeter spikes mentioned in section 4.2.2, were discovered and understood. The efficiencies of the sub-systems have been better measured.

Thus, to deal with increasing event rate and to improve our precision in selecting the signal events, by using our better understanding of the detector, the trigger algorithms have changed and new algorithms were introduced in the course of that year. For example, the p_T threshold on the un-prescaled single muon trigger was raised from 7 GeV in the beginning of the data-taking period to 12 GeV close to the end. The new triggers, with improved electron identification algorithm that took into account the "spike" noise background, were introduced.

[1]n-tuples in our case mean files containing information about the events, such as the list of particles in the event, their kinematic information, trigger information, and any other information about the event we think is relevant for analyzing the data. This information is organized by the event.

In order to manage the above-described complexity of triggers in our analysis we required that each event was triggered either un-prescaled single muon triggers or un-prescaled single electron triggers. In addition, to avoid addressing trigger turn-on effect we required that the events that came on muon triggers had at least one reconstructed muon with $p_T > 15\ GeV$ and the events that came on electron triggers had at least one reconstructed electron with $p_T > 20\ GeV$, which was higher the p_T thresholds of correspondently single muon and electron triggers. You can find the full list of the datasets, triggers, and the periods of their validity in Appendices A and B.

6.2.2 Event screening criteria.

After events have been initially captured by the triggers and classified in their respective datasets, we skim over them and select the proton-proton collision events, while rejecting the events that were originated by other processes. Such as, the proton collisions with the residual gas in the beam pipe, so called beam-gas events, or the events triggered by the muons, penetrating the detector from the outside, that were produced in atmospheric interactions of highly relativistic charged particles (mostly protons) that came from outer space. In order to accomplish this selection, we require each event to have the following properties:

Each event should have at least one primary vertex which has at least 4 degrees of freedom and is located within the cylinder, $|z| < 24\ cm$ and $r < 2\ cm$.

Additionally, if the event has more than 10 tracks, then at least 20% of them should be of "high purity" type.

6.2.3 Lepton Selection.

In order to classify the events, we select and count the positively identified prompt isolated leptons according to the identification criteria detailed in sections 5.3

and 5.4, separating them from all the reconstructed leptons in the event. The order in which we pick the leptons is in inverse relation to their probability of misidentification. First, we select isolated muons, because they are less likely to be misidentified. Then, we select isolated electrons making sure that they do not overlap in with already selected muons, which means they should have the same azimuthal angle and the same pseudo-rapidity. Finally, we select isolated tracks, we determine the isolation of tracks in the same way we determine the isolation of muons, see 5.4. The tracks act as a proxy for isolated single prong taus, which are the taus that decayed into a single pion or kaon and a neutrino, see section 2.1.2. Again, we make sure that none of the tracks overlap with either previously selected muons or previously selected electrons.

Muon selection criteria.

As was discussed in section 5.4, muons are less likely to be misidentified, thus we start our lepton selection with them. We select prompt isolated muons that were identified according to the criteria in table 5.8 and, which are also passed the cuts on the transverse momentum and pseudo-rapidity, as listed in the table 6.1.

Muons	
variable	cut
p_T	$> 8\ GeV$
$\|\eta\|$	< 2.1

Table 6.1: Additional muon selection cuts on the transverse momentum and pseudo-rapidity.

Note that although muon system extends in pseudo-rapidity up to $|\eta| = 2.4$, we impose tighter cut on pseudo-rapidity to insure proper determination of the isolation of the muon, since the isolation cone has radius $R = 0.3$.

Electron selection criteria.

Electrons come up second on our list of the less likely to be misidentified leptons. Thus, we select them after we have already selected muons. To select prompt isolated electrons, we apply identification cuts in listed table 5.4, followed by the cuts that reject electrons, which have originated from converted photons (see table 5.5), and the isolation cuts listed in table 5.6. In addition, we require that electrons pass the transverse momentum, pseudo-rapidity cuts, and that their direction should be far enough from already selected muons, see table 6.2. Note

Electrons	
variable	cut
p_T	$> 8\ GeV$
$\|\eta\|$	< 2.1
ΔR(nearest muon)	> 0.1

Table 6.2: Additional electron selection cuts on the transverse momentum, pseudo-rapidity, and distance between electron candidate and the nearest selected muon.

that again, we chose pseudo-rapidity range 0.3 η units less, than the full pseudo-rapidity coverage for electrons, to insure the correct calculation of their isolation.

Tau selection criteria.

As was discussed in section 2.1.2, tau leptons have very short life time ($c\tau = 87.11\ \mu m$), therefore they decay within a few microns from the interaction point. Large fraction of all tau decays, 35.2%, is leptonic, either $\mu^- \bar{\nu}_\mu \nu_\tau$ or $e^- \bar{\nu}_e \nu_\tau$. Since neutrinos in leptonic tau decay escape undetected, the only particles we observe are either prompt and isolated muon or prompt and isolated electron. In order to select them, we apply the same identification cuts we use for identifying electrons and muons. In other words, a fraction of the electrons and muons that we are selecting as described above are taus, which have decayed leptonically.

The remaining tau decay modes are hadronic, see table 2.4. In the beginning of the data collection several distinct algorithms were employed within CMS to identify and reconstruct the hadronically decaying tau leptons, such as: the Tau Neural Classifier (TaNC) algorithm, the Hadron plus Strips (HPS) algorithm, the Track Corrected Tau (TCTau) algorithm, and the shrinking cone tau algorithm based on the particle flow method [24]. However, at the time of this analysis all these algorithms were in the testing stage and the measurements of the efficiencies and fake rates were available only for simulated data. For that reason, in this analysis we use isolated tracks to select hadronic single-prong isolated tau decays, that is $\tau \to \pi\nu_\tau$ and $\tau \to K\nu_\tau$. These decays account for 11.6% of all tau decays. The usage of the isolated track is simple and allows us to estimate the efficiencies and the fake rates from the collision data, using the same methods as we use for muons and electrons (see section 6.4.1). The selection criteria for the isolated tracks are listed in the table 6.3. Note that the combined relative isolation is calculated in the same way as it is done for muons, see equation 5.5.

Taus	
Vairable	cut
Number of Valid Hits	> 10
$\lvert d_z(pv)\rvert$	$< 1\ cm$
$\lvert d_{xy}(bs)\rvert$	$< 200\ \mu m$
$(iso_E + iso_H + iso_T)/p_T$	< 0.15
$p_T >$	$8\ GeV$
$\lvert\eta\rvert$	< 2.1
ΔR(nearest electron or muon)	> 0.1

Table 6.3: Identification cuts for selecting hadronic single-prong isolated tau decays. All cuts are applied any CTF track in the general track collection (see section 5.2).

Note that again we limit our region of the pseudo-rapidity to $|\eta| < 2.1$, in order to insure correct evaluation of the track's isolation.

Missing E_T criteria.

As we saw in chapter 3, missing transverse energy accompanies many multi-lepton signatures. It is originating either from the neutrinos generated in the cascade decays of the supersymmetric particles or from the neutral lightest supersymmetric particle, which escapes the detector without interacting. Thus, we expect signal to background ratio to be different for multi-lepton events with small and with large values of the missing transverse energy. To account for that, each of our channels is divided into two sub-channels one with low missing transverse energy ($\not\!\!E_T < 50\ GeV$) and with one high missing transverse energy ($\not\!\!E_T > 50\ GeV$).

In section 5.5.2, we saw that missing transverse energy reconstructed in the particle flow algorithm is cleaned by default from the signals that can be misidentified as missing transverse energy. Thus, we do not apply any additional identification cuts and use the value of missing E_T as it comes out from particle flow reconstruction algorithm.

Jet selection criteria.

When selecting signal events, we do not take jets into account. However, as was shown in section 5.5.1, jets are the primary source of "fake" isolated leptons. Besides, they are also the primary source of "fake" isolated tracks, produced by charged pions and kaons. Thus, we use jets to estimate the fake rates for the tracks and for the leptons by using the fake rate method described in section 6.4.1. For that purpose we apply the criteria listed in table 6.4 to select jets.

Jets	
Vairable	cut
$p_T >$	$20\ GeV$
$\|\eta\|$	< 2.4
ΔR(nearest electron, muon, or track)	> 0.1

Table 6.4: Cuts applied to select jets for use in fake rate analysis.

6.2.4 Channels

Once our objects are selected and disambiguated by using ΔR cut (see tables 6.2 and 6.3) to make sure that electrons are not also identified as muons, and that tracks are not also identifed as either muons or electrons. We then analyze the event: We count the total number of muons (N_μ), the total number of electrons (N_{elec}), the total number of tracks (N_{track}), then add these number together to get the total number of all leptons ($N_l = N_\mu + N_{elec} + N_{track}$), and then determine the total charge of all leptons ($|Q_l|$) in the event. We also determine the amount of missing transverse energy in the event (missing E_T), and, for the muons and electrons, we calculate the invariant mass of the opposite-sign-same-flavor pairs (m_{ll}^{OSSF}).

Next, the events are categorized into exclusive channels according the values of the parameters determined above and the cuts on these values listed in table 6.5. The channels are then organized in precedence roughly according to signal to background ratio. This categorization results in 167 exclusive channels. All the channels, in the order of their priorities, are listed in Appendix C.

6.3 Lepton Efficiencies.

In order to compare the number of events we obtain from data with the number of events we obtain from theory, we need to know the efficiency of the method for selecting our events. In our case, we need to know the efficiency of the reconstruction and identification of the leptons and tracks. More precisely, since we already have a model for that efficiency, which is incorporated into our simulations, we need to compare the efficiency we obtain from the simulations with the efficiency we obtain from the data.

To obtain the efficiency of the reconstruction and identification of the leptons, we use tag and probe method. In this method we use a sample of prompt isolated

Channel	
Vairable	Allowed values
N_l	> 4
	4
	3
N_μ, N_{elec}	> 4
	4
	3
	2
	1
	0
N_{track}	2
	1
	0
$\|Q_l\|$	> 2
	2
	1
	0
missing E_T	$> 50\ GeV$
	$< 50\ GeV$
m_{ll}^{OSSF}	$[20,\ 75]$ and $[105,\ max]\ GeV$
	$[75, 105]\ GeV$

Table 6.5: Characterization criteria for exclusive channels: The number of leptons (N_l), number of each lepton flavor (N_μ, N_{elec}, N_{track}), absolute value of total charge of leptons in a channels ($|Q_l|$) the amount of missing transverse energy (missing E_T), and invariant mass of the opposite sign same flavor leptons (m_{ll}^{OSSF}). Note that $N_l = N_\mu + N_{elec} + N_{track}$.

leptons, which have originated from Z boson. We select one lepton requiring that it passes the strict criteria we use for selection of our signal leptons. We call this first lepton a tag. Then we look for another lepton that passes much weaker criteria, but, if its four-momentum is combined with the four-momentum of the tag lepton, the invariant mass of the combination is equal to the invariant mass of the Z boson. We call this second lepton a probe. We then check, if the probe lepton passes the same strict criteria as a tag lepton. We count the number of passing (N_{pass}^{probe}) and failing (N_{fail}^{probe}) probes and obtain the efficiency by using the following formula:

$$\epsilon = \frac{N_{pass}^{probe}}{N_{pass}^{probe} + N_{fail}^{probe}} = \frac{N_{pass}^{probe}}{N_{all}^{probe}} \tag{6.1}$$

For an electron, the probe criteria are listed in table 6.6. The values of these cuts are double those that select electrons with 95% efficiency, as measured in simulations. Moreover, no requirements either on isolation, or on rejection of converted photons is made. Thus, the probe electron selected by these criteria should have very high efficiency.

Electron probe		
Variable	barrel	end-cap
Had/Em	< 0.30	< 0.14
$\lvert\sigma_{I\eta I\eta}\rvert$	< 0.02	< 0.06
$\lvert\Delta\phi_{in}\rvert$	< 1.6	< 1.4
$\lvert\Delta\eta_{in}\rvert$	< 0.014	< 0.02

Table 6.6: Loose electron ID cuts for selecting probes.

The selection criteria for the tag electron are our regular selection criteria, which are listed in tables 5.4, 5.5, and 5.6. As mentioned above these requirements are also used to define a passing probe. For the tag electrons we have the same pseudo-rapidity cut but a stronger transverse momentum cut, $p_T > 20\ GeV$, in comparison to the cuts listed in the table 6.2.

The only criteria we impose on the probe muon, in addition to the transverse momentum and pseudo-rapidity criteria listed in table 6.1, is for it to be a global muon. As for the tag muon, in addition to our regular selection the criteria listed in tables 5.8 and 6.1, we impose a stronger transverse momentum cut, $p_T > 20\ GeV$.

The example of the invariant mass distribution of all probe and tag muon and electron pairs is shown on figure 6.1. The transverse momentum of the probe is in the range from 12 GeV to 24 GeV. In these plots, the invariant mass distribution for the simulated events is normalized to the area under the Z boson peak, 80 GeV to 100 GeV, in data.

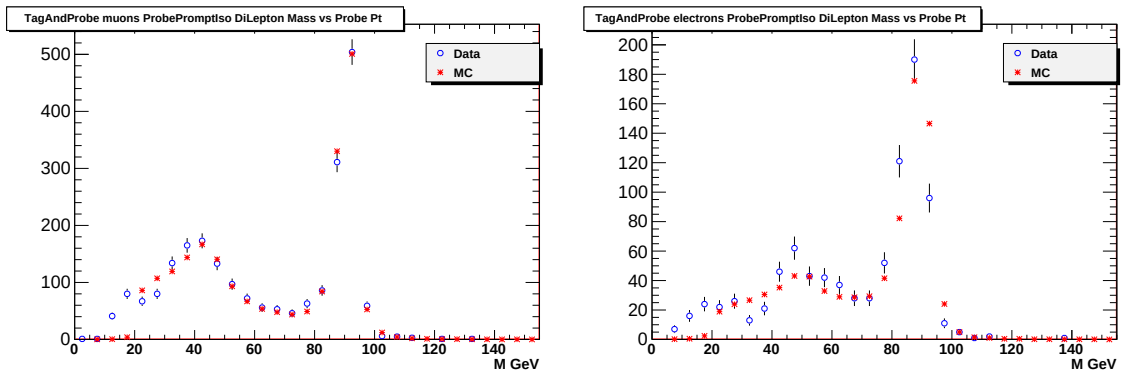

(a) (b)

Figure 6.1: The invariant mass of all tag and probe (a) muon and (b) electron pairs, with the p_T of the probe lepton in the range from 12 GeV to 24 GeV. The simulated events are shown by the red asterisks, while the data are shown by the blue circles.

We determine the number of all probes (N_{all}^{probe}) and the number of passing probes (N_{pass}^{probe}) by counting the number of events under the Z boson peak, 80 GeV to 100 GeV, before and after applying the passing probe criteria. In order to make sure that we count only the probe leptons thats have originated from the decay of the Z boson, we remove the background events under the Z boson peak, by fitting the side bands of the invariant mass distribution, 55 $GeV < m_{ll} < 75\ GeV$ and 105 $GeV < m_{ll} < 125\ GeV$, with a straight line. The amount of events under

the fit in the range from 80 GeV to 100 GeV is then subtracted from the total number of events under the peak as determined above.

The efficiency was calculated as a function of transverse momentum for two pseudo-rapidity ranges, barrel $|\eta| < 1.5$ and end-cap $1.5 < |\eta| < 2.1$. The efficiency was also calculated before and after applying the isolation criteria listed in tables 5.6 and 5.8 for electron and muon respectively, see figures 6.2 (a)-(h).

We find that lepton identification efficiencies agree to within a few percent over the whole range of the transverse momentum and for both ranges of pseudo-rapidity. Thus we calculate the average over the whole range of the transverse momentum of the ratios between identification efficiencies for muon and for electron, see table 6.7.

Identification efficiency		
η range	Muon	Electron
$\|\eta\| < 2.1$	1.008 ± 0.0009	0.983 ± 0.0026
$\|\eta\| < 1.5$	1.0062 ± 0.0009	0.9796 ± 0.0028
$1.5 < \|\eta\| < 2.1$	1.0142 ± 0.0021	0.9963 ± 0.0071

Table 6.7: Average ratios between the identification efficiencies in data and in simulations for muons and electrons for two pseudo-rapidity ranges.

While for the isolation efficiencies we find the the ratio of the isolation efficiencies between the data and the simulations is flat from $p_T = 20\ GeV$ and higher, but bellow 20 GeV the isolation efficiency in data is less and linearly declining, see figure 6.3. To model it we perform piecewise linear fit by the following function,

$$f(p_T) = \begin{cases} m \times (p_T - 20\ GeV) & \text{if } p_T < 20\ GeV \\ b & \text{if } p_T > 20\ GeV \end{cases} \tag{6.2}$$

where b and m are the fitting parameters. Their values for the muon and electron isolation efficiency ratios are listed in table 6.8.

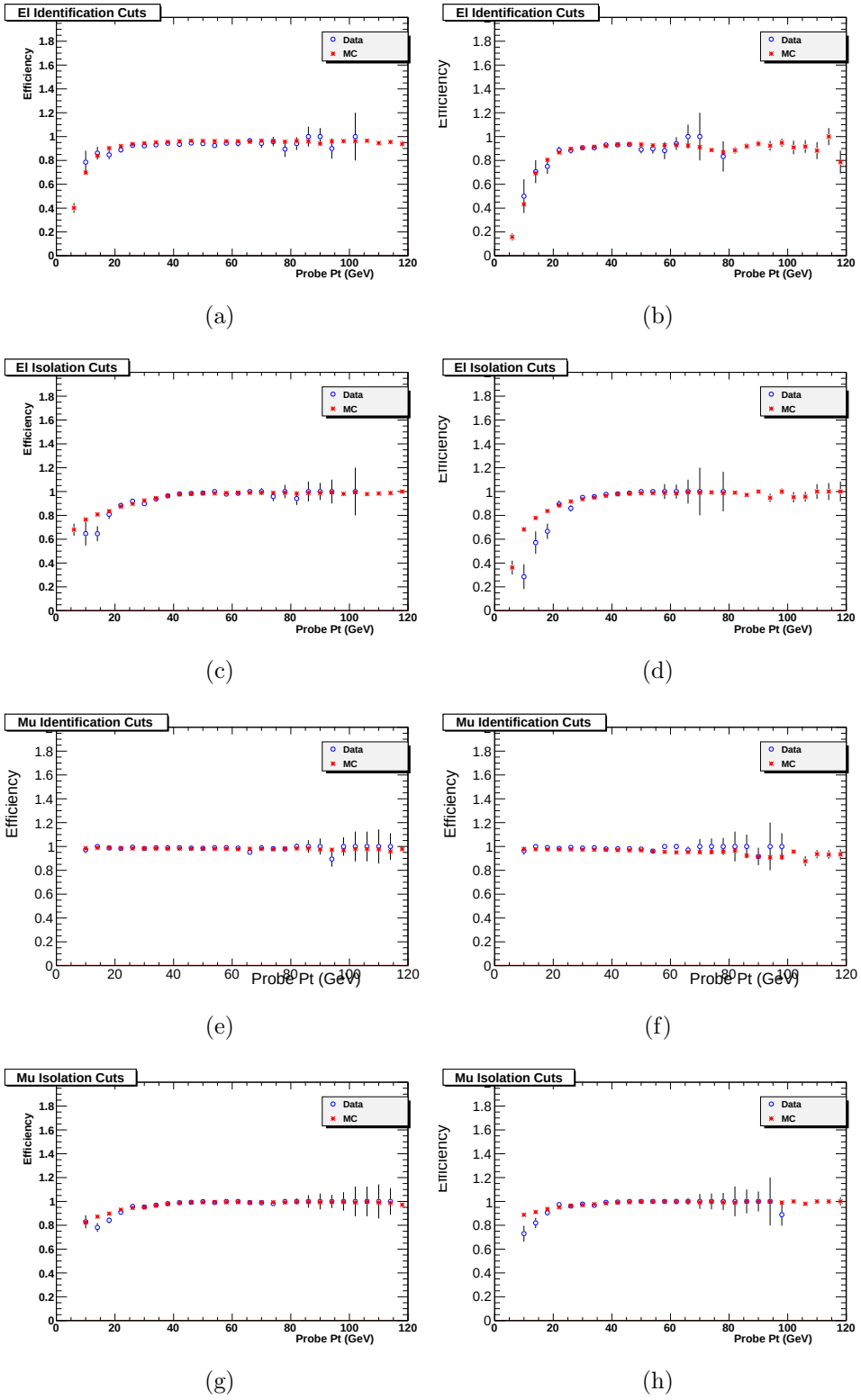

Figure 6.2: The (a)-(b) identification and (c)-(d) isolation efficiency for electrons and the (e)-(f) identification and (g)-(h) isolation muons. Plots for the barrel $|\eta| < 1.5$ are on the left, while plots for the end-cap $1.5 < |\eta| < 2.1$ are on the right. The simulated events are shown by the red asterisks, while the data are shown by the blue circles.

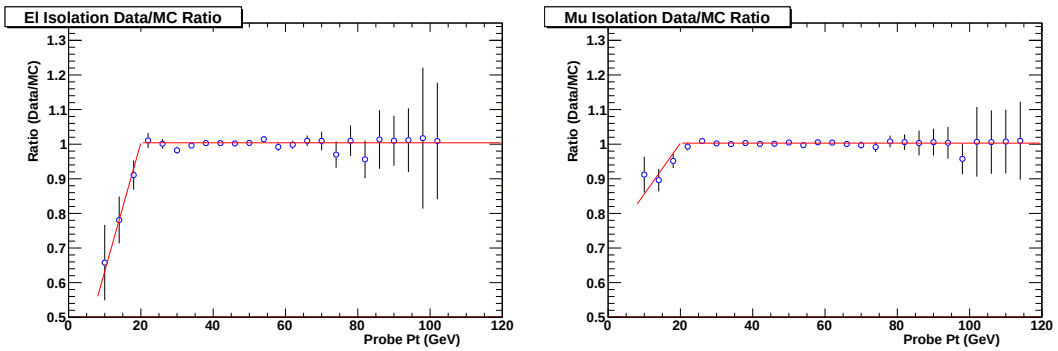

(a) (b)

Figure 6.3: The ratio between the isolation efficiencies in data and in simulations for (a) electrons and for (b) muons. The simulated events are shown by the red asterisks, while the data are shown by the blue circles.

	Isolation efficiency			
η range	Muon		Electron	
	b	m	b	m
$\|\eta\| < 2.1$	1.003 ± 0.0003	0.0147 ± 0.0035	1.004 ± 0.0015	0.0371 ± 0.0073
$\|\eta\| < 1.5$	1.0028 ± 0.0008	0.0107 ± 0.0046	1.0033 ± 0.0017	0.0239 ± 0.0086
$1.5 < \|\eta\| < 2.1$	1.005 ± 0.0013	0.0181 ± 0.005	1.0069 ± 0.0041	0.0586 ± 0.0115

Table 6.8: Parameters of the fit to the average ratios between the isolation efficiencies in data and in simulations for muons and electrons for two pseudo-rapidity ranges.

6.3.1 Lepton trigger efficiencies.

Before lepton can be identified it has to be recorded by the trigger. Similar to lepton identification described above, lepton trigger is not fully efficient. However, unlike the efficiency of the identification, we do not account for the trigger efficiency in our simulations. Thus, we cannot use the ratio of the trigger efficiencies between the data and the simulations and we have to determine the trigger efficiency itself.

To determine the trigger efficiency we count events, N_{met}, which were recorded on missing E_T trigger and have at least one lepton identified according to our identification criteria listed in tables 5.4, 5.5, 5.6, and 6.2 for electrons and in tables 5.8 and 6.1 for muons. Out of those events, we count how many events were also triggered by any of our lepton triggers, N_{met}^{lepton}. Since we assume that missing E_T trigger is uncorrelated with the lepton triggers, the combined efficiency of the lepton triggers is then:

$$\epsilon_{lepton} = \frac{N_{met}^{lepton}}{N_{met}} \tag{6.3}$$

We compare the results for several sets of events, which were recorded on various missing E_T triggers with different thresholds. We find that the efficiency of the muon and electron triggers does not depend on the choice of the missing E_T trigger. The lepton trigger efficiencies for the combination of all our electron and for the combination of all our muon triggers as a function of transverse momentum are shown in figure 6.4. We also find that the combined efficiency of the muon triggers was constant over the whole dataset range, while the combined efficiency of the electron triggers was higher in the beginning of the data taking period. The results are summarized in table 6.9.

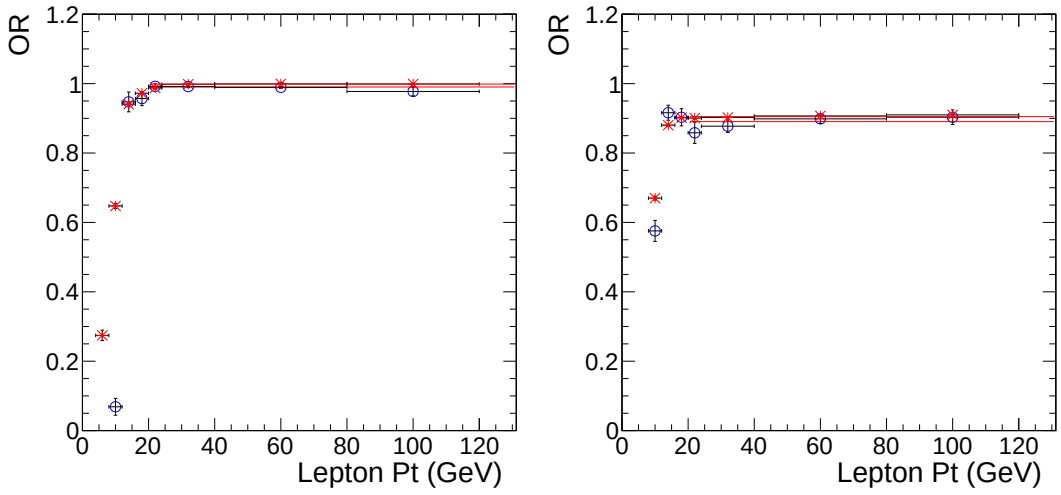

(a) (b)

Figure 6.4: The combined trigger efficiencies in data and in simulations for OR of all (a) electrons and (b) muons triggers. These efficiencies were measured for events which were recorded by the missing E_T trigger with threshold 45 GeV. The simulated events are shown by the red asterisks, while the data are shown by the blue circles.

	Trigger efficiency		
missing E_T threshold	Run range	Electron triggers	Muon triggers
45 GeV	< 148031	$99.0\% \pm 0.2\%$	$89.1\% \pm 0.9\%$
65 GeV	< 147116	$99.0\% \pm 0.8\%$	$89.9\% \pm 1.4\%$
80 GeV	$147196 - 148058$	$96.2\% \pm 1.5\%$	$88.8\% \pm 1.5\%$
100 GeV	$148822 - 149294$	$96.0\% \pm 3.3\%$	$91.7\% \pm 2.3\%$
120 GeV	$148822 - 149294$	$95.9\% \pm 5.3\%$	$91.1\% \pm 3.6\%$

Table 6.9: Trigger efficiencies for combined electrons and muon triggers measured on events recorded on missing E_T triggers with various thresholds.

6.4 Background Estimation

The main advantage of the multi-lepton signatures is that they have a very low number of Standard Model background events. Few Standard Model processes produce three or more prompt isolated leptons. The most prominent examples are: the ZZ, where both Z bosons decay leptonically thus giving a signature of four leptons and no missing transverse energy, since there are no neutrinos in the final state. The WZ, where both W and Z bosons decay leptonically, thus giving a signature of three real leptons and missing transverse energy, because of the neutrino in decay of the W. The cross-section of those two processes is very small, therefore they did not produce many multi-lepton signatures in the current LHC data (see table 6.13).

However, there are plenty of processes in which one or two prompt isolated leptons are accompanied by jets, where one or more of the jets "fake" an isolated lepton, therefore resembling a multi-lepton event. Here are the most prominent examples of these processes are: W+jets, Z+jets, and $t\bar{t}$+jets.

"Fake" background source			
Process	final state	$\sigma_{NNLO} \times B.R.$ (pb)	N_{events}
$W + N$ jets	$\rightarrow \ell\,\nu + N$ jets	31314	1.1×10^6
$Z + N$ jets	$\rightarrow \ell\,\ell + N$ jets	4998	1.7×10^5
$t\bar{t} + N$ jets	$\rightarrow \ell\,\nu_l\,q\,q\,b\,\bar{b} + N$ jets	73	2.6×10^3
	$\rightarrow \ell\,\ell'\,\nu_l\,\nu_{l'}\,b\,\bar{b} + N$ jets	18	6.4×10^2

Table 6.10: Main sources of "fake" multi-lepton background events, their decay modes, their cross-sections multiplied by the branching ratios ($\sigma_{NNLO} \times B.R.$) and total number of events expected in 35 pb^{-1} of data collected in 2010. Note that N is zero or more.

In the data samples with large amount of events that also contain background for our channels, such as di-leptonic sample originating from $Z + N$ jets decays,

we use data to derive the background estimates. In all other data samples we use Monte-Carlo simulations to estimate background contained in them.

In the following I will first describe our data-driven methods of background estimation then I will describe the relevant details in our estimation of the background using Monte-Carlo simulations.

6.4.1 Data-driven background estimation.

Data-driven background estimation for leptons.

We estimate the rate with which jets "fake" leptons by using data. We do that by first measuring the ratio between the rate with which a jet is mis-identified as an isolated track and the rate with which it is mis-identified as an isolated lepton. We assume that this ratio depends on the transverse momentum of the jet, its pseudo-rapidity, and the flavor of the jet, which is the flavor of the primary parton that produced this jet.

In the first method, we assume that the jet production is controlled by similar strong interactions (also known as QCD processes) in the direct QCD production, where jets are produced directly as a result of hard collision, and in the di-lepton sample, where the QCD process accompanies the electroweak process that has produced the leptons. Thus, we can assume that the jet flavor content, or the ratio of the heavy flavor jets to the light flavor jets, is the same in both the QCD and di-lepton sample. Therefore, the ratio of the number of isolated tracks to the number of isolated leptons is also the same for the same pseudo-rapidity and transverse momentum ranges in both the QCD and di-lepton samples. Hence, we can take advantage of the fact that QCD processes are in abundance in proton-proton collider, calculate the conversion coefficients (see equations 6.4 and 6.5)

in the high statistic QCD sample, and then apply them to our di-lepton "seed" sample.

$$f_\mu = \frac{N_\mu^{iso}}{N_t^{iso}} \tag{6.4}$$

where N_μ^{iso} is the number of the isolated muons, N_t^{iso} is the number of isolated tracks.

$$f_e = \frac{N_e^{iso}}{N_t^{iso}} \tag{6.5}$$

where N_e^{iso} is the number of the isolated muons, N_t^{iso} is the number of isolated tracks.

In the 2010 LHC data, with a total integrated luminosity 35 pb^{-1}, the number of fake multi-lepton events is small, hence we ignore the p_T and η dependence of the conversion coefficients and calculate their average values for the single p_T and η bin, 8 $GeV < p_T < 24$ GeV and $|\eta| < 2.1$. We stop at $p_T = 24$ GeV, because the transverse momentum distribution of leptons in the QCD sample dies out at this value.

In the second of our data-driven methods, we evaluate the dependence of the conversion coefficients on the jet composition, that is the amount of heavy flavor jets in a jet sample. To do this we first re-write the formulae for the conversion coefficients, 6.5 and 6.4, as following, 6.7 and 6.6.

$$f_\mu = \frac{N_\mu}{N_t}\frac{\epsilon_\mu^{iso}}{\epsilon_t^{iso}} \tag{6.6}$$

where N_μ is the number of the non-isolated muons, N_t is the number of non-isolated tracks, ϵ_t^{iso} is an isolation efficiency of tracks, and ϵ_μ^{iso} is an isolation efficiency of muons.

$$f_e = \frac{N_e}{N_t}\frac{\epsilon_e^{iso}}{\epsilon_t^{iso}} \tag{6.7}$$

where N_e is the number of the non-isolated electrons, N_t is the number of non-isolated tracks, ϵ_t^{iso} is an isolation efficiency of tracks, and ϵ_e^{iso} is an isolation efficiency of electrons. We determine the first ratio in equations 6.7 and 6.6 of the number of the non-isolated leptons to the number of the non-isolated tracks in the di-lepton samples. While the second ratio, $\frac{\epsilon_l^{iso}}{\epsilon_t^{iso}}$, we determine in the QCD sample as a function of R_{dxy}. Where R_{dxy} is the ratio between the number of non-isolated tracks with the impact parameter $|d_{xy}| > 0.02\ cm$ and the number of non-isolated tracks with the impact parameter $|d_{xy}| < 0.02\ cm$, see equation 6.8.

$$R_{dxy} = \frac{N^{track}(|d_{xy}| > 0.02)}{N^{track}(|d_{xy}| < 0.02)} \tag{6.8}$$

Since the heavy flavor hadrons decay few hundred microns away from the interaction point, the tracks of the charged particles in the heavy flavor jet have impact parameter larger than the tracks in the light jet, which is formed in the primary interaction. Thus, this ratio is a measure of the heavy flavor content in jets, thus we are measuring the dependence of the ratio of isolation coefficients as a function of the heavy flavor content in jet. The dependance of the ratio of the isolation efficiencies for electrons and tracks on R_{dxy} and the dependance of the ratio of the isolation efficiencies for muons and tracks on R_{dxy} are very different as one can see from figures 6.5a and 6.5b.

Next, we determine the R_{dxy} in the di-lepton sample to which we apply the conversion coefficients. Because we expect the fraction of the heavy jets to be the

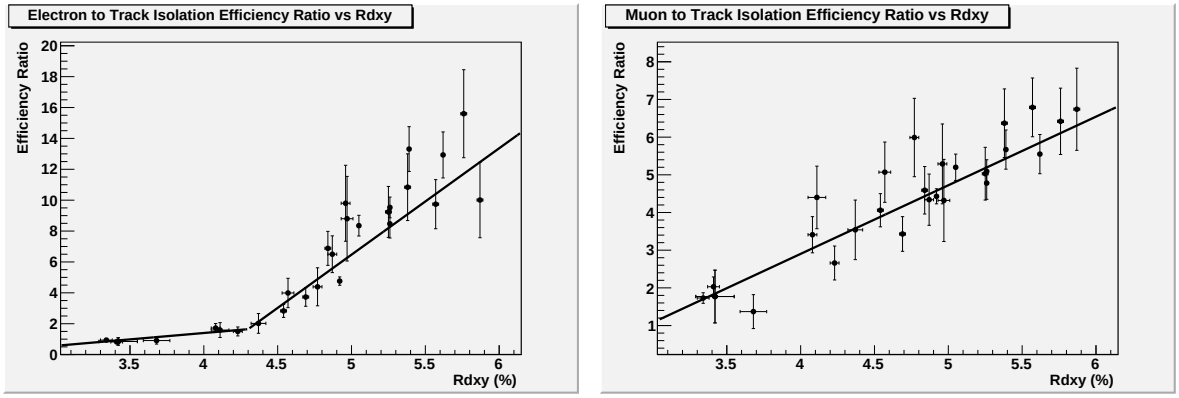

(a) electrons (b) muons

Figure 6.5: The ratio of isolation efficiencies of electrons to tracks (a) and the ratio of isolation efficiencies of muons to tracks (b) dependancies on the fraction of non-isolated tracks with a large impact parameter.

same in the di-muon and di-electron sample, hence the same value of R_{dxy}, we combine these samples to calculate R_{dxy}. We use thus determined value of R_{dxy} to find the ratio of isolation efficiencies from the corresponding graph in figure 6.5. Finally, we calculate the conversion coefficients,f_e and f_μ, for our di-lepton seed sample. The results are presented in the table 6.11.

The conversion coefficients which we determined with the first method were similar, thus both methods are applicable

After we have determined our conversion coefficients, we use them to determine the "fake" rate for the three and four lepton samples by applying the conversion coefficients to the di-lepton sample from which this background potentially originates, also known as a "seed" sample. For example, the potential contributor of background events to the sample with two isolated muons and one isolated electron ($\mu\mu e$) is the sample with two isolated muons ($\mu\mu$) in which the jet, accompanying muons, would "fake" a prompt isolated electron. Thus, in order to estimate the number of potentially "fake" electrons in $\mu\mu e$ sample, we

Conversion coefficients	
Parameter	Value
$\frac{N_e}{N_t}$	0.008 ± 0.001
$\frac{N_\mu}{N_t}$	0.007 ± 0.001
R_{dxy}	0.043 ± 0.003
$\frac{\epsilon_e^{iso}}{\epsilon_t^{iso}}$	$1.6^{+2.2}_{-0.3}$
$\frac{\epsilon_\mu^{iso}}{\epsilon_t^{iso}}$	3.3 ± 0.6
f_e	$0.0013^{+0.018}_{-0.003}$
f_μ	0.022 ± 0.006

Table 6.11: Summary of the conversion coefficients for di-electron and di-muon seed samples.

calculate the number of events with one isolated track in $\mu\mu$ sample ($N^{iso}_{\mu\mu t}$) then multiply it by the conversion coefficient for electrons (f_e) see equation 6.9.

$$N^{iso}_{\mu\mu e} = N^{iso}_{\mu\mu t} \times f_e \ , \tag{6.9}$$

where the $N^{iso}_{\mu\mu e}$ is the estimated number of fake background $\mu\mu e$ events, $N^{iso}_{\mu\mu t}$ is the number events with one isolated track in $\mu\mu$ sample, and f_e is a conversion coefficient for electrons.

For the four lepton sample we twice multiply the number of events in the di-lepton sample that have two isolated tracks (N^{iso}_{lltt}) by the appropriate conversion coefficients. For example, to determine the number of fakes in $eee\mu$ sample, we count the number of events with two isolated tracks (N^{iso}_{eett}) in ee sample and then

multiply that number by the conversion coefficients for muon and for electron, f_μ and f_e, see equation 6.10

$$N^{iso}_{eee\mu} = N^{iso}_{eett} \times f_e \times f_\mu \ , \tag{6.10}$$

where $N^{iso}_{eee\mu}$ is the estimated number of fake background $eee\mu$ events and N^{iso}_{eett} is the number of events with two isolated tracks in ee sample.

Fake rate for tracks.

In order to predict the background for isolated tracks, we use the isolation template method. In this method we divide the isolation distribution in three regions:

The isolated region, containing the tracks with the combined relative isolation (see equation 5.5) between 0.0 and 0.15.

The side band region, containing the tracks with the combined relative isolation between 0.2 and 1.0.

The non-isolated region, containing the tracks with the combined relative isolation > 1.0.

We define the conversion coefficient (f_T) as a ratio between the number of isolated tracks and the number of tracks in the side band region, as shown in the formula 6.11

$$f_T = \frac{N^{iso}_{track}}{N^{SB}_{track}} \tag{6.11}$$

And we define the side band coefficient (f_{SB}) as a ratio between the number of tracks in the side band region and the number of tracks in the non-isolated region, as shown in the formula 6.12.

$$f_{SB} = \frac{N^{SB}_{track}}{N^{non-iso}_{track}} \tag{6.12}$$

In this method we assume that, if two data-samples have the same coefficient f_{SB}, then they should have approximately the same coefficient f_T. Hence, to determine the number of isolated tracks in our di-lepton sample, we first find the f_T dependance on f_{SB} shown in figure 6.6. We determine this dependance by splitting the data into bins of the sum of the transverse momentum values of all tracks associated with the primary vertex and calculate both coefficients, f_T and f_{SB}, for each bin. To understand the systematic errors of our method, we measure this relation in two distinct datasets, one containing events that were recorded on jet triggers (Jet) and the other containing events that were recorded on missing E_T and forward triggers (MetFwd). The systematic error is then obtained from the difference between f_T versus f_{SB} dependancies for the two datasets.

From the f_T versus f_{SB} dependance we find the appropriate f_T for the f_{SB} that we measure in our di-lepton sample. Then, to find the expected number of isolated tracks, we count the number of tracks in the side band region of our di-lepton sample and multiply it by the f_T .

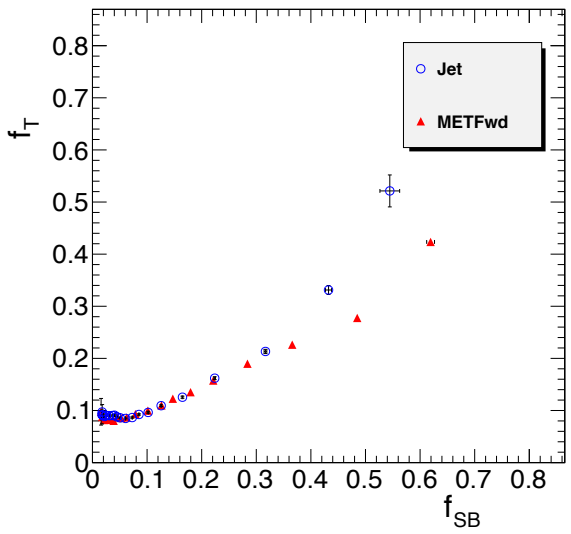

Figure 6.6: The dependance between the side band coefficient and isolation coefficient for MetFwd and the Jet datasets.

Since the f_T dependance on f_{SB} is non-linear, we divide the dependance into three bins and fit each bin with a separate linear function, $f_T = a \times f_{SB} + b$. The result of the fits is summarized in table 6.12. Since the two fits (one made using the Jet dataset, the other made using the MetFwd dataset) give different results, we choose the one that gives the largest f_T value, in order to overestimate the systematic error. We estimate the systematic error to be either the difference between the two f_T value or 20%, whichever is larger.

	0.0 – 0.1		0.1 – 0.3		0.3–1.0	
Trigger dataset	a	b	a	b	a	b
MetFwd	0.22	0.0745	0.49	0.049	0.747	-0.56
Jet	-0.047	0.0904	0.52	0.043	1.115	-0.141

Table 6.12: Coefficients of the linear fits of the f_T vs f_{SB} dependence for three bins of f_{SB} in Jet and MetFwd datasets.

6.4.2 Backgrounds estimation from Monte-Carlo.

Irreducible Multi-lepton background

The "real" multi-lepton background, produced by ZZ and WZ processes, is straightforward to estimate. The Standard Model theory describes them well, hence we rely on Monte-Carlo (MC) simulations for their estimation. However, the simulation of the detector response is not perfect, we observe small differences between the measured lepton efficiencies in the simulations and the measured lepton efficiencies in the data. Thus, we do apply small corrections based on the measured efficiency ratio for leptons between the simulations and the data. Finally, we scale the number of events in the MC sample to the luminosity we have in data using the Next-to-Leading-Order (NLO) cross-section in order to get the number of estimated background events. The results are summarized in the table 6.13

WZ and ZZ background			
Process	final state	$\sigma_{NNLO} \times B.R.$ (pb)	N_{events}
Z/γ^*-Z/γ^*	$\rightarrow \ell\,\ell\,\ell'\,\ell'$	0.059	2
W-Z/γ^*	$\rightarrow \ell\,\ell\,\ell'\,\nu$	0.6	21

Table 6.13: Main sources of "real" multi-lepton background events, their decay modes, their cross-sections multiplied by the branching ratios ($\sigma_{NNLO} \times B.R.$) and total number of events expected before accounting for detector acceptance, trigger and identification efficiencies in 35 pb^{-1} of data collected in 2010. The ℓ stands for all lepton flavors, e, μ, and τ. Not that the cross-sections are calculated for $m(Z/\gamma^*) > 40\ GeV$.

Background from di-lepton events with jets.

As we saw above, the $Z + jets \rightarrow l^+l^- + jets$ process gives the largest sample of di-lepton events accompanied by jets. This background is estimated using data-driven method described in section 6.4.1. However, there are other process that produce events with two leptons in the final state accompanied by jets, but for which due to smaller statistic, the data-driven background prediction is difficult. The most prominent of such processes is $t\bar{t} \rightarrow W^+W^-b\bar{b} \rightarrow l^+l^-\nu\bar{\nu}b\bar{b}$. In 35 pn^{-1} of integrated luminosity the amount of di-leptonic $t\bar{t}$ events is not large, see table 6.10, but due to the presence of two b-quarks in the final state, the prompt isolated lepton fake rate is naturally higher.

Background from bremsstrahlung.

In a two lepton event, one of the leptons, interacting with matter of the detector, can emit a hard photon that converts into two electrons. If one of the electrons is significantly harder, than the other, it will not be rejected by conversion rejection cuts listed table 5.5. Additionally, if the electron is isolated from the parent lepton, this event we will be interpreted as an event with three leptons in the final state. Even in relatively low integrated luminosity, 35 pb^{-1}, this process creates a substantial background to the eee and $\mu\mu e$ channels with low missing

E_T ($\not\!\!E_T < 50\ GeV$) and Z veto ($75\ GeV < m_{ll} < 105\ GeV$). Since this background can not be estimated by using the fake lepton method, described in section 6.4.1, we use simulations to predict it.

In order to check how well our simulations predict the bremsstrahlung conversion mis-identification described above, we use the leptons originating in Z decays. The invariant mass of all three leptons, two originating from Z decay and one from converted bremsstrahlung, should be equal to the mass of Z boson. Thus, we count the number of three lepton events under the Z peak ($75\ GeV, 105\ GeV$) in data and in simulations. The results are summarized in table 6.14

sample	Events in data	Events in MC
$e^+e^-e^\pm$	1	0.45
$\mu^+\mu^-e^\pm$	3	0.78

Table 6.14: Number of events under the Z ($75\ GeV, 105\ GeV$) peak for tri-lepton events in simulations and in data

We combine both predictions for $e^+e^-e^\pm$ and $\mu^+\mu^-e^\pm$s to calculate the scale factor for this background, which is equal to 3.3 ± 1.6. We use this scale factor to scale our predictions from the simulations of this background.

6.5 Control Regions

The control regions are the high statistic regions in the parameter space, dominated by the background. The parameter space is defined by the variables we use to classify our events such as: The number of leptons, the amount of missing transverse energy in the event, the invariant mass of the opposite sign same flavor leptons, and the total charge of the leptons in the event. The control regions are usually obtained by relaxing one or two parameters in this space, in order to allow for more background and less signal. Thus the control regions can be used to verify the agreement between the simulation and the data. If the agreement is good

in the high statistic regions, then we have higher confidence that the simulation can predict the background in other areas of the parameter space.

In this analysis we use Monte-Carlo simulations to predict two types of "fake" background: A jet faking a prompt isolated lepton in di-leptonic $t\bar{t}$ decay and an electron from the undetected conversion of the bremsstrahlung photon in the di-lepton sample. We also use simulations to predict backgrounds from the ZZ boson pair and from the WZ boson pair, however, these backgrounds completely overlap with our signal region, thus forming control regions is difficult for this type of background. Besides, these processes have very low cross-sections (see table 6.13) thus we do not expect large uncertainties in the estimates of these backgrounds in the 35 pb^{-1} of the total integrated luminosity.

The control regions for the electron from the undetected conversion of the bremsstrahlung photon in the di-lepton sample were discussed in section 6.4.2. The amount of events in these is low as shown in table 6.14.

The natural choice of the control region for di-leptonic $t\bar{t}$ decay is the sample of the events with opposite sign muon-electron pairs, $\mu^{\pm}e^{\mp}$, because in this region $t\bar{t}$ constitutes large fraction of the Standard Model background. Thus allowing us determine whether the simulation describes it accurately.

In this sample we examine the distributions of two variables that we use to classify our channels: The invariant mass distribution of the opposite sign electron-muon pairs and the missing transverse energy distribution, see figure 6.7. We find the agreement in the control regions satisfactory thus allowing us to utilize the $t\bar{t}$ Monte-Carlo simulations for the estimation of the background in the signal regions.

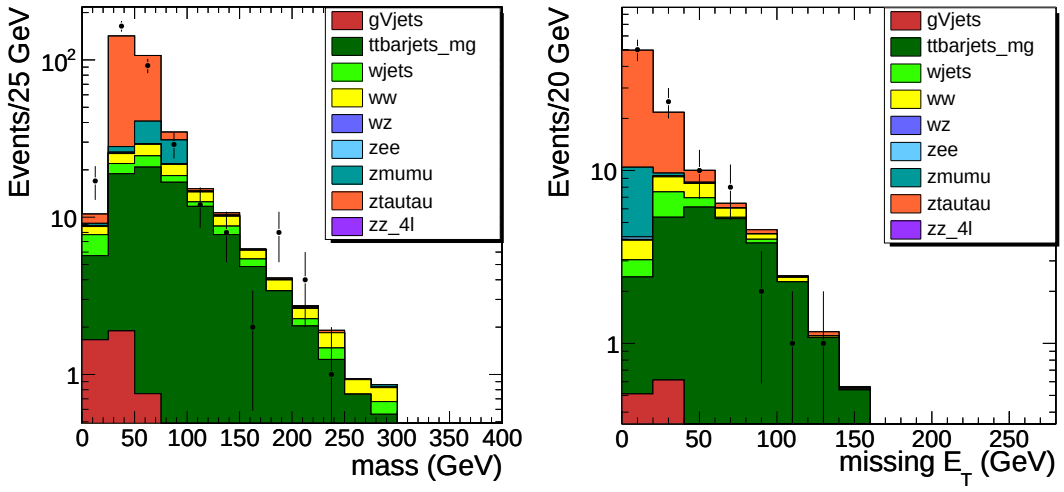

(a) (b)

Figure 6.7: Distributions for the sample of events with the opposite sign electron-muon pairs: (a) invariant mass of the highest p_T electron and of the highest p_T muon opposite sign pair (b) missing transverse energy.

Chapter 7

Results

7.1 Observed events.

Finally, all the data events that passed our selection are sorted into the exclusive channels following the procedure outlined in section 6.2.4. Then in each channel we compare with the number of Standard Model background events. However, showing all 167 channels here will be overbearing, thus to present results in more compact form we group several channels, that have similar signal to background ratios, together. This summary is shown in table 7.1.

objects # (event cut)	0T		1T		2T	
exclusive Final State	obs	exp B	obs	exp B	obs	exp B
>4	0	0 ± 0	0	0 ± 0	0	0 ± 0
4 ($\|Q\| = 4$)	0	0 ± 0	0	0 ± 0.07	0	0 ± 0.05
4 (MET+ZV)	0	0 ± 0	0	0 ± 0	0	0 ± 0
4 (MET)	0	0 ± 0	0	0 ± 0	0	0 ± 0
4 (ZV+low MET)	0	0 ± 0	0	0.01 ± 0.06	0	0.07 ± 0.02
4 (on Z + low MET)	2	0.21 ± 0.02	0	0.06 ± 0.08	0	0 ± 0.06
3 ($\|Q\| = 3$ or SSSF)	0	0.25 ± 0.1	3	0.81 ± 0.38	4	6.5 ± 1.4
3 (MET+ZV)	0	0.2 ± 0.07	0	0.36 ± 0.13	–	–
3 (MET+onZ)	3	0.94 ± 0.13	2	0.79 ± 0.19	0	0.36 ± 0.1
3 (low MET+ZV)	3	1.6 ± 0.6	32	25 ± 5	–	–
3 (low MET+onZ)	6	6.2 ± 2.1	96	99 ± 21	26	41 ± 9
Totals	14	9.4 ± 2.2	133	126 ± 21	30	48 ± 9
Totals 4L	2	0.21 ± 0.02	0	0.07 ± 0.12	0	0.07 ± 0.08
Totals 3L	12	9.2 ± 2.2	133	126 ± 21	30	48 ± 9

Table 7.1: Observed versus background events.

In this table the total number of objects in each row is the sum of selected electrons, muons, and tracks in the event. Since the background for channels

containing events with tracks is different, quite often larger, than the background for channels with only electrons and muons, we present the channels containing events with zero, one, or two tracks in the corresponding columns.

Several observation can be made here: First, the number of events observed in the channels with three objects and low missing transverse energy ($\not\!\!E_T < 50\ GeV$) is consistent with the number of predicted background events. Second, the there are no events observed in most of the channels containing events with four or more objects. The two events observed in the channel with four leptons, with low missing transverse energy, and with one of the same-flavor-opposite-sign lepton pairs has invariant mass within Z mass region ($90 \pm 15\ GeV$). Both are four muon events. One those four muon event is a very nice ZZ event, the mass of one the same-flavor-opposite-sign lepton pair is 92.24 GeV and the mass of the other the same-flavor-opposite-sign lepton pair is 92.15 GeV. In the other four muon event none of the opposite signed muon combinations make a good Z mass ($91 \pm 3\ GeV$). In the channels containing events with three leptons and high missing transverse energy we see a small excess of events in data over the background prediction in columns containing events with zero or with one track. More detail about those events one can find in appendix D.

7.2 Fitting procedure.

After sorting the observed events into the exclusive channels we perform multivariate fit over all the channels in order to see if we are sensitive to particular theoretical model or not. I will describe the theoretical models which we tested in the following sections. To perform the fit we do the following: First, we combine together channels with a similar background values, in exactly the same manner as was described in the previous section (7.1). Then, we model each channel as a

Poisson distribution with number of observed events given by k_i and number of expected events given by the λ_i, where i is the channel number.

$$f(k_i, \lambda_i) = \frac{\lambda_i^k e^{-\lambda_i}}{k_i!} \tag{7.1}$$

The number of expected events is a sum of the number of the predicted background events and the number of the expected signal events in the channel. To determine this number of the expected signal events in the particular channel, we first generate and reconstruct a Monte-Carlo sample of signal events, then following the same selection procedure as we did for the data events, we select events from this sample and classify them into the exclusive channels. Then we simply count the number of events in each channel and multiply it by the efficiencies of each object reconstructed in that channel. The resulting number is normalized to the integrated luminosity of the data sample, which in our case is 35 pb^{-1}. The number of background events is also divided in two sets: the background predicted by the data-driven method and background determined by the Monte-Carlo driven methods. The latter depends on total luminosity and the former does not. In the same manner as the signal Monte-Carlo, the background numbers determined by Monte-Carlo driven methods are multiplied by the efficiencies of each object in the channel and are scaled to the luminosity.

$$\lambda_i = S_i \times \epsilon_i \times \mathcal{L} \times \sigma_S + B_i^{MC} \times \epsilon_i \times \mathcal{L} \times \sigma_B + B_i^{DD} \tag{7.2}$$

Once we setup the models for each channel we perform simultaneous likelyhood fit over all the channels, trying to maximize the product of the Poisson distributions of all channels.

$$L = \prod_i f(k_i, \lambda_i) \tag{7.3}$$

by varying $S_{total} = \sum_i S_i$. We set other parameters, such as background errors, background efficiencies, signal efficiencies, luminosity to be nuisance parameters with a gaussian distribution, that is they will be allowed to vary but we do not care about their final value.

7.3 co-NLSP scenario.

As we discussed in the section 3.1 the multi-lepton signatures occur naturally in the co-NLSP scenarios with the compressed spectrum. As an example in table 7.2 we show the yield in various channels for the co-NLSP point with gluino mass = 900 GeV and weak mass = 600 GeV. Majority signal events we expect in the high priority channels that have events with high missing transverse energy ($\not\!\!E_T$> 50 GeV) and with invariant mass of same-flavor-opposite-sign leptons outside of Z mass veto region.

objects # (event cut)	0T			1T			2T		
exclusive Final State	obs	exp B	exp S	obs	exp B	exp S	obs	exp B	exp S
>4	0	0 ± 0	1.63	0	0 ± 0	0.63	0	0 ± 0	0.02
4 ($\|Q\| = 4$)	0	0 ± 0	0	0	0 ± 0.07	0.01	0	0 ± 0.05	0.01
4 (MET+ZV)	0	0 ± 0	2.79	0	0 ± 0	1.33	0	0 ± 0	0.62
4 (MET)	0	0 ± 0	0.9	0	0 ± 0	0.17	0	0 ± 0	0
4 (ZV+low MET)	0	0 ± 0	0.2	0	0.01 ± 0.06	0.08	0	0.07 ± 0.02	0.04
4 (on Z + low MET)	2	0.21 ± 0.02	0.04	0	0.06 ± 0.08	0	0	0 ± 0.06	0
3 ($\|Q\| = 3$ or SSSF)	0	0.25 ± 0.1	0.21	3	0.81 ± 0.38	0.26	4	6.5 ± 1.4	0.01
3 (MET+ZV)	0	0.2 ± 0.07	2.39	0	0.36 ± 0.13	1.04	–	–	–
3 (MET+onZ)	3	0.94 ± 0.13	0.43	2	0.79 ± 0.19	0.5	0	0.36 ± 0.1	0.34
3 (low MET+ZV)	3	1.6 ± 0.6	0.17	32	25 ± 5	0.05	–	–	–
3 (low MET+onZ)	6	6.2 ± 2.1	0.01	96	99 ± 21	0.02	26	41 ± 9	0.02
Totals	14	9.4 ± 2.2	8.77	133	126 ± 21	4.09	30	48 ± 9	1.06
Totals 4L	2	0.21 ± 0.02	5.56	0	0.07 ± 0.12	2.22	0	0.07 ± 0.08	0.69
Totals 3L	12	9.21 ± 2.18	3.21	133	126 ± 21	1.87	30	48 ± 9	0.37

Table 7.2: Expected signal for co-NLSP point with gluino mass = 900 GeV and weak mass = 600 GeV.

To expand our search beyond just one sample we generate a number of samples in co-NLSP parameter space by varying gluino mass in the range from 800 GeV to 1600 GeV and varying weak mass in the range from 300 GeV to 900 GeV, than

applying the statistical procedure described above in section 7.2 on each point in this parameter space we find the 95% exclusion limits in this parameter space as shown in figure 7.1. From this figure we see that the region with the gluino mass below 1000 GeV is ruled out for all values of the chargino mass. Also we see that the observed limit is within one sigma confidence band from the expected limit for most of the values of the chargino mass.

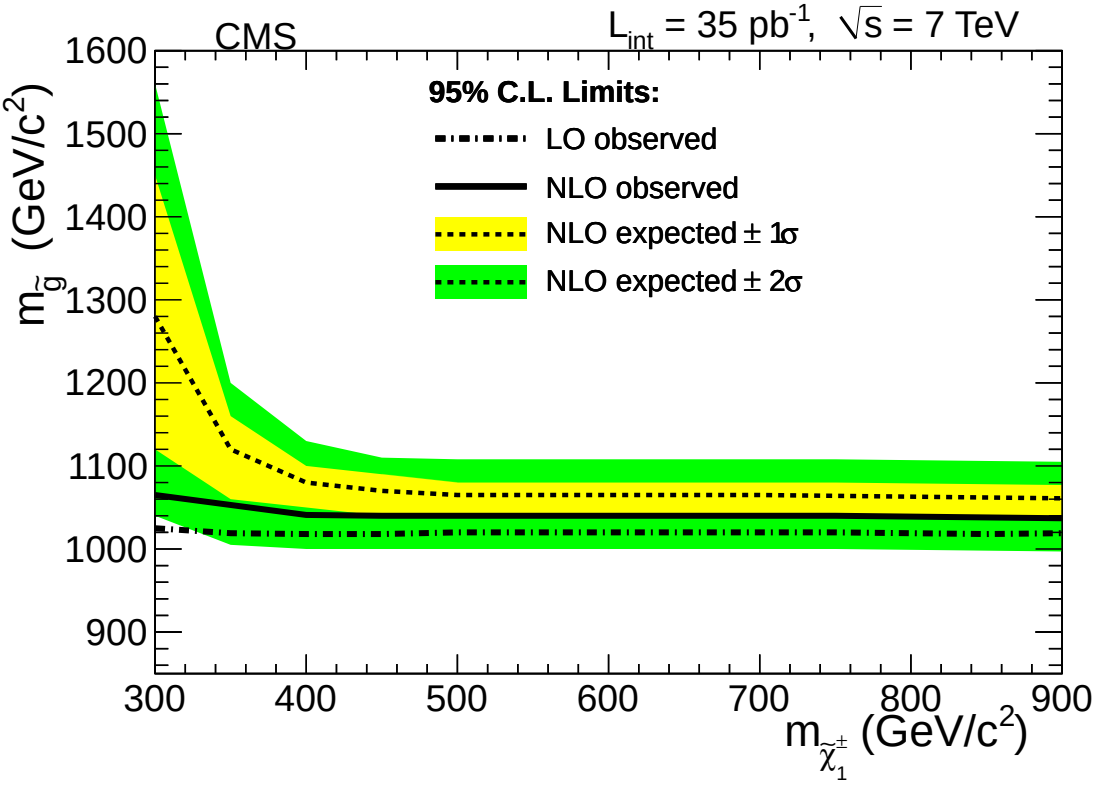

Figure 7.1: co-NLSP exclusion limits in the gluino and chargino (weak mass) parameter space.

7.4 RPV scenario.

When R-parity is violated

SUSY with R-parity violation scenario was discussed in section 3.2. We recall that if the leptonic R-parity violating coupling is non-zero ($\lambda_{ijk} \neq 0$) then neutralino decays into two charge leptons and neutrino. Thus we obtain four

charge leptons in each event from the two decaying neutralinos. Here we consider separately the case when $\lambda_{122} \neq 0$ and the case when $\lambda_{123} \neq 0$. As the indices of λ_{ijk} couplings denote the lepton generation, we obtain signature with muons and electrons in the final state for the former case and signature with muons, electrons, and taus in the final state for the latter case.

objects # (event cut)	0T			1T			2T		
exclusive Final State	obs	exp B	exp S	obs	exp B	exp S	obs	exp B	exp S
>4	0	0 ± 0	0.05	0	0 ± 0	0.07	0	0 ± 0	0
4 ($\|Q\| = 4$)	0	0 ± 0	0	0	0 ± 0.07	0	0	0 ± 0.05	0
4 (MET+ZV)	0	0 ± 0	8.46	0	0 ± 0	1.37	0	0 ± 0	0.12
4 (MET)	0	0 ± 0	2.45	0	0 ± 0	0.15	0	0 ± 0	0
4 (ZV+low MET)	0	0 ± 0	1.06	0	0.01 ± 0.06	0.14	0	0.07 ± 0.02	0.01
4 (on Z + low MET)	2	0.21 ± 0.02	0.17	0	0.06 ± 0.08	0.03	0	0 ± 0.06	0
3 ($\|Q\| = 3$ or SSSF)	0	0.3 ± 0.1	2.18	3	0.82 ± 0.38	0.3	4	6.5 ± 1.4	0
3 (MET+ZV)	0	0.2 ± 0.07	5.81	0	0.35 ± 0.13	0.38	–	–	–
3 (MET+onZ)	3	0.95 ± 0.13	1.15	2	0.79 ± 0.19	0.32	0	0.36 ± 0.1	0.02
3 (low MET+ZV)	3	1.6 ± 0.6	0.59	32	25.4 ± 5.1	0.02	–	–	–
3 (low MET+onZ)	6	6.2 ± 2.1	0.04	96	99 ± 21	0	26	41 ± 9	0
Totals	14	9.5 ± 2.2	22	133	126 ± 21	2.78	30	48 ± 9	0.15
Totals 4L	2	0.21 ± 0.02	12.19	0	0.07 ± 0.12	1.76	0	0.07 ± 0.08	0.13
Totals 3L	12	9.3 ± 2.2	9.77	133	126 ± 21	1.02	30	48 ± 9	0.02

Table 7.3: Expected signal for rpv $\lambda_{122} \neq 0$ point with gluino mass = 700 GeV and squark mass = 700 GeV, bino mass = 300 GeV, and with all other super-partners de-coupled.

The table 7.3 shows the signal we would have obtained in our exclusive channels when $\lambda_{122} \neq 0$ and gluino mass = 700 GeV and squark mass = 700 GeV, bino mass = 300 GeV, and all other super-partners de-coupled. We notice that majority of the signal is expected channels with little or zero background. Also, since we do not expect any taus in our signal most of the signal events ends in the channels containing events with zero isolated tracks in the final state.

The table 7.4 shows the signal we would have obtained in our exclusive channels when $\lambda_{123} \neq 0$ and gluino mass = 700 GeV and squark mass = 700 GeV, bino mass = 300 GeV, and all other super-partners de-coupled. Again, we notice that majority of the signal is expected channels with little or zero background. This time though we do expect more signal in the channels containing events with one or two isolated tracks in the final state.

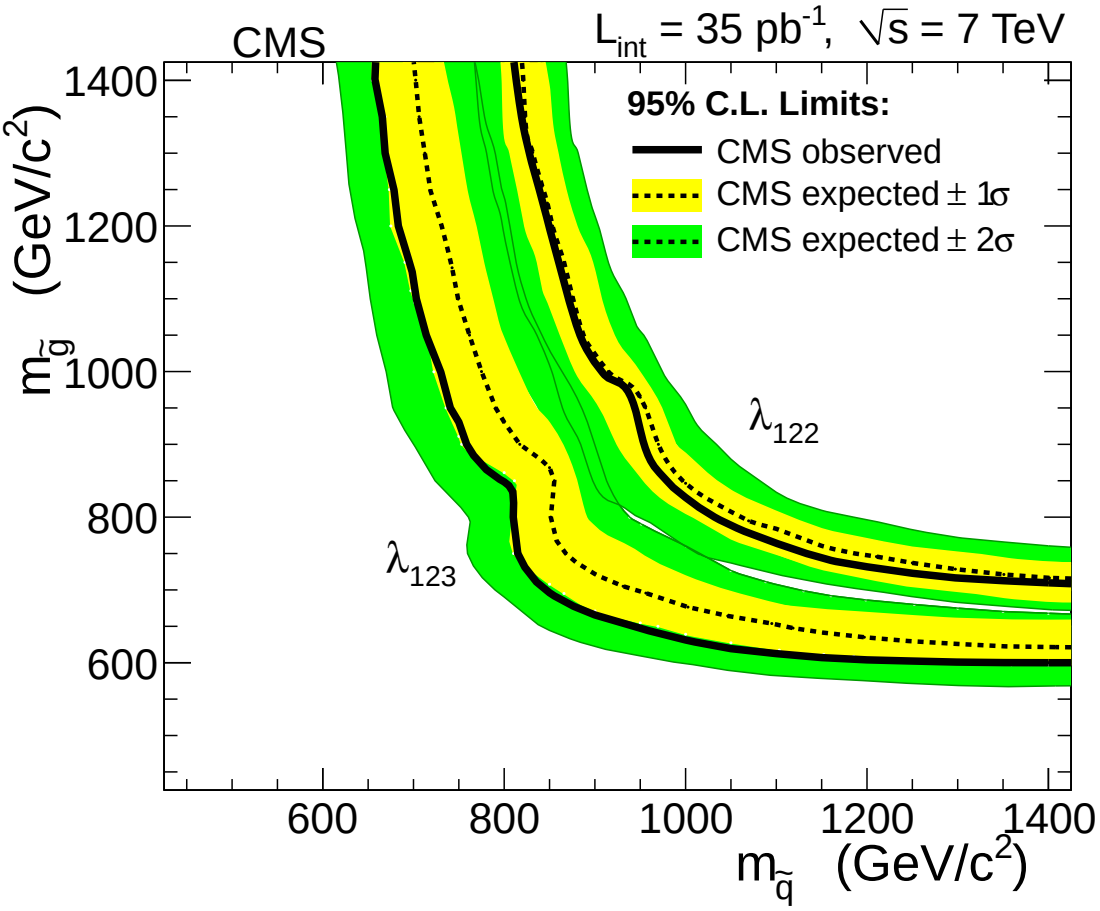

Figure 7.2: RPV exclusion limits for $\lambda_{122} \neq 0$ and for $\lambda_{123} \neq 0$. In gluino versus squark parameter space for fix bino mass 300 GeV with all other super-partners decoupled.

objects # (event cut)	0T			1T			2T		
exclusive Final State	obs	exp B	exp S	obs	exp B	exp S	obs	exp B	exp S
>4	0	0 ± 0	0	0	0 ± 0	0.2	0	0 ± 0	0
4 ($\|Q\| = 4$)	0	0 ± 0	0	0	0 ± 0.07	0	0	0 ± 0.05	0
4 (MET+ZV)	0	0 ± 0	0.55	0	0 ± 0	1.57	0	0 ± 0	1.33
4 (MET)	0	0 ± 0	0.35	0	0 ± 0	0.32	0	0 ± 0	0
4 (ZV+low MET)	0	0 ± 0	0.07	0	0.01 ± 0.06	0.11	0	0.07 ± 0.02	0.09
4 (on Z + low MET)	2	0.21 ± 0.02	0.02	0	0.06 ± 0.08	0.01	0	0 ± 0.06	0
3 ($\|Q\| = 3$ or SSSF)	0	0.25 ± 0.1	1.44	3	0.81 ± 0.38	2	4	6.5 ± 1.4	0.01
3 (MET+ZV)	0	0.2 ± 0.07	3.38	0	0.36 ± 0.13	1.57	–	–	–
3 (MET+onZ)	3	0.94 ± 0.13	0.94	2	0.79 ± 0.19	3.7	0	0.36 ± 0.1	1.39
3 (low MET+ZV)	3	1.62 ± 0.59	0.26	32	25.42 ± 5.13	0.11	–	–	–
3 (low MET+onZ)	6	6.2 ± 2.09	0.05	96	99 ± 21	0.36	26	41 ± 9	0.12
Totals	14	9.4 ± 2.2	7.06	133	126 ± 21	9.95	30	48 ± 9	2.94
Totals 4L	2	0.21 ± 0.02	0.99	0	0.07 ± 0.12	2.21	0	0.07 ± 0.08	1.42
Totals 3L	12	9.2 ± 2.2	6.07	133	126 ± 21	7.74	30	48 ± 9	1.52

Table 7.4: Expected signal for rpv $\lambda_{123} \neq 0$ point with gluino mass = 700 GeV and squark mass = 700 GeV, bino mass = 300 GeV, and with all other super-partners de-coupled..

To expand our search beyond just one sample we generate a number of samples in MSSM parameter space by varying gluino mass in the range from 400 GeV to 1450 GeV and varying squark mass in the range from 400 GeV to 1450 GeV for both $\lambda_{122} \neq 0$ and $\lambda_{123} \neq 0$ separately, than applying the statistical procedure described above in section 7.2 on each point in this parameter space we find the 95% exclusion limits in this parameter space as shown in figure 7.2. From this figure we see that the region with the gluino mass below 600 GeV is ruled out for all values of the squark mass. Also we see that the observed limit is within one sigma confidence band from the expected limit for the whole region. The bump in the exclusion curves is due to sudden change of efficiency in lepton isolation due appearing of two extra jets in the final state when the squark mass becomes larger than the gluino mass, as shown of figure 7.4.

Our limits for $\lambda_{122} \neq 0$ are better than our limits for $\lambda_{123} \neq 0$ because we have better sensitivity to electrons and muons than to taus.

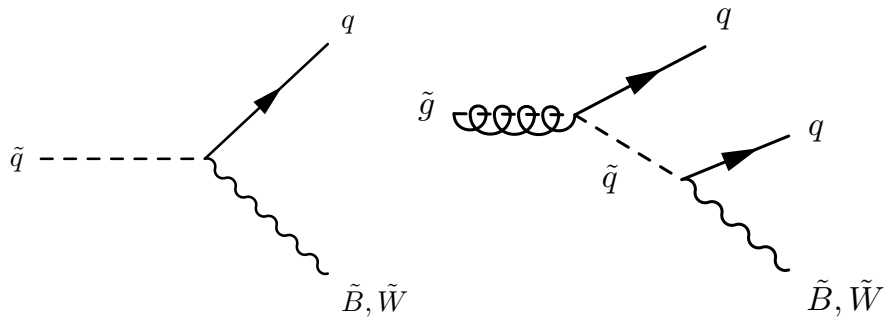

(a) (b)

Figure 7.3: Average jet multiplicity for constant squark mass = 950 GeV as the function of the gluino mass. Two extra jet appear in the final state when the squark mass becomes larger than the gluino mass.

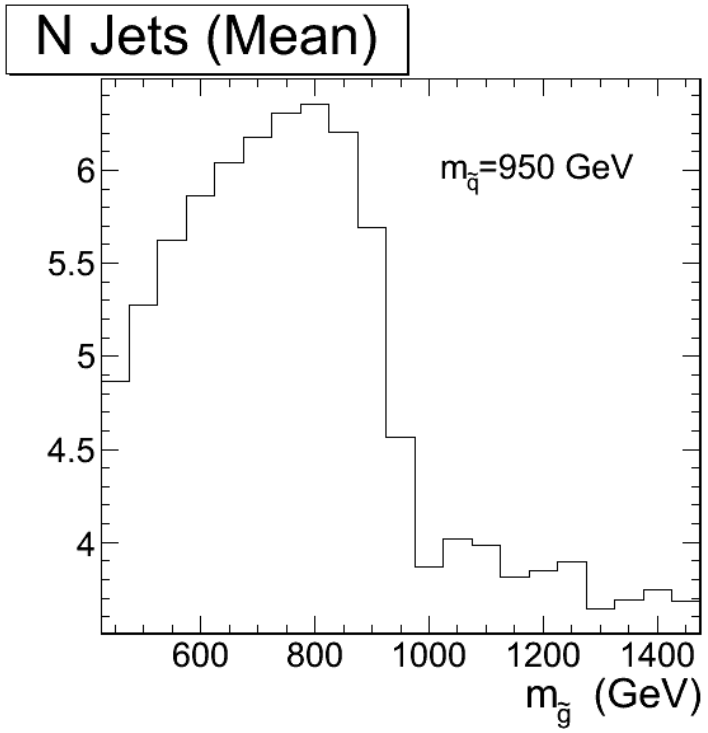

Figure 7.4: Average jet multiplicity for constant squark mass = 950 GeV as the function of the gluino mass. Two extra jet appear in the final state when the squark mass becomes larger than the gluino mass.

7.5 cMSSM scenario.

As we discussed in the section 3.3 in constrained MSSM scenario where the SUSY breaking is mediated by gravity is associated with tri-lepton signature when the chargino-neutralino electro-weakly produced. Here as example we use cMSSM point with $m_0 = 70\ GeV$, $m_{1/2} = 200\ GeV$, and $tan(\beta) = 3$.

objects # (event cut)	0T			1T			2T		
exclusive Final State	obs	exp B	exp S	obs	exp B	exp S	obs	exp B	exp S
>4	0	0 ± 0	0	0	0 ± 0	0	0	0 ± 0	0
4 ($\|Q\| = 4$)	0	0 ± 0	0	0	0 ± 0.07	0	0	0 ± 0.05	0
4 (MET+ZV)	0	0 ± 0	0.88	0	0 ± 0	0.69	0	0 ± 0	0.29
4 (MET)	0	0 ± 0	0.27	0	0 ± 0	0.06	0	0 ± 0	0
4 (ZV+low MET)	0	0 ± 0	0.22	0	0.01 ± 0.06	0.28	0	0.07 ± 0.02	0
4 (on Z + low MET)	2	0.21 ± 0.02	0.06	0	0.06 ± 0.08	0	0	0 ± 0.06	0
3 ($\|Q\| = 3$ or SSSF)	0	0.25 ± 0.1	0	3	0.81 ± 0.38	0.16	4	6.5 ± 1.4	0.09
3 (MET+ZV)	0	0.2 ± 0.07	5.02	0	0.36 ± 0.13	3.44	–	–	–
3 (MET+onZ)	3	0.94 ± 0.13	0.62	2	0.79 ± 0.19	0.55	0	0.36 ± 0.1	0.9
3 (low MET+ZV)	3	1.62 ± 0.59	1.58	32	25.4 ± 5.1	1.47	–	–	–
3 (low MET+onZ)	6	6.2 ± 2.1	0	96	99 ± 21	0.06	26	41 ± 9	0.29
Totals	14	9.4 ± 2.2	8.65	133	126 ± 21	6.71	30	48 ± 9	1.57
Totals 4L	2	0.21 ± 0.02	1.43	0	0.07 ± 0.12	1.03	0	0.07 ± 0.08	0.29
Totals 3L	12	9.2 ± 2.2	7.22	133	126 ± 21	5.68	30	48 ± 9	1.28

Table 7.5: Expected signal for cMSSM $m_0 = 70\ GeV$ and $m_{1/2} = 200\ GeV$.

We see in the table 7.5 that the primary signal are the events with three leptons, one of them could be track, with high missing transverse energy and with the invariant mass of the same-flavor-opposite-sign leptons outside of the Z veto region.

To expand our search beyond just one sample we generate a number of samples in MSSM parameter space by varying $m_{1/2}$ in the range from 150 GeV to 400 GeV and varying m_0 in the range from 0 GeV to 300 GeV. than applying the statistical procedure described above in section 7.2 on each point in this parameter space we find the 95% exclusion limits in this parameter space as shown in figure 7.5. We see that our limits extend above the limit previously excluded by the tevatron experiments. The gap in the exclusion plot is due to the fact that lepton spectrum

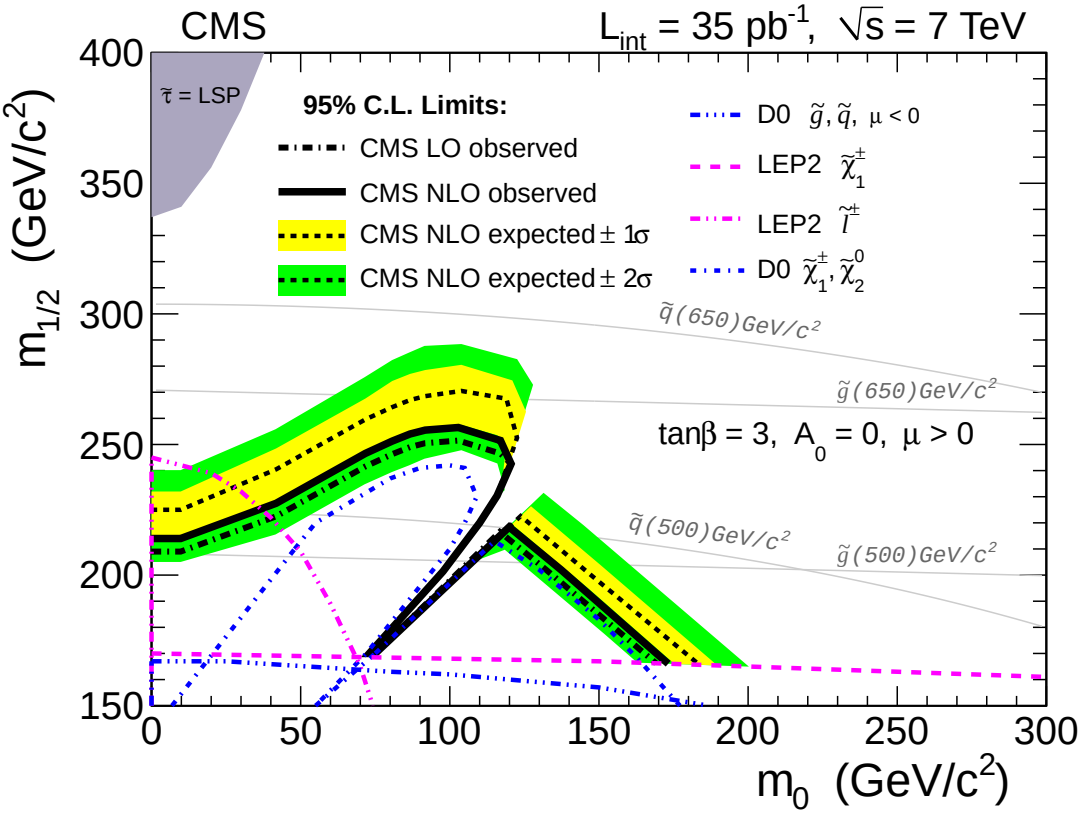

Figure 7.5: constrained MSSM exclusion limits in $m_{1/2}$ versus squarkm_0 parameter space for fix $tan(\beta) = 3$.

becomes much softer in this part of the parameter space, thus we are limited by the detector acceptance.

References

[1] D. Kovalskyi, et al. Fireworks: A physics event display for cms. *Journal of Physics*, 219, 2010.

[2] S. Baffioni, et al. Electron identification in cms. Technical Report AN2009/178, CMS Collaboration, 2009.

[3] D. Barge, et al. Study of photon conversion rejection at cms. *CMS Analysis Note*, (159), 2009.

[4] C. Collaboration. Performance of cms muon reconstruction in cosmic-ray events. *Journal of Instrumentation*, 5(03):T03022, 2010.

[5] M. Cacciari and G. P. Salam. The anti-k_t jet clustering algorithm. *Journal of High Energy Physics*, 2008(04):063, 2008. ArXiv:0802.1189.

[6] C. Collaboration. Commissioning of the particle-flow event reconstruction with the first lhc collisions recorded in the cms detector. *CMS PAS*, PFT-10-01, 2010.

[7] M. Peskin and D. Schroeder. *An introduction to Quantum Field Theory*. Westview press, 1995.

[8] H. Georgi and S. L. Glashow. Unity of all elementary-particle forces. *Phys. Rev. Lett.*, 32(8):438–441, Feb 1974.

[9] K. A. Olive. Dark Matter in SuperGUT Unification Models. 2010.

[10] K. Inoue, et al. Low energy parameters and particle masses in a supersymmetric grand unified model. *Progress of Theoretical Physics*, 67:1889–98, 1982.

[11] K. Inoue, A. Kakuto, and S. Takeshita. Weak-symmetry breaking in locally supersymmetric grand unified theories. *Progress of Theoretical Physics*, 71:348–63, 1984.

[12] D. I. Kazakov. Beyond the standard model (in search of supersymmetry). 2001.

[13] G. Papotti. Luminosity analysis. pp. 244–247, 2011.

[14] C. Collaboration. The cms experiment at the cern lhc. *Journal of Instrumentation*, 3, 2008.

[15] C. Collaboration. Tracking and primary vertex results in first 7 tev collisions. *CMS Physics Analysis Summary*, 2010.

[16] R. Fŕuhwirth, W. Waltenberger, and P. Vanlaer. Adaptive vertex fitting. Technical Report CMS-NOTE-2007-008. CERN-CMS-NOTE-2007-008, CERN, Geneva, Mar 2007.

[17] M. Pioppi. Iterative tracking. *CMS Internal Note*, (2007/065), 2008.

[18] T. Speer, et al. Track reconstruction in the cms tracker. *Nuclear Instruments and Methods in Physics Research Section A: Accelerators, Spectrometers, Detectors and Associated Equipment*, 559(1):143 – 147, 2006. Proceedings of the X International Workshop on Advanced Computing and Analysis Techniques in Physics Research - ACAT 05.

[19] R. E. Kalman. A new approach to linear filtering and prediction problems. *Trans. ASME, D*, 82:35–44, 1960.

[20] P. Azzurri and B. Mangano. Optimal filtering of fake tracks. *CMS Internal Note*, (2008/017), 2008.

[21] H. Bethe and W. Heitler. On the stopping of fast particles and on the creation of positive electrons. *Proceedings of the Royal Society of London A*, 146:83–112, 1934.

[22] N. Rompotis and C. Seez. URL `https://twiki.cern.ch/twiki/bin/view/CMS/SimpleCutBasedEleID`.

[23] A. P. Vartak, M. LeBourgeois, and V. Sharma. Lepton isolation in the cms tracker, ecal and hcal. Technical Report AN2010/106, CMS Collaboration, 2010.

[24] C. Collaboration. Study of tau reconstruction algorithms using pp collisions data collected at $\sqrt{s} = 7$ tev. *CMS PAS*, PFT-10-04, 2010.

[25] C. Collaboration. Performance of tau reconstruction algorithms in 2010 data collected with cms. *CMS PAS*, TAU-11-001, 2011.

Appendix A

Datasets

/MinimumBias/Commissioning10-PromptReco-vx/RECO

Appendix B

Triggers

2010 was the first year of the collecting collision data at 7 TeV and the luminosity increased exponentially during this period. As the result the trigger table evolved a significantly with the understanding of the detector behavior and beam backgrounds and to cope with increasing luminosity. For this analysis we choose events which came either on single muon triggers or on single electron triggers. The single muon triggers are:

- Muon Triggers with p_T threshold 9 GeV:
  - HLT_Mu9, HLT_IsoMu9, HLT_IsoMu9_v3, HLT_IsoMu9_v4.
- Muon Triggers with p_T threshold 11 GeV:
  - HLT_Mu11, HLT_IsoMu11_v1, HLT_IsoMu11_v3, HLT_IsoMu11_v4.
- Muon Triggers with p_T threshold 13 GeV:
  - HLT_IsoMu13_v1, HLT_IsoMu13_v3, HLT_IsoMu13_v4,
- Muon Triggers with p_T threshold 15 GeV:
  - HLT_IsoMu15_v3, HLT_IsoMu15_v4.

The single electron triggers are:

- Electron Triggers with p_T threshold 10 GeV:

- HLT_Ele10_SW_L1R, HLT_Ele10_SW_L1R_v2, HLT_Ele10_LW_EleId_L1R, HLT_Ele10_SW_EleId_L1R.

- Electron Triggers with p_T threshold 12 GeV:
  - HLT_Ele12_SW_TighterEleId_L1R, HLT_Ele12_SW_TightEleIdIsol_L1R, HLT_Ele12_SW_TighterEleIdIsol_L1R, HLT_Ele12_SW_TightEleIdIsol_NoDEtaInEE_L1R,

- Electron Triggers with p_T threshold 15 GeV:
  - HLT_Ele15_SW_L1R, HLT_Ele15_SC10_LW_L1R, HLT_Ele15_SW_EleId_L1R, HLT_Ele15_SW_CaloEleId_L1R,

- Electron Triggers with p_T threshold 17 GeV:
  - Without electron ID:

    HLT_Ele17_SW_L1R, HLT_Ele17_SW_L1R_v2,
  - With electron ID:

    HLT_Ele17_SW_EleId_L1R, HLT_Ele17_SW_CaloEleId_L1R, HLT_Ele17_SW_LooseEleId_L1R, HLT_Ele17_SW_TightEleId_L1R, HLT_Ele17_SW_TighterEleId_L1R_v1, HLT_Ele17_SW_TightCaloEleId_SC8HE_L1R_v1, HLT_Ele17_SW_TightCaloEleId_Ele8HE_L1R_v1, HLT_Ele17_SW_TightCaloEleId_Ele8HE_L1R_v2,
  - With electron ID and isolation:

    HLT_Ele17_SW_TightEleIdIsol_L1R, HLT_Ele17_SW_TightEleIdIsol_L1R_v1, HLT_Ele17_SW_TighterEleIdIsol_L1R_v1, HLT_Ele17_SW_TighterEleIdIsol_L1R_v2, HLT_Ele17_SW_TighterEleIdIsol_L1R_v3,
  - With isolation:

    HLT_Ele17_SW_Isol_L1R_v1, HLT_Ele17_SW_Isol_L1R_v2,

  - Electron Triggers with p_T threshold 20 GeV:

    HLT_Ele20_SW_L1R, HLT_Ele20_LW_L1R.

- Electron Triggers with p_T threshold 22 GeV:

  - Without electron ID:

    HLT_Ele22_SW_L1R, HLT_Ele22_SW_L1R_v2,

  - With electron ID:

    HLT_Ele22_SW_CaloEleId_L1R, HLT_Ele22_SW_TighterEleId_L1R,
    HLT_Ele22_SW_TighterEleId_L1R_v2,

  - With electron ID and Isolation:

    HLT_Ele22_SW_TighterCaloIdIso1_L1R,
    HLT_Ele22_SW_TighterCaloIdIso1_L1R_v2,

Appendix C

Channels.

Here is the list of exclusive channels in the order of their priority.

The following abbreviations are used to describe the channels.

$\underline{\boldsymbol{N_{e,\mu}^{\mathrm{iso}} > 4}}$

ElandMuGt4Qhigh, ElandMuGt4Qlow, T1ElandMu4Qhigh, T1ElandMu4Qlow, T2ElandMu3Qhigh, T2ElandMu3Qlow

$\underline{\boldsymbol{\not{E}_T > 50\ GeV,\ m_{ll} < 75\ GeV,\ m_{ll} > 105\ GeV}}$

$\underline{\boldsymbol{N_{\mu}^{\mathrm{iso}} = 4}}$
Mu4q4METVZV , Mu4q2METVZV , Mu4q0METVZV

$\underline{\boldsymbol{N_{\mu}^{\mathrm{iso}} = 3,\ N_{e}^{\mathrm{iso}} = 1}}$
Mu3El1Q4METVZV, Mu3El1Q2METVZV, Mu3El1Q0METVZV

$\underline{\boldsymbol{N_{\mu}^{\mathrm{iso}} = 3,\ N_{track}^{\mathrm{iso}} = 1}}$
Mu3T1Q4METVZV, Mu3T1Q2METVZV, Mu3T1Q0METVZV

$\underline{\boldsymbol{N_{\mu}^{\mathrm{iso}} = 2,\ N_{e}^{\mathrm{iso}} = 2}}$
Mu2El2Q4METVZV , Mu2El2Q2METVZV , Mu2El2Q0METVZV

$\underline{\boldsymbol{N_{\mu}^{\mathrm{iso}} = 2,\ N_{e}^{\mathrm{iso}} = 1,\ N_{track}^{\mathrm{iso}} = 1}}$
Mu2El1T1Q4METVZV , Mu2El1T1Q2METVZV , Mu2El1T1Q0METVZV

$\underline{\boldsymbol{N_{\mu}^{\mathrm{iso}} = 1,\ N_{e}^{\mathrm{iso}} = 3}}$
Mu1El3Q4METVZV , Mu1El3Q2METVZV , Mu1El3Q0METVZV

$\underline{\boldsymbol{N_{\mu}^{\mathrm{iso}} = 1,\ N_{e}^{\mathrm{iso}} = 1,\ N_{track}^{\mathrm{iso}} = 1}}$
, Mu1El2T1Q4METVZV , Mu1El2T1Q2METVZV , Mu1El2T1Q0METVZV

$\underline{\boldsymbol{N_e^{\text{iso}} = 4}}$

El4q4METVZV , El4q2METVZV , El4q0METVZV

$\underline{\boldsymbol{N_e^{\text{iso}} = 3, N_{track}^{\text{iso}} = 1}}$

El3T1Q4METVZV , El3T1Q2METVZV , El3T1Q0METVZV

$\underline{\boldsymbol{N_{\mu,e}^{\text{iso}} = 2, N_{track}^{\text{iso}} = 2}}$

T2Any2LepQ4METVZV , T2Any2LepQ2METVZV , T2Any2LepQ0METVZV

$\underline{\boldsymbol{\not{E}_T > 50\ GeV, 75\ GeV < m_{ll} < 105\ GeV}}$

$\underline{\boldsymbol{N_\mu^{\text{iso}} = 4}}$

Mu4q4METV , Mu4q2METV , Mu4q0METV

$\underline{\boldsymbol{N_\mu^{\text{iso}} = 3, N_e^{\text{iso}} = 1}}$

Mu3El1Q4METV , Mu3El1Q2METV , Mu3El1Q0METV

$\underline{\boldsymbol{N_\mu^{\text{iso}} = 3, N_{track}^{\text{iso}} = 1}}$

Mu3T1Q4METV , Mu3T1Q2METV , Mu3T1Q0METV

$\underline{\boldsymbol{N_\mu^{\text{iso}} = 2, N_e^{\text{iso}} = 2}}$

Mu2El2Q4METV , Mu2El2Q2METV , Mu2El2Q0METV

$\underline{\boldsymbol{N_\mu^{\text{iso}} = 2, N_e^{\text{iso}} = 1, N_{track}^{\text{iso}} = 1}}$

Mu2El1T1Q4METV , Mu2El1T1Q2METV , Mu2El1T1Q0METV

$\underline{\boldsymbol{N_\mu^{\text{iso}} = 1, N_e^{\text{iso}} = 3}}$

Mu1El3Q4METV , Mu1El3Q2METV , Mu1El3Q0METV

$\underline{\boldsymbol{N_\mu^{\text{iso}} = 1, N_e^{\text{iso}} = 2, N_{track}^{\text{iso}} = 1}}$

Mu1El2T1Q4METV , Mu1El2T1Q2METV , Mu1El2T1Q0METV

$\underline{\boldsymbol{N_e^{\text{iso}} = 4}}$

El4q4METV , El4q2METV , El4q0METV

$\underline{\boldsymbol{N_e^{\text{iso}} = 3, N_{track}^{\text{iso}} = 1}}$

El3T1Q4METV , El3T1Q2METV , El3T1Q0METV

$\underline{\boldsymbol{N_{e,\mu}^{\text{iso}} = 23, N_{track}^{\text{iso}} = 2}}$

T2Any2LepQ4METV , T2Any2LepQ2METV , T2Any2LepQ0METV

$\underline{\boldsymbol{\not{E}_T < 50\ GeV, m_{ll} < 75\ GeV, m_{ll} > 105\ GeV}}$

$\underline{\boldsymbol{N_{\mu}^{\mathrm{iso}} = 4}}$

Mu4q4ZV , Mu4q2ZV , Mu4q0ZV

$\underline{\boldsymbol{N_{\mu}^{\mathrm{iso}} = 3, N_{e}^{\mathrm{iso}} = 1}}$

Mu3El1Q4ZV , Mu3El1Q2ZV , Mu3El1Q0ZV

$\underline{\boldsymbol{N_{\mu}^{\mathrm{iso}} = 3, N_{track}^{\mathrm{iso}} = 1}}$

Mu3T1Q4ZV , Mu3T1Q2ZV , Mu3T1Q0ZV

$\underline{\boldsymbol{N_{\mu}^{\mathrm{iso}} = 2, N_{e}^{\mathrm{iso}} = 2}}$

Mu2El2Q4ZV , Mu2El2Q2ZV , Mu2El2Q0ZV

$\underline{\boldsymbol{N_{\mu}^{\mathrm{iso}} = 2, N_{e}^{\mathrm{iso}} = 1, N_{track}^{\mathrm{iso}} = 1}}$

Mu2El1T1Q4ZV , Mu2El1T1Q2ZV , Mu2El1T1Q0ZV

$\underline{\boldsymbol{N_{\mu}^{\mathrm{iso}} = 1, N_{e}^{\mathrm{iso}} = 3}}$

Mu1El3Q4ZV , Mu1El3Q2ZV , Mu1El3Q0ZV

$\underline{\boldsymbol{N_{\mu}^{\mathrm{iso}} = 1, N_{e}^{\mathrm{iso}} = 2, N_{track}^{\mathrm{iso}} = 1}}$

Mu1El2T1Q4ZV , Mu1El2T1Q2ZV , Mu1El2T1Q0ZV

$\underline{\boldsymbol{N_{e}^{\mathrm{iso}} = 4}}$

El4q4ZV , El4q2ZV , El4q0ZV

$\underline{\boldsymbol{N_{e}^{\mathrm{iso}} = 3, N_{track}^{\mathrm{iso}} = 1}}$

El3T1Q4ZV , El3T1Q2ZV , El3T1Q0ZV

$\underline{\boldsymbol{N_{e,\mu}^{\mathrm{iso}} = 2, N_{track}^{\mathrm{iso}} = 2}}$

T2Any2LepQ4ZV , T2Any2LepQ2ZV , T2Any2LepQ0ZV

$\underline{\boldsymbol{\not{E}_T < 50\ GeV, 75\ GeV < m_{ll} < 105\ GeV}}$

$\underline{\boldsymbol{N_{\mu}^{\mathrm{iso}} = 4}}$

Mu4q4 , Mu4q2 , Mu4q0

$\underline{\boldsymbol{N_{\mu}^{\mathrm{iso}} = 3, N_{e}^{\mathrm{iso}} = 1}}$

Mu3El1Q4 , Mu3El1Q2 , Mu3El1Q0

$\underline{\boldsymbol{N_{\mu}^{\mathrm{iso}} = 3, N_{track}^{\mathrm{iso}} = 1}}$

Mu3T1Q4 , Mu3T1Q2 , Mu3T1Q0

$\underline{\boldsymbol{N_{\mu}^{\text{iso}} = 2, N_{e}^{\text{iso}} = 2}}$

Mu2El2Q4 , Mu2El2Q2 , Mu2El2Q0

$\underline{\boldsymbol{N_{\mu}^{\text{iso}} = 2, N_{e}^{\text{iso}} = 1, N_{track}^{\text{iso}} = 1}}$

Mu2El1T1Q4 , Mu2El1T1Q2 , Mu2El1T1Q0

$\underline{\boldsymbol{N_{\mu}^{\text{iso}} = 1, N_{e}^{\text{iso}} = 3}}$

Mu1El3Q4 , Mu1El3Q2 , Mu1El3Q0

$\underline{\boldsymbol{N_{\mu}^{\text{iso}} = 1, N_{e}^{\text{iso}} = 2, N_{track}^{\text{iso}} = 1}}$

Mu1El2T1Q4 , Mu1El2T1Q2 , Mu1El2T1Q0

$\underline{\boldsymbol{N_{e}^{\text{iso}} = 4}}$

El4q4 , El4q2 , El4q0

$\underline{\boldsymbol{N_{e}^{\text{iso}} = 3, N_{track}^{\text{iso}} = 1}}$

El3T1Q4 , El3T1Q2 , El3T1Q0

$\underline{\boldsymbol{N_{e,\mu}^{\text{iso}} = 2, N_{track}^{\text{iso}} = 2}}$

T2Any2LepQ4 , T2Any2LepQ2 , T2Any2LepQ0

3 Lepton, $\boldsymbol{\not{E}_T > 50\ GeV}$

$\underline{\boldsymbol{N_{\mu}^{\text{iso}} = 3}}$

Mu3q1METVZV , Mu3q1METV

$\underline{\boldsymbol{N_{\mu}^{\text{iso}} = 2, N_{e}^{\text{iso}} = 1}}$

Mu2q0El1METVZV, Mu2q0El1METV

$\underline{\boldsymbol{N_{\mu}^{\text{iso}} = 1, N_{e}^{\text{iso}} = 2}}$

El2q0Mu1METVZV , El2q0Mu1METV

$\underline{\boldsymbol{N_{e}^{\text{iso}} = 3}}$

El3q1METVZV , El3q1METV

3 Lepton, $\boldsymbol{\not{E}_T < 50\ GeV}$

$\underline{\boldsymbol{N_{e,\mu}^{\text{iso}} = 3}}$

Mu3q3 , Mu2q2El1 , Mu3q1ZV , Mu3q1 , El2q2Mu1 , El3q3

2 muons + 1 Track, $\not\!\!E_T > 50$ *GeV*

Mu2q2T1METV , Mu2q0T1METVZV , Mu2q0T1METV

2 electrons + 1 Track, $\not\!\!E_T > 50$ *GeV*

El2q2T1METV , El2q0T1METVZV , El2q0T1METV

1 muon, 1 electron, 1 Track, $\not\!\!E_T > 50$ *GeV*

Mu1El1T1Q3 , Mu1El1T1Q1METV

1 lepton + 2 Track, $\not\!\!E_T > 50$ *GeV* or high total charge

Mu1T2Q3 , Mu1T2Q1METV , El1T2Q3 , El1T2Q1METV

2lepton + 1Track, Zveto

Mu2q0T1ZV , El2q0T1ZV , Mu2q0El1ZV

2samesignleptons + 1Track

Mu2q2T1 , El2q2T1

3leptonswithlowtotalcharge , El2q0Mu1ZV , El2q0Mu1 , El3q1ZV , Mu2q0El1 , Mu2q0T1 , Mu1El1T1Q1 , El2q0T1 , Mu1T2Q1 , El1T2Q1 , El3q1

Appendix D

Interesting events

Here we have interesting events!